Gerd Korbinian Meisl

**Nitrogen implantation in tungsten and migration in the fusion experiment ASDEX Upgrade**

# Technische Universität München

## Max-Planck-Institut für Plasmaphysik

## Nitrogen implantation in tungsten and migration in the fusion experiment ASDEX Upgrade

Gerd Korbinian Meisl

Vollständiger Abdruck der von der Fakultät für Physik der Technischen Universität München zur Erlangung der akademischen Grades eines

Doktors der Naturwissenschaften

genehmigten Dissertation.

Vorsitzende:       Univ.-Prof. Dr. Nora Brambilla

Prüfer der Dissertation:

1. Univ.-Prof. Dr. Ulrich Stroth

2. Univ.-Prof. Dr. Winfried Petry

Die Dissertation wurde am 13.11.2014 bei der Technischen Universität München eingereicht und durch die Fakultät für Physik am 12.01.2015 angenommen.

**Abstract**

Hydrogen plasmas utilized to generate energy producing fusion reactions can create prohibitive large heat and particle fluxes onto the walls around the plasma. Experiments with magnetically confined fusion plasmas in the tokamak ASDEX Upgrade (AUG) have demonstrated that the systematic admission of small amounts of nitrogen to the hydrogen plasma effectively reduces the wall loads by radiative cooling. However, nitrogen from the plasma becomes stored in the tungsten wall surfaces and is released back into the plasma under particle or thermal loads. Hence, a self-consistent model of nitrogen wall retention and fluxes in the plasma is needed to predict the nitrogen puff required to obtain the desired amount of radiation. The first part of this work presents results of laboratory experiments and computer simulations of the nitrogen-tungsten interaction. These results were then used to establish a model for the nitrogen-tungsten interaction and to include it in the WallDYN code. By applying WallDYN to dedicated AUG experiments, it is shown that the WallDYN model correctly describes nitrogen wall retention and fluxes in the plasma.

The laboratory experiments were performed in an X-ray induced photoemission spectroscopy (XPS) setup with in situ sample preparation capabilities provided by ion sources and tunable sample temperature. The measured evolution of the surface nitrogen content under ion bombardment is interpreted by simulations in the binary collision approximation with the SDTrimSP code. To this end, a model to calculate XPS intensity ratios from the elemental depth profiles predicted by SDTrimSP was developed. The comparison of simulated and measured intensity ratios demonstrates that the nitrogen implantation at ambient temperature is well described by SDTrimSP when an effusive loss of nitrogen above a critical concentration is taken into account. The deuterium erosion of tungsten nitride is somewhat overestimated by SDTrimSP. Concerning the temperature dependence of nitrogen retention, a diffusive loss of previously implanted nitrogen is observed only above 800 K. However, the measurements show an unexpected reduction of the nitrogen accumulation already at lower *implantation* temperatures, indicating the occurrence of radiation enhanced diffusion.

Following the verification of the SDTrimSP predictions for nitrogen implantation, such simulations were used to extrapolate the laboratory results to a fusion relevant parameter range. To obtain a model for nitrogen wall retention and fluxes in a fusion plasma, the physical understanding gained from laboratory experiments and SDTrimSP simulation was included into WallDYN-DIVIMP, a code package describing the surface composition evolution and impurity fluxes in fusion experiments.

Finally, nitrogen transport and retention in AUG plasma discharges were studied experimentally. The nitrogen retention in samples exposed to AUG plasmas and spectroscopic measurements are well reproduced by the WallDYN-DIVIMP simulations. In contrast to earlier conclusions also the observed long term nitrogen retention in AUG is correctly extrapolated from the laboratory results. This successful benchmark of WallDYN facilitates the physical interpretation of the AUG experiments via

such simulations. To this end further WallDYN-DIVIMP simulations employing tailored plasma backgrounds and customized input parameters were performed. These indicate that nitrogen fluxes and deposition in the outer divertor were determined by the nitrogen ionization pattern. Furthermore, the simulations show that the core nitrogen concentration is sensitive to all considered parameters: ionization location, temperature gradient force and plasma flows in the X-point region.

## Kurzfassung

Wasserstoffplasmen, die zur Erzeugung von Energie aus Kernfusionsprozessen genutzt werden sollen, können inakzeptabel hohe Teilchen- und Wärmeflüsse auf die das Plasma umgebenden Wände hervorrufen. Untersuchungen an magnetisch eingeschlossenen Fusionsplasmen im Tokamak ASDEX Upgrade (AUG) haben gezeigt, dass das kontrollierte Einbringen kleiner Mengen Stickstoff in das Wasserstoffplasma die Wandbelastung durch Strahlungskühlung deutlich reduziert. Allerdings wird Stickstoff aus dem Plasma in die Oberflächen der umgebenden Wolframwände eingelagert und unter Teilchen- oder Wärmebelastung wieder freigesetzt. Um die Menge an Stickstoff die zum Erreichen der angestrebten Strahlungsmenge notwendig ist zu bestimmen, benötigt man deshalb ein selbstkonsistentes Modell der Stickstoffrückhaltung in den Wänden und der Flüsse im Plasma. Im ersten Teil dieser Arbeit werden die Ergebnisse von Laborexperimenten und Computersimulationen zur Wechselwirkung von Stickstoff und Wolfram vorgestellt. Diese Ergebnisse wurden dann zur Entwicklung eines Modells der Stickstoff-Wolfram Wechselwirkung und dessen Integration in den WallDYN Code verwendet. Die Simulation dedizierter AUG Experimente mit WallDYN zeigt, dass das WallDYN Modell die Stickstoffrückhaltung in den Wänden und die Flüsse im Plasma korrekt beschreibt.

Die Laborexperimente wurden in einer Anlage mit in situ Röntgenphotoelektronenspektroskopie (XPS), Probenpräparation mittels Ionenquellen und einstellbarer Probentemperatur durchgeführt. Die beobachtete Entwicklung des Stickstoffinhalts der Oberfläche unter Ionenbeschuss wird mit Hilfe von SDTrimSP Simulationen erklärt, die auf dem binären Stoßmodell (BCA) basieren. Zu diesem Zweck wurde ein Modell zur Berechnung von XPS-Intensitätsverhältnissen aus von SDTrimSP berechneten Tiefenverteilungen entwickelt. Der Vergleich der simulierten mit den gemessenen Intensitätsverhältnissen zeigt, dass SDTrimSP die Stickstoffimplantation bei Raumtemperatur gut beschreibt wenn berücksichtigt wird, dass Stickstoff nur bis zu einer maximalen Konzentration eingelagert werden kann. Die Erosion von Wolframnitrid durch Deuterium wird von SDTrimSP etwas überschätzt. Im Hinblick auf die Temperaturabhängigkeit der Stickstoffrückhaltung wurde beobachtet, dass die Diffusion erst über 800 K zu einem Verlust von vorher implantiertem Stickstoff führt. Betrachtet man hingegen die Abhängigkeit von der *Implantations*temperatur, zeigen

die Messungen bereits bei geringeren Temperaturen eine unerwartete Abnahme der Stickstoffaufnahme. Dies deutet darauf hin, dass der Ionenbeschuss eine Erhöung der Diffusionsrate induziert.

Nach dieser Verifikation der SDTrimSP Vorhersagen wurde dieser Code benutzt, um die Laborergebnisse in den fusionsrelevanten Parameterbereich zu extrapolieren. Um ein Modell für die Rückhaltung von Stickstoff in den Wänden und die Flüsse in einem Fusionsplasma zu erhalten, wurde das mit Hilfe der Laborexperimente und SDTrimSP Simulationen gewonnene physikalische Verständnis in WallDYN-DIVIMP eingearbeitet, einem Simulationspaket zur Beschreibung der Entwicklung der Oberflächenzusammensetzung und Verunreinigungsflüsse in Fusionsexperimenten.

Schließlich wurden Aufnahme und Transport von Stickstoff in AUG Experimenten untersucht. Sowohl die Aufnahme von Stickstoff in Proben die AUG Plasmen ausgesetzt wurden, als auch spektroskopische Messungen werden von den WallDYN-DIVIMP Simulationen gut reproduziert. Im Gegensatz zu früheren Schlussfolgerungen wird auch die Langzeitrückhaltung von Stickstoff in AUG korrekt aus den Labormessungen extrapoliert. Dieser erfolgreiche Test erlaubt die Verwendung von WallDYN zur physikalischen Interpretation der AUG Experimente. Zu diesem Zweck wurden weitere WallDYN-DIVIMP Simulationen mit angepassten Plasmahintergründen und spezifischen Simulationsparametern durchgeführt. Diese deuten darauf hin, dass Stickstoffflüsse und die Stickstoffeinlagerung im äußeren Divertor durch das Ionisationsprofil von Stickstoff bestimmt werden. Des Weiteren zeigen die Simulationen, dass die Stickstoffkonzentration im Zentralplasma von allen betrachteten Parametern abhängt, dem Ionisationsprofil, der Thermokraft und den Plasmaflüssen im Bereich des X-Punkts.

# Inhaltsverzeichnis

x

# Chapter 1

# Introduction

The exploitation of artificial sources of energy is a key skill of humanity. For the modern civilization a life without energy, especially electric energy, is unthinkable. Unfortunately, the availability of energy is accompanied by a scarceness of the required resources on one side and inherent risks on the other side.

These menaces connected to our energy supply, today especially the shortness of natural resources and global warming, will remain one of the largest challenges in the future. Considering that about 2 billion people do not yet have access to modern energy sources [1], a reduction of the energy consumption is unlikely [2]. Currently, there are two sources which seem capable of solving the world energy problem: renewable energies and fusion of hydrogen nuclei, a copy of the sun's energy source. Both technologies are challenging, where in the case of fusion energy it even remains to be shown that a fusion reactor is technologically feasible.

The attractiveness of nuclear energy arises from the strength of the nuclear force initiating nuclear reactions. The energy scale of such reactions is in the range of mega-electron-volts. This is one million times higher than in the common chemical combustion reactions. The fusion of four protons to one $^4$He nucleus, as it takes place in stars, involves the conversion of protons to neutrons via the weak force and has therefore a very small cross section. In fact, only the cross section for the fusion of deuterium (D) with tritium (T) is sufficiently high to be technologically feasible within the next thirty or forty years [3, 4]. Still, to initiate fusion reactions the D-T mixture must be heated to temperatures of about 100 million Kelvin.

At temperatures above ten thousand Kelvin the electrons of hydrogen atoms are no longer bound to the nuclei and hydrogen gas turns into a plasma. The central objective in magnetic confinement fusion is to confine the D-T plasma by a magnetic field at sufficient temperature and density to reach a self-sustaining fusion plasma. In fusion experiments employing the tokamak configuration sufficient temperatures and densities have already been reached [5]. However, a large variety of plasma instabilities, which increase the transport of plasma across the magnetic field, have

so far prohibited a net energy gain. Only the next generation experiments like ITER will be large enough to generate a surplus of energy.

Another key problem in fusion research is the power and particle load reaching the walls. The power load can mechanically damage the wall material and energetic ions from the plasma erode the surface by sputtering processes. To increase the distance between the hot central plasma and the zone of intense plasma-wall interaction, the so called *divertor configuration* is employed [6]. This configuration directs the plasma to specially designed target plates. Currently the favored material for such divertor target plates is tungsten, which features low erosion rates and good power handling capabilities. Still, the power load onto the walls has to be kept below 5–10 MW/m$^2$ [7]. The divertor configuration has the disadvantage of focusing the plasma flux to a comparably small wall area, so that the material power load limit could easily be exceeded. A possibility to spread the power over a larger area is to radiatively cool the plasma before it reaches the material surface [8].

The radiation emitted from the plasma can be controlled by puffing gases like nitrogen into the plasma [9]. However, a plasma is not a self-contained system, but strongly interacts with the walls. The implantation of nitrogen ions into the walls removes nitrogen from the plasma and induces the formation of tungsten nitride layers [10]. The subsequent re-erosion of nitrogen from such layers causes a history dependent nitrogen flux into the plasma. Therefore, a model for the retention and release of nitrogen from tungsten is required to optimize the radiation control. However, the previous results on formation and stability of tungsten nitride layers under ion bombardment are contradictory [9, 10, 11].

Generally, the wall around a fusion plasma is strongly modified by sputter erosion of the surface and re-deposition of eroded material at a different part of the wall. The chain of material erosion, transport through the plasma, re-deposition and possible re-erosion is called migration [12, 13, 14]. Migration is a key process in the plasma-wall interaction and controls net erosion of the walls, formation of mixed materials and alloys (which may have poor thermo-mechanical properties) and the contamination of the core plasma with impurities (i.e. non-hydrogen isotopes). It also contributes to the retention of radioactive tritium via its incorporation in re-deposited material layers.

In this work results on the migration of nitrogen in the fusion experiment ASDEX Upgrade are presented. The approach taken to study this multifaceted topic is illustrated in Fig. 1.1. As a first step the elementary processes controlling the deposition and erosion of nitrogen in tungsten, the wall material employed in ASDEX Upgrade, are studied. This is done in laboratory experiments with a mass-filtered ion source, controlled sample temperature, in situ X-ray induced photoemission spectroscopy (XPS) analysis and nuclear reaction analysis. The measurements are interpreted by computer simulations with the code SDTrimSP based on the binary collision approximation. The simulation results are converted via a newly developed forward calculation to XPS intensity ratios, which can be directly compared to the
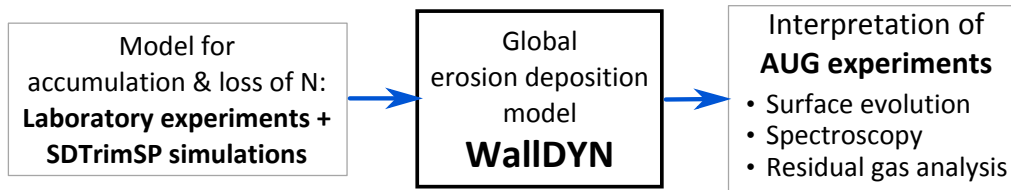
2

| Model for accumulation & loss of N: **Laboratory experiments + SDTrimSP simulations** | → | Global erosion deposition model **WallDYN** | → | Interpretation of **AUG experiments** • Surface evolution • Spectroscopy • Residual gas analysis |

**Figure 1.1:** *WallDYN simulates the evolution of plasma facing surfaces due to erosion and deposition. WallDYN is based on models for the elementary plasma wall interactions and the transport of impurities through the plasma. It allows a direct self-consistent comparison to different diagnostics of nuclear fusion experiments.*

in situ measurements.

In the next step, the established theoretical model is used to include the N-W interaction in the impurity migration simulation code WallDYN (section 3.3.3 and Ref. [15]). The applicability of the results from laboratory experiments to the plasma wall interaction in ASDEX Upgrade was then tested in dedicated ASDEX Upgrade plasma discharges with and without nitrogen seeding. Using the divertor manipulator system, tungsten samples were exposed to divertor plasmas and the nitrogen areal density after the exposure was measured by nuclear reaction analysis. The nitrogen distribution and fluxes in the plasma were monitored spectroscopically and the production of nitrogen containing molecules and pumping of nitrogen by the vacuum system were studied by residual gas analysis. The measurements are compared to WallDYN simulations. The comparison of the spectroscopic measurements is based on a newly implemented synthetic spectroscopy diagnostic based on atomic data. The comparison allows to benchmark the WallDYN model with the extensions added for the present work, to interpret all measurements within a unified self-consistent model and to identify the processes controlling nitrogen migration.

This thesis is structured as follows: Chapter 2 gives an introduction to nuclear fusion, magnetic confinement of fusion plasmas and plasma-wall interaction. The experimental setups and methods used for the present work, like X-ray photoemission spectroscopy, ASDEX Upgrade and computer codes, are introduced in chapter 3. The results from the laboratory experiments and SDTrimSP simulations on the implantation and loss of nitrogen in tungsten are presented in chapter 4 and the results from the ASDEX Upgrade experiments and WallDYN simulations are given in chapter 5. Finally, chapter 6 closes the work with a summary.

Some parts of the present work have already been published in Refs. [16] and [17].

# Chapter 2

# Plasma wall interaction in magnetic confinement fusion experiments

Most of the conventional sources of energy are based on chemical processes induced by electromagnetic forces. In contrast, the fusion of atomic nuclei is caused by the strong nuclear force, so that the energy release per reaction is one million times higher than for chemical reactions. This chapter is intended to give a general introduction to nuclear fusion, magnetic confinement of fusion plasmas and plasma-wall interaction. More detailed discussions can be found in Refs. [3, 5, 7, 8, 18].

## 2.1   Nuclear fusion and magnetic confinement

There are several possible fusion reactions. The most important one for a potential power plant is the fusion of the hydrogen isotopes $^2$H (deuterium, D) and $^3$H (tritium, T) to $^4$He and $^1$n that delivers 17.6 MeV of energy (Fig. 2.1). Thanks to a resonance, this reaction has a comparatively high probability at comparatively low temperatures. However, the required temperature is still about 10 keV[a], which corresponds to about 100 million Kelvin. This high energy is required because the attractive nuclear force has a much shorter range than the electromagnetic force, repelling the positively charged nuclei. The energy in the high keV range required to tunnel trough this barrier can be given to the
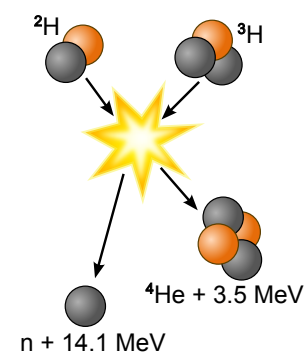


**Figure 2.1:** *Deuterium-Tritium fusion reaction, source: [19].*

---

[a]In plasma physics the temperature is measured in units of energy, i.e. as $k_B$T. A temperature of 1 eV corresponds 11605 K.
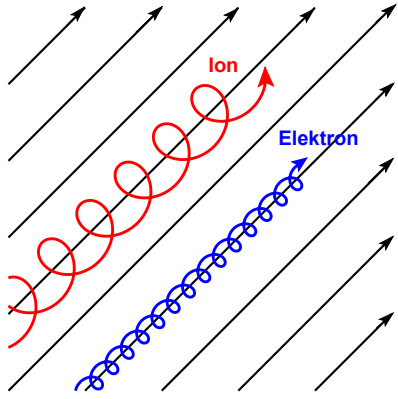
**Figure 2.2:** *Ions and electrons in a strong magnetic field follow the magnetic field lines, source: IPP.*
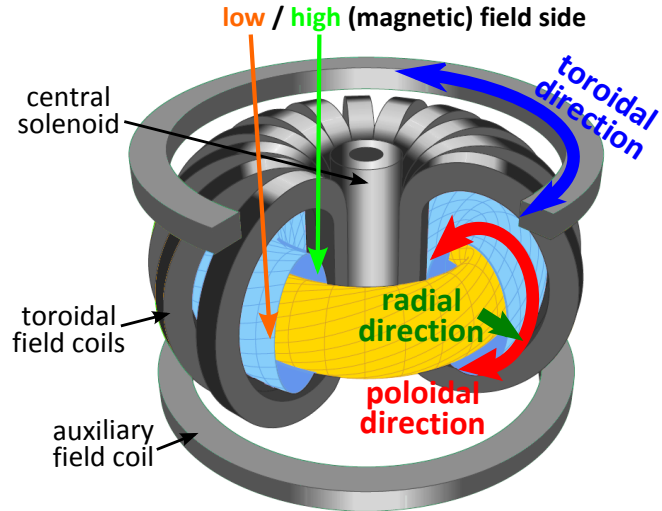


**Figure 2.3:** *Scheme of a tokamak, based on [20].*

nuclei by heating hydrogen gas to very high temperatures [3, Ch. 10].

At such high temperatures, light atoms are fully ionized and in a state called plasma. The confinement of high temperature plasmas is possible by exploiting the Lorentz force $\vec{F} = q\,\vec{v} \times \vec{B}$, acting on particles with charge $q$ and velocity $\vec{v}$ in a magnetic field $\vec{B}$. The resulting motion of the charged particles is a helix along the magnetic field lines as shown in Fig. 2.2 [3]. The motion parallel to a (homogeneous) magnetic field is not altered by the magnetic field, but the guiding center of the particle is forced to follow the magnetic field line. Experiments with a linear magnetic field configuration like mirror machines still have large losses along the magnetic field lines. A better confinement can be reached by bending the magnetic field lines to a torus [21].

Such a toroidal magnetic field is applied in tokamaks [5]. A tokamak and the coordinate system employed in such a device are shown in Fig. 2.3:

- The **toroidal** direction $\phi$ along the torus axis. This is also the direction of the main, 'toroidal', magnetic field.

- The **radial** direction $r$ which points away from the torus axis. The plasma is confined in this direction, i.e. the plasma temperature decreases in the radial direction.

- The **poloidal** direction $\theta$ is perpendicular to the toroidal and the radial direction.

- Because the toroidal magnetic field decays from the central solenoid with $1/R^{\mathrm{b}}$, the side close to the solenoid is called **high field side** and the remote side is

---

$^{\mathrm{b}}R$ is not the radial direction $r$, but the distance from the center of the solenoid as measured in a cylindrical coordinate system.

called **low field side**. Usually poloidal cross sections (like the ones in Figs. 2.4 and 3.9) are given with the high field side to the left and the low field side to the right.

The distinctive feature of a tokamak is that an electric current in the toroidal direction is induced by the central solenoid. This plasma current creates a magnetic field component in the poloidal direction, so that the magnetic field lines twist around the axis of the torus. The poloidal magnetic field is required because charged particles in an inhomogeneous (e.g. bent) magnetic field experience a drift, which separates electrons and positively charged ions [3]. Through the poloidal component of the magnetic field, currents along the magnetic field lines can compensate the charge separation and stabilize the plasma. The plasma current required in a tokamak to create the poloidal magnetic field is a potential source of instabilities and makes a continuous operation challenging. An alternative concept is the stellarator configuration, where also the poloidal magnetic field is created by external magnetic field coils [3]. Although there remain some challenges like instabilities and collisional or turbulent transport across the magnetic field, these concepts of toroidal magnetic confinement are promising.

The present work has been carried out on the tokamak ASDEX Upgrade (see section 3.2.1) at the Max-Planck-Institut für Plasmaphysik. ASDEX Upgrade is a medium size tokamak whose torus has a major radius of 1.65 m and a minor radius of 0.5 m.

## 2.2 Plasma wall interaction in tokamaks

### 2.2.1 Impurity migration

Though the plasma can largely be magnetically confined there remains a, mostly turbulent, transport of the plasma perpendicular to the magnetic fields. This transport not only necessitates the construction of large devices to reach the required energy confinement, but also causes an interaction of the plasma with the surrounding walls. This interaction leads to a surface erosion by energetic ions knocking atoms out of the wall. The net-erosion of the walls can be much smaller than the original gross erosion, because eroded atoms can be re-deposited close to their origin. Therefore, the net material erosion depends on the erosion of atoms from the wall (see section 2.3), the transport through the plasma (see section 2.5), the re-deposition of the atoms at some surface and their potential re-erosion [12, 13, 14]. This chain of processes is called **migration** and is also important for other aspects of the plasma wall interaction:

- When different materials are used for different parts of the walls, migration causes material mixing. This may lead to the formation of alloys with unfavorable properties.

- Radioactive tritium can be incorporated in layers of re-deposited material [22].

- Non-hydrogen isotopes (*impurities*) traveling through the core plasma dilute the hydrogen fuel and lead to increased radiation losses.

Migration is therefore one of the central processes in plasma-wall interaction research. The WallDYN code has been developed to provide an analysis method including the complete migration chain . It self-consistently calculates the impurity fluxes and the composition evolution of the complete first wall surface in a tokamak. WallDYN is described in detail in section 3.3.3.

## 2.2.2 Divertor configuration

The plasma-wall interaction can be better controlled in tokamaks with a so called *divertor* configuration [23, 24]. To understand this configuration it is convenient to use the concept of magnetic flux surfaces: The magnetic field in a tokamak has a toroidal and a poloidal component and therefore winds helically around the torus axis, as indicated in Fig. 2.3. In the common magnetohydrodynamic description of the plasma, the pressure rise towards the plasma center ($\vec{\nabla}p$) has to be balanced by the cross product of current density $\vec{j}$ and magnetic field $\vec{B}$ [3, Ch. 3]:

$$\vec{\nabla}p = \vec{j} \times \vec{B} \tag{2.1}$$

This implies that the magnetic field lines (and the currents) lie on the surfaces of constant pressure. Such a surface can be identified by the enclosed magnetic flux and is called *magnetic flux surface*.

For a divertor configuration one (or more) null-points or "X-points" in the poloidal magnetic field are created (Fig. 2.4a) by external magnetic field coils. With the divertor configuration, the plasma is separated into two different regions: In the center the plasma is confined by closed magnetic flux surfaces. On the outside the magnetic surfaces are diverted to a "divertor", where they intersect the wall (Fig. 2.4a). The magnetic flux surface passing through the X-point, called *separatrix*, separates these two plasma regions [8, Ch. 1]. The intersection of the separatrix with the divertor target plates is called strike line.

The plasma-wall interaction takes place at specially designed divertor target plates, remote from the main plasma [8, p. 212]. The ions outside the separatrix are lost ("scraped off") by the contact with the plasma facing components, mainly the divertor target plates. So the region outside the separatrix is called scrape-off layer (SOL). Having a divertor remote from the main plasma has several advantages. For example the plasma can cool down before reaching the wall, and impurities produced in the divertor cannot easily reach the main plasma [12]. Only a small fraction of the plasma reaches the main wall. This implicates that the heat flux from the plasma may be focused to a small fraction of the available wall area, as
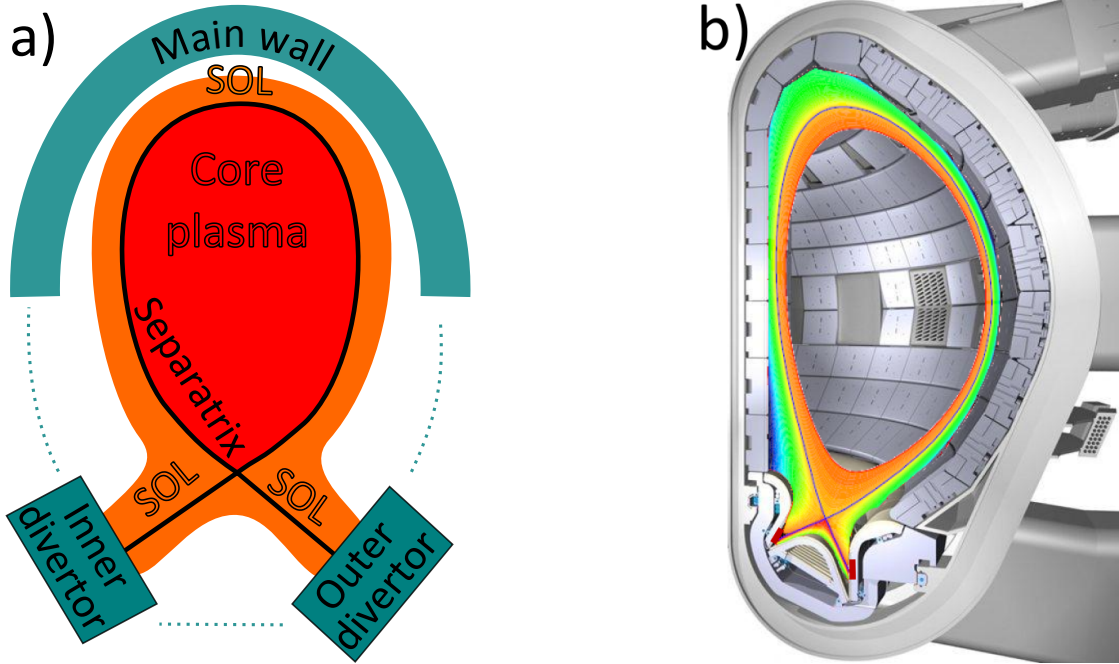
**Figure 2.4:** *The scrape-off layer (SOL) of tokamaks in the divertor configuration. In the left illustration the SOL is shown in orange. The inner divertor is on the high, the outer divertor on the low field side (cf. Fig. 2.3). The right figure illustrates the electron density distribution in a ITER edge plasma. The red marked areas on the divertor target plates denote the small zones of intense plasma wall interaction.*

illustrated in Fig. 2.4b. This figure shows the small zones (red marked wall areas) of interaction between the plasma and the walls predicted for ITER, a large tokamak fusion experiment which is currently under construction. As discussed in sections 2.4 and 2.6, *impurity seeding* can help to distribute the 500 MW of fusion power envisaged for ITER more homogeneously.

## 2.3 Interaction of energetic particles with matter

### 2.3.1 Plasma sheath

The impact parameters of plasma ions impinging on the walls are dominated by the presence of an electrostatic sheath. It develops because of the large discrepancy between the electron and ion masses. The thermal velocity of particles with temperature $T$ and mass $m$ is $v_{th} = \sqrt{2T/m}$. The resulting particle flux density for a particle density $n$ is $\frac{n}{2\sqrt{\pi}} v_{th}$ [3], so that the flux is proportional to $m^{-1/2}$. For an electron-ion plasma in its initial state, where plasma and wall have the same electric potential, the electron wall flux is much larger than the ion wall flux. As a consequence the surface will become negatively charged. The arising electric field repels electrons and

attracts ions until the incoming flux is ambipolar, that means the ion flux equals the electron flux. Under this condition the potential of the wall will drop relative to the plasma potential to the *floating potential* $\Phi_{fl} \approx -(6.7 + \ln 2)\frac{T_e}{2e} \approx -3.7\ T_e/e$, with the electron temperature $T_e$ and the elementary charge $e$ [3].

Because of the large number of mobile charge carriers in a plasma, electric fields are screened on the scale of the Debye length $\lambda_D = \sqrt{\frac{\varepsilon_0 T_e}{n_e e^2}}$. In this expression $\varepsilon_0$ is the permittivity of free space and $n_e$ the electron density. The plasma sheath, generated by the potential difference between plasma and wall, has a thickness of a few Debye length. The Debye length in the edge plasma of a tokamak is of the order of 10 micrometer [3].

The walls of fusion experiments are exposed to an influx of energetic ions. The angle of incidence [25] and the energy of the ions are determined by the electric field from the sheath. For the energy of the ions reaching the wall Ref. [8, Ch. 2] suggests the commonly used formula:

$$E_i = 2\ T_i + 3\ Z \cdot T_e \qquad (2.2)$$

$T_i$ and $T_e$ are the temperatures of ions and electrons in the plasma next to the wall and $Z$ is the charge number of the considered ion. The contribution $2\ T_i$ is due to the original kinetic energy of the ions [3, Ch. 7.1]. Furthermore, the ions are accelerated towards the wall by the sheath voltage of about $3 \cdot T_e/e$ [8, p. 79]. For temperatures in the range from a few eV to about 30 eV and charge numbers varying from one to about five (for nitrogen in its He-like configuration, see Fig. 2.8 for the temperature dependence of the nitrogen charge state), the impact energies vary from a few eV to hundreds of eV.

## 2.3.2   Transport of energetic particles in matter

To understand the erosion and modification of surfaces by energetic particles the transport of energetic particles in matter has to be considered [26, Ch. 6]. The interaction of energetic particles with matter is usually divided into two parts: The interaction of the particles with atomic nuclei and energy loss to the electronic system. The interaction is usually independent of the original charge state of the projectile, as the electron configuration of the projectile in the solid is determined by its interaction with the surrounding matter [26, Ch. 6.2]. This section introduces the common binary collision approximation (BCA) model for the interaction of energetic particles with solids [27]. It is used in codes like SDTrimSP [28, 29], which was also employed for the present work and is described further in section 3.3.1.

The BCA model is applicable to particles with a sufficiently high energy, starting at about 50 eV. Firstly, at these kinetic energies the binding energies are negligible. Secondly, the relevant impact parameters are small in comparison to

the distance between the atoms, such that the projectile only interacts with one target atom at a given time [27]. The BCA model is illustrated in Fig. 2.5:

Between collisions the particles move on straight lines and loose energy by electronic stopping. In the collisions the projectiles are deflected and transfer energy to the respective target atom. The asymptotic trajectories of the projectile and the generated recoil atom are calculated from the classical equation of motion with a screened Coulomb potential. This model does not include an attractive interaction between atoms, but the particles are bound to the matter by the surface binding energy (SBE)[c]. Only particles reaching the surface with a normal energy exceeding the surface binding energy can leave the sample.
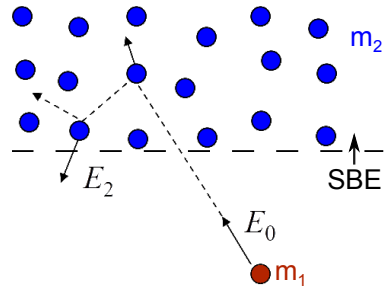


**Figure 2.5:** *In the binary collision approximation the particles move, similar to balls in a billiard game, on straight lines until they collide with another atom. To leave the surface, the kinetic energy of the particles must suffice to overcome the surface binding energy (SBE).*

In these calculations not only the motion of the initial projectiles is considered, but also the motion of recoil atoms generated by the collisions in the target. These recoil atoms may also reach the surface with a normal energy exceeding the SBE and can leave the target. This process causes the sputter erosion of samples exposed to energetic particles.

### 2.3.3 Sputtering and reflection

Mostly one is not interested in the detailed interaction of one single particle with a surface, but in mean values for a large number of particles. Two common quantities to parametrize the interaction of ions and solids are the particle reflection yield and the sputter yield [30].

The particle reflection yield ($RY$) states which fraction of the incoming projectiles is reflected from the target by collisions [8, 30, 31]. The reflection yield for light projectiles impinging on heavier substrates ranges from 0.1 to almost 1 at low projectile energies of about 10 eV and normal incidence and drops with increasing projectile energy. With increasing angle of incidence (measured from the surface normal) the reflection yield increases. Most of the reflected particles leave the surface as neutral atoms.

The fraction $1 - RY$ of the incoming particles comes to rest within the target and is implanted. This, however, does not mean that the particle really remains in the

---

[c]For metals the heat of sublimation is a good estimate for the SBE. However, especially for mixed materials the SBE is mainly a parameter used to fit experimental measurements [27, Ch. 6].
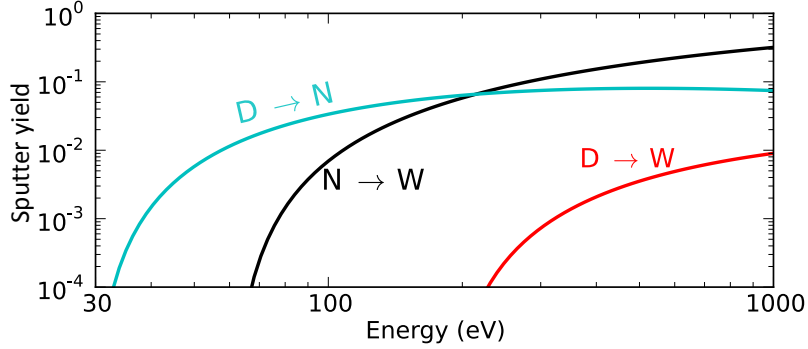
**Figure 2.6:** *Physical sputter yields of tungsten by deuterium (red) and nitrogen (black) and of nitrogen by deuterium (cyan) based on static SDTrimSP calculations.*

target, as diffusive processes still can transport the particles back to the surface.

The sputter yield (SY) states the number of recoil atoms leaving the surface per incident projectile. The sputter yield mainly depends on the projectile species, energy, angle of incidence and the target composition [32].

Physical sputtering is caused by a transfer of momentum from the incoming projectile to the target atoms. The momentum transfer in an elastic collision strongly depends on the mass ratio of the colliding atoms. This dependence on the mass ratio is reflected in the mass dependence of the sputter yields. Especially the sputter yield for a target comprised of heavy atoms by light particles is very low.

The dependence of physical sputtering on the kinetic energy of the projectile ($E$) is well described by the Bohdansky formula [33, 34, 35]:

$$SY_{ei,ej}^{Bohd}(E) = H(E - E_{th}) \cdot Q_0 \cdot s_n^{KrC}(\epsilon) \left(1 - \left(\frac{E_{th}}{E}\right)^{2/3}\right) \left(1 - \frac{E_{th}}{E}\right)^2 \quad (2.3)$$

At low energies there is a threshold energy $E_{th}$, below which there is no physical sputtering and above which the sputter yield rises with increasing energy. This is included in the formula by the Heaviside step function $H(E - E_{th})$, which is zero below the threshold and one above. $Q_0$ is a parameter which is fitted to measured or simulated data. $s_n^{KrC}$ is the nuclear stopping cross section based on the Kr-C interaction potential, which has been found to give a good agreement to experimental data [36]. The stopping cross section depends on the reduced energy

$$\epsilon = E \frac{m_2}{m_1 + m_2} \frac{a_L}{Z_1 Z_2 e^2}$$

with the energy $E$, the masses of the projectile $m_1$ and target atoms $m_2$, the Lindhard screening length $a_L$ and the nuclear charge numbers $Z_1$ and $Z_2$.

Fits of the Bohdansky formula to static SDTrimSP simulations with an impact angle of 60 degree are shown in Fig. 2.6. In this figure one can see the strong rise of the

12

sputter yield directly above the threshold, which depends mainly on the masses of the projectile and the sputtered atom. The threshold energy for sputtering of tungsten by deuterium is about 200 eV. Sputtering of tungsten by nitrogen sets in at a lower energy and remains much more effective at higher energies.

Figure 2.7 shows the amount of sputter eroded particles versus the depth from which the particles were released. The figure is based on a static SDTrimSP calculation with 100 eV D impinging under an angle of 60° to the surface normal on a target consisting of 34 % tungsten, 33 % nitrogen and 33 % boron. One can see that most of the eroded atoms come from the uppermost atomic layer. This demonstrates the sensitivity of the sputter yield to the composition of this layer.
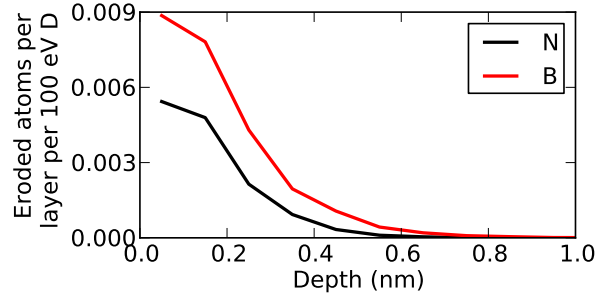


**Figure 2.7:** *Nitrogen and boron (in a tungsten matrix) are eroded almost exclusively from the uppermost nanometer by 100 eV deuterium impinging under 60 degree.*

For targets composed of several species one has to consider their individual partial sputter yields. The partial sputter yield of a species is the number of eroded atoms from this species per projectile. The partial sputter yield of an element are usually proportional to the abundance of this element in the very surface. However, the proportionality factor can be very different. This is the case when species with very different masses (e.g. $N$ and $W$) are mixed and bombarded with a light species like hydrogen isotopes. As already discussed, the momentum transfer from the light projectile to the heavy $W$ atom is rather ineffective, so the sputter yield of $W$ by $D$ is much smaller than the sputter yield of $N$ by $D$. If the material is initially a homogeneous mix of N and W, the initial erosion of $N$ is higher than of $W$. The preferential erosion of species $N$ continues until an equilibrium surface composition is approached, where the enrichment of species $W$ in the surface compensates for the smaller proportionality factor.

As mentioned above, the sputter yield depends on the incidence angle of the projectile. From a minimum for normal incidence the sputter yield rises with increasing angle of impact until there is a sharp drop for angles larger than about 80° [35]. In a tokamak, the angle of incidence depends on the magnetic field, the surface morphology and the mass and charge state of the ion. Based on Ref. [25], a typical angle of incidence under tokamak divertor conditions is around 60 degree.

A special situation, called *chemical erosion*, can occur when the projectile species form volatile molecules with the target material [30]. In this case, in addition to physical sputtering, the particle flux induces the formation of volatile molecules which desorb from the surface and thereby remove material. As nitrogen and hydrogen form ammonia, the erosion of nitrogen by deuterium could be increased by

this chemical reaction over the base value given by physical sputtering. Indications for the chemical erosion of nitrogen implanted into beryllium by deuterium have been found at PISCES-B experiments [37].

## 2.4 Scrape-off layer: Power exhaust, particle transport and plasma flows

In a magnetized plasma the radial transport is many orders of magnitudes smaller than the parallel transport [38]. On the one hand, this provides the desired, good energy confinement in the core plasma. On the other hand, "the confinement is rather *too good* for the SOL plasma" [8, p. 10], yielding a very thin SOL and a very small zone with an intense interaction of the plasma with the wall. All the heating power that is transported from the plasma core to the wall via heat conduction is deposited on a very small fraction of the first wall [7, 39] as indicated in Fig. 2.4b. The resulting heat flux density could therefore easily exceed material limits of about 5 MW/m² [7].

The heat flux from the plasma is transmitted to the wall via the energies of ions and electrons. The mean kinetic energy of an ion impinging on the wall has already been given in equation (2.2). The mean energy of an electron is $2\,T_e$, because the electrons crossing the plasma sheath (section 2.3.1) maintain their Maxwellian distribution with temperature $T_e$ [8, Ch. 2.8], [3, Ch. 7.1]. The particle flux $\Gamma_n$ is the same for electrons and ions because of the ambipolarity condition enforced by the sheath. Assuming a common temperature $T$ of electrons and ions the resulting heat flux density $q$ to the wall is:

$$q = \left( \gamma\, T + \epsilon_{pot} \right)\, \Gamma_n \qquad (2.4)$$

In this equation $\gamma \approx 2+2+3 = 7$ summarizes the kinetic energies from the electrons and the (singly ionized) ions and $\epsilon_{pot}$ is the potential energy per incident ion [23, section 5.2]. Please note that the value for the sheath heat transmission coefficient $\gamma$ depends on the underlying model and may vary significantly [40].

Under experimental conditions the heat flux is fixed by the heating power and the plasma temperature adjusts to the given heat flux. Because the sputter yield depends strongly on the energy of the impinging ions which again depends on the plasma temperature via equation (2.2), the sputter erosion of the divertor targets is closely related to the local heat flux density.

A better distribution of the power flux to the available wall area and a reduction of the divertor plasma temperature can be achieved by emitting power from the plasma via radiation. Radiated power is not bound to the magnetic field and hence homogeneously distributed over the surrounding walls. The control of the radiated

power by impurity seeding is described in section 2.6. Because the sputter yield is closely related to the heat flux, impurity seeding also can reduce material erosion. However, the plasma temperature must drop sufficiently to overcome the increased sputter yield caused by the heavy impurity ions (see section 5.5).

To study the plasma-wall interaction and the transport of impurities through the plasma it is necessary to reconstruct or even predict the SOL plasma parameters. Because the plasma parameters can at best be measured at a few poloidal positions[d], plasma models are required to interpolate the measured data. Such models have to include the collisional transport parallel to the magnetic field, the (original turbulent) transport perpendicular to the magnetic field, the complex geometry and atomic or even molecular physics. The models used to reconstruct the plasma parameters range from the rather simple two-point model [23] to sophisticated simulation packages like SOLPS [41]. The reconstruction of the plasma parameters is further discussed in section 3.3.5.

As will be discussed in section 2.5, the parallel ion flow profile in the SOL is an important factor in determining impurity transport. Typically the flows in the divertor region are directed towards the particle sink at the divertor target plates [13]. However, under certain conditions also a reversal of the flows can occur [41]. Measurements of the ion flow in divertor tokamaks show that the parallel velocity of the ions in most of the upper SOL points towards the inner divertor target and is of the order of the speed of sound [12]. It has been found that the flows calculated with plasma edge physics codes like SOLPS do not correctly reproduce this observation. Improvements in the simulated flow pattern could be reached by including classical drifts and ballooning transport in the simulations. Still, the simulated flows are smaller than the measured ones [42, 43, 44, 45].

## 2.5   Transport of impurities in a divertor tokamak plasma

An important step in the migration of impurities (see section 2.2) is their transport through the plasma. The SOL transport determines where the impurities are re-deposited and which, typically small, percentage of the impurity ions enters the core plasma. For the impurity contamination of the core plasma also the transport in this region with closed magnetic field lines can be important [46, 47, 48, 49]. However, this work focuses on the transport of impurities in the SOL.

Depending on whether an impurity atom is neutral or ionized, its transport in a magnetized plasma is controlled by very different mechanisms. Particles start from

---

[d]Typically radial profiles of electron density and temperature at the divertor target plates and one upstream position are measured.

the walls (or valves for puffed species) as neutral atoms or molecules. Neutrals essentially travel along straight lines until they are ionized by collisions with electrons or hit a wall. For ions a larger number of processes has to be considered: further ionization and recombination processes, the guidance of the ion by the magnetic field, collisions with other charged particles and turbulent transport. The ionization and recombination is described by rate coefficients, which are mostly taken from ADAS [50], and depend on the electron density and temperature. The motion of the ions parallel to the magnetic field is, apart from small effects like the mirror force, largely free and controlled by collisions with other ions and electrons. Assuming that collisions with a large impact parameter dominate, this motion can be described by the Fokker-Planck-Landau equation [51]. As this kinetic description is computationally very costly, the edge plasma is mostly described in the fluid approximation [3, 52]. The plasma temperatures and thereby the ion mean free paths in the SOL are mostly short enough to permit this description, though kinetic effects may still play a role [45, 53].

As explained in section 2.1, the dominating motion perpendicular to the magnetic field is gyro-orbiting, while the guiding centers of the ions are bound to a magnetic field line. Only due to collisions with other ions or guiding center drifts, caused for instance by electric fields, particles depart from their original magnetic field line. The current understanding of the mainly turbulent perpendicular transport is still, especially in the SOL region, at best qualitative. For this reason the perpendicular transport is mostly modeled by a diffusive description, with a typical diffusion coefficient of $D = 1$ m$^2$s$^{-1}$ [26, Ch. 5.5].

For impurity transport studies, a common approach is to specify the parameters of a hydrogen plasma $H$ and then to calculate the motion of impurities on this "plasma background". The dominating forces $F_I$ acting on an impurity ion $I$ parallel to the magnetic fields are [8, p. 298], [54]:

- The *impurity pressure gradient force*, acting towards a constant impurity pressure $p_I$ along a field line: $F_I \propto -\dfrac{dp_I}{ds}$

- The *electrostatic force* caused by a parallel electric field: $F_I = Z_I e E_{||}$

- The *friction force* caused by momentum transfer collisions and depending on the difference in velocity: $F_I \propto (V_H - V_I)$

- The *electron* and *ion temperature gradient forces*: $F_I \propto Z^2 \dfrac{dT_{e/H}}{ds}$

The last force is a peculiarity of particles interacting via the Coulomb force. The Rutherford cross section for the interaction of charged particles is proportional to $1/u^2$, where $u$ is the relative velocity. This causes a $u^{-3} \propto T^{-3/2}$ dependence of the momentum transfer cross section [3, ch. 8]. In a plasma with a temperature gradient parallel to the magnetic field, the particles coming from the hot side transfer less

16

momentum to the considered ion than the ones coming from the cold side. This leads to a net force pushing impurities in the direction of the gradients of background temperature gradients towards higher temperatures [52]. Because the temperatures of the background ions ($T_H$) and the electrons ($T_e$) may be different one has to consider their contributions to the temperature gradient force separately.

For a better fusion performance one wants to keep the impurity content in the core plasma as low as possible. For this reason the friction force is of large importance [55, 43]. The mean velocity of the background ions is directed towards the divertor target plates in the divertor region and mostly towards the inner divertor in the main SOL (see section 2.4). Therefore the friction force counteracts the temperature gradient force in the divertor region and improves impurity retention in the divertor. Comparisons of impurity injection experiments with computer simulations found that also the flows in upper SOL are important for the migration of impurities. For impurities originating from the upper wall region, these flows lead to a dominant transport and deposition in the inner divertor [12, 13, 14, 56, 57].

A common challenge in the computation of plasma parameters and impurity transport is the description of the (turbulent) transport perpendicular to the magnetic field. In the plasma center, gyrokinetic simulations can describe the turbulent fluxes within the uncertainties [58]. However, in the edge and SOL region this approach is not valid due to additional complications like X-point geometry, magnetic field lines intersecting the walls, steep gradients and the occurrence of atomic processes. Nevertheless, some progress has been made by recognizing that the drift motion of the ions [3] can contribute to the cross field transport of deuterium [8] and impurities [59].

## 2.6 Plasma facing materials and application of nitrogen in fusion experiments

Radiation emitted from the plasma reduces the heat flux to the divertor targets (see section 2.4). However, the radiation should not be emitted from the core plasma to retain a good energy confinement in this region. The location from where radiation is emitted can actually be controlled by adding impurities to the plasma. Figure 2.8 shows the fractional abundance of nitrogen charge states in a plasma. Up to about 200 eV nitrogen is only partly ionized and emits line radiation. In the core plasma light elements like nitrogen are fully ionized and cannot emit line radiation, so that the acceptable concentration is limited by the dilution of the hydrogen fuel and lies in the low percent range [60]. Figure 2.8 gives fractional abundances based on two different approaches: The solid lines depict the charge state distribution in thermal equilibrium calculated by ADAS [50]. In contrast, the dashed lines are

17

taken from a DIVIMP simulation[e], which includes the modification of the charge state distribution by transport effects. The differences between these curves show that simple calculations of the charge state distribution and emitted radiation with equilibrium models only yield a first approximation and sophisticated models like DIVIMP are required for a quantitative analysis.
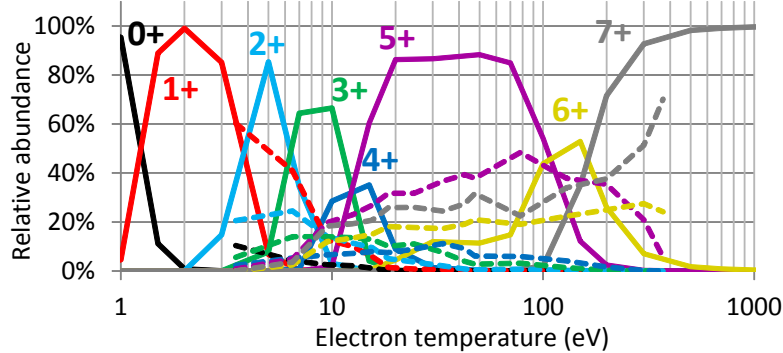


**Figure 2.8:** *Fractional abundance of the nitrogen charge states versus the electron temperature, calculated with ADAS [50] (solid lines) and from a DIVIMP (dashed lines, see section 3.3.4) simulation. ADAS assumes that the charge state distribution is in coronal equilibrium while DIVIMP includes transport effects. This broadens especially the abundance of the high charge states.*

For a long time carbon was used as wall material for fusion experiments and acted as edge radiator [9]. However, carbon cannot be used in a fusion reactor, because it causes a high tritium retention, is strongly eroded by deuterium and degrades under neutron irradiation [7]. The current materials of choice are metals, especially tungsten with an atomic number of 74. Tungsten is expected to have a low tritium retention, is hardly sputtered by deuterium (see section 2.3.3) and has a high melting point [7]. However, the maximum tungsten concentration tolerable in the core of a fusion reactor is about $10^{-5}$. This constrains the acceptable sputter yields and thereby the plasma temperature at the wall. The use of tungsten as plasma facing material also necessitates a manual control of the radiated power by puffing impurities into the plasma [61].

In ASDEX Upgrade, the first tokamak using a full tungsten wall (see section 3.2), nitrogen has been established as optimal choice to control the radiated power [9, 62] and is now also used at the Joint European Torus (JET) [63]. For a given particle energy the sputtering of tungsten by nitrogen is much higher than by deuterium (Fig. 2.6). Nevertheless, Ref. [64] and Fig. 5.24 show that nitrogen seeding reduces the sputter erosion by lowering the plasma temperature and thereby the energy of the ions impinging on the walls. In comparison to noble gases, which also can be used to control the radiated power, the nitrogen content in the plasma shows a history effect [62]. That means the nitrogen content in the plasma depends not only

---

[e]DIVIMP is introduced in section 3.3.4. No regions with very low or very high temperatures were present in the applied plasma background, which is shown in Fig. D.2.

on the currently applied nitrogen puff but also on the nitrogen puff applied in the previous discharges. This history effect is caused by the storage of nitrogen in and release from the surfaces.

Apart from its application to control the radiated amount of power, nitrogen also has been employed to study the transport of impurities in tokamaks [14]. Nitrogen is well suited for such studies as it is easy to handle and tolerated by the plasma. In Ref. [65], $^{15}$N was injected into AUG from the low field side directly before a vessel opening. During the vessel opening some of the wall tiles were removed and the $^{15}$N deposition pattern was measured. These measurements showed that the deposition, for the chosen injection location on the low field side wall, is toroidally asymmetric and governed by the intersections of the magnetic field lines with the walls [57].

## 2.7 Retention of nitrogen in ASDEX Upgrade and formation of tungsten nitride

The previous examples indicate that nitrogen adds some complexity to the plasma-wall interaction. Ref. [10] suggested, in agreement with the experimental results presented in Refs. [9, 11, 62, 57, 65, 66] and with results on tungsten nitride from other areas of research, e.g. Refs. [67, 68, 69, 70, 71], the following picture: Nitrogen as a gas cannot, different from carbon or metals, form layers on top of the original wall material. Still nitrogen which is implanted into the tungsten surface can be chemically bound there up to a maximum concentration of 50 %. As nitrogen only starts to diffuse in tungsten at rather high temperatures (see section 4.1.3), the formation of tungsten nitride by ion implantation is restricted to the implantation range of a few nanometers.

Still, some questions on the nitrogen retention and release remained unresolved. Firstly, the nitrogen saturation areal density deduced (indirectly) from AUG measurement, is by a factor of ten larger than the saturation areal density measured in laboratory experiments [9, 62]. Suggested explanations for this increased nitrogen retention were the roughness of the wall tiles or co-deposition of nitrogen with re-deposited wall material.

The already mentioned $^{15}$N experiments (Refs. [65, 57]) raised some questions, too. On one hand the $^{15}$N deposition is more homogeneous than the $^{13}$C deposition measured in the same experiment [14], indicating a saturation of the $^{15}$N deposition. On the other hand the $^{15}$N areal densities are partly above the values expected from the laboratory experiments [10]. However, these high areal densities are measured at positions where also significant amounts of $^{13}$C, which was injected together with the $^{15}$N, have been found. Therefore, it is likely that N+C co-deposits have formed and the measured $^{15}$N areal densities cannot be compared to laboratory experiments on pure W.

Furthermore, the results concerning the temperature dependence of formation and stability of tungsten nitride layers under nitrogen bombardment are contradictory [10, 11]. The temperature stability of tungsten nitride is an important question for the application of nitrogen in fusion experiments, as a sudden release of large amounts of nitrogen from the walls could terminate the plasma operation. Another open question is the erosion of tungsten nitride layers by deuterium, the most abundant species in fusion plasmas, which has not been measured yet. Finally, Ref. [72] observed the formation of ammonia in ASDEX Upgrade, so that sticking of ammonia to the walls could also contribute to nitrogen retention in ASDEX Upgrade. An improved understanding of these processes is desirable to deduce the nitrogen fluxes in the plasma, to predict the erosion of the walls and the hydrogen retention [73, 74], and to improve the feedback control for radiative cooling.

# Chapter 3

# Methods

## 3.1 Laboratory experiments

### 3.1.1 X-ray photoemission spectroscopy

Under irradiation with electromagnetic waves, materials emit electrons if the frequency of the light, i.e. the energy of the photons, surpasses a certain threshold. This so called photoelectric effect was discovered by H. Hertz [75] and explained by A. Einstein [76] around 1900. In this interaction the complete energy of a photon is transferred to one electron. Photoemission spectroscopy utilizes this effect to determine the binding energy of electrons. The binding energy can be calculated from the kinetic energy of the emitted electrons as illustrated in Fig. 3.1:

$$
\begin{aligned}
\hbar\omega &= E_{Kin}^{S} + \Phi_S + E_B^F = E_{Kin}^{D} + \Phi_D + E_B^F \\
&\Rightarrow E_B^F = \hbar\omega - E_{Kin}^{D} - \Phi_D
\end{aligned}
\tag{3.1}
$$

where $E_B^F$ is the binding energy of the electron relative to the common Fermi level of detector and sample, $\hbar\omega$ the energy of the photon, $\Phi_D$ the work function of the detector, $\Phi_S$ the work function of the sample (which is not required for the calculation of $E_B^F$), $E_{Kin}^{D}$ the kinetic energy at the detector and $E_{Kin}^{S}$ the kinetic energy at the sample surface [77]. The kinetic energy at the detector $E_{Kin}^{D}$ is different from the kinetic energy at the sample surface $E_{Kin}^{S}$ because the contact potential $\Phi_S - \Phi_D$ between the sample surface and the analyzer acts on the electrons [78].

It should be mentioned that the measured binding energy is the difference between the total energy of the final state with $N-1$ electrons ($E_f^{N-1}$) and the total energy of the $N$ electron system in the initial state ($E_i^N$) [80]. When the photoemitted electron leaves the atom, the remaining $N-1$ electron orbitals usually rearrange to reduce their energy. Therefore the binding energy $E_B = E_f^{N-1} - E_i^N$, including the
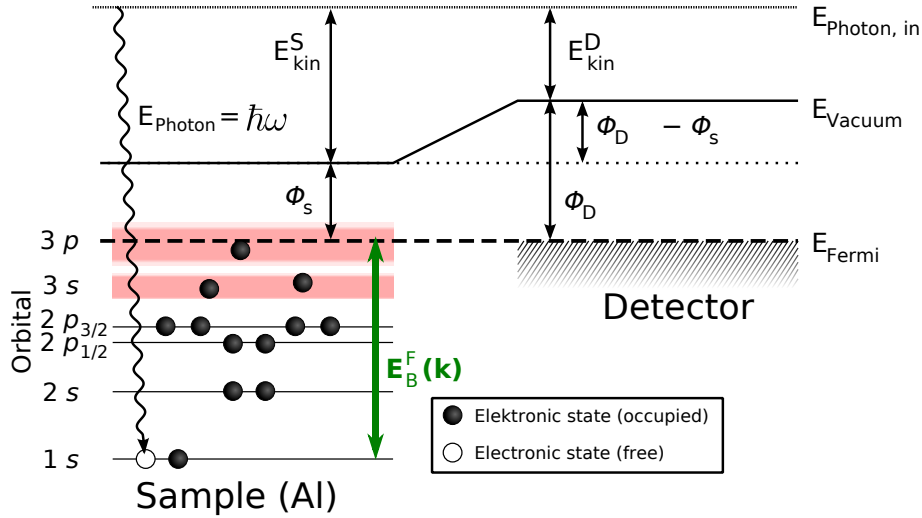
**Figure 3.1:** *The binding energy of a photoelectron can be calculated by subtracting the kinetic energy at the detector and the work function of the detector from the energy of the original photon (based on [79]).*

relaxation energy, is not identical to the orbital energy from which the electron was emitted. The binding energy of an electron depends on the chemical environment of the emitting atom, so measurements of the binding energy with high resolution can help to identify the chemical phase of the observed element [81].

A very popular kind of photoemission spectroscopy uses photons in the X-ray range with an energy of the order of 1 keV [81, 82], so that core levels of all elements may be observed. This technique is called *X-ray induced photoemission spectroscopy, XPS.*

A common approach for the interpretation of photoemission spectra from solids is the *three-step model* [80, 83]. In this model it is assumed that the photoemission process can be split into three independent parts: Absorption of the incoming photon by an electron which becomes excited from its initial state to a final state, the transport of the electron to the sample surface and the emission of the electron into the vacuum.

The number of created photoelectrons can be calculated from the density of the considered element, its photoionization cross section and the incoming photon flux. X-ray photons at 1.5 keV penetrate into depths of more than 100 nm, so that the photon flux can be assumed to be constant over the depth probed by XPS. The XPS information depth is limited by inelastic collisions of the photoelectrons, mostly with weakly bound electrons in the valence or conduction band [84, p. 144]. The electron transport is described by the electron inelastic mean free path $\lambda$, which is a function of the electron energy and the sample composition. The inelastic mean free path is very short, in tungsten it is between 1–2 nm for electrons with 1–1.5 keV. This short inelastic mean free path is responsible for the high surface sensitivity of photoemission spectroscopy. The transmission of the electrons into the vacuum changes the perpendicular momentum of the electron and is therefore an important process for

the measurement of band structures by angle resolved photoemission spectroscopy. For the quantitative analysis of X-Ray induced Photoemission Spectroscopy this step is usually neglected.

A further effect that has to be considered in actual measurements is the transmission function of the detector. The percentage of electrons which reach the detector and are then counted depends on the kinetic energy of the electrons. The actual intensity measured in an XPS system can be calculated by the following equation [82]:

$$I_A/t = \sigma_{A,\omega} \cdot L_{A,\omega,\rho,\alpha,\gamma} \cdot \Gamma_{Phot} \cdot T_{A,\omega} \int_0^\infty \rho_A(z) \exp\left(-\int_0^z \frac{1}{\lambda_{\rho(z'),\omega,A} \cdot \cos\alpha} dz'\right) dz$$
(3.2)

where $I_A/t$ $[1/s]$ denotes the intensity of peak A per time, $\sigma_{A,\omega}$ $[m^2]$ the orbital and energy $(\hbar\omega)$ dependent total cross section, $L_{A,\omega,\rho,\alpha,\gamma}$ the angular dependence, $\rho_A(z)$ $[1/m^3]$ the depth dependent number density of the element that generates peak A, $\alpha$ the angle between detector and sample normal, $\gamma$ the angle between the incoming photons and the electron detector, $\lambda(\rho)$ $[m]$ the electron inelastic mean free path (IMFP) (which depends on the local composition of the sample and the energy of the electrons), $\Gamma_{Phot}$ $[1/s]$ is the incident photon flux which cancels in the observation of intensity ratios and $T_{A,\omega}$ the detector transmission function. A computer model to actually calculate the intensities is presented in section 3.3.2.

**Evaluation of XPS measurements**

In the previous section the generation of the peaks in the XPS spectrum was discussed. In this section the two steps required to extract the peak intensities (i.e. peak areas) from measured spectra are discussed: First the background caused by inelastically scattered electrons must be removed. Second the remaining signal must be attributed to the different peaks.

An XPS spectrum from a N-implanted W sample is shown in Fig. 3.2a. Originally the kinetic energy of the electrons is measured, but typically the intensity is not given as a function of the kinetic energy, but of the binding energy ($E_B = \hbar\omega - E_{Kin} - \Phi_D$). The spectrum consists of four strong W peaks, W 4*f*, W 4*d*, W 4*p* and W 4*s*, one strong nitrogen peak and some smaller peaks like the valence band at a few eV binding energy.

Peaks from orbitals with nonzero orbital angular momentum **l**, like W 4*f*, W 4*d* and W 4*p*, are doublet peaks [82]. When one electron is removed from an orbital, the remaining electron can have either spin up or down. The spin and the orbital angular momentum couple to the total angular momentum **j**, which can be either **l**+1/2 or **l**−1/2 and determines the final state energy of the electron system. The number of degenerated substates available for a given state **j** is 2**j**+1 and determines
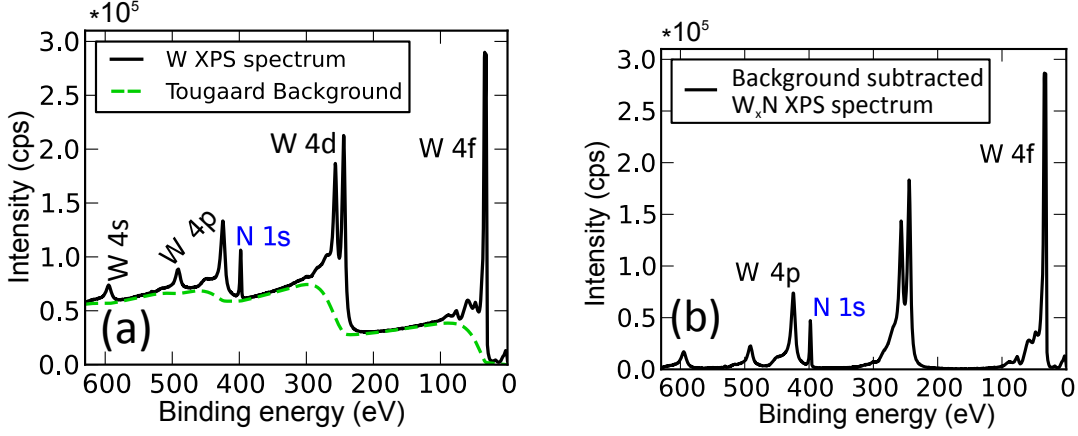
23

**Figure 3.2:** *The XPS spectrum of N-ion implanted W in (a) is dominated by tungsten peaks. The N 1s peak is still nicely visible, the N 2s peak at 18 eV is very small. The Tougaard background gives a good fit to the spectrum and removes most of the background (b).*

the intensity ratio of the doublet. For example the W 4$f$ (**l**=3) peak splits into W 4$f_{7/2}$ and W 4$f_{5/2}$ with an intensity ratio of $\dfrac{I_{7/2}}{I_{5/2}} = \dfrac{2 \cdot 7/2 + 1}{2 \cdot 5/2 + 1} = \dfrac{4}{3}$.

## Background Subtraction

In the following, the generation and subtraction methods for the background in XPS will be discussed. Then the background subtraction chosen for this work and the method for the separation of the N 1$s$ peak from a nearby tungsten peak will be presented. A sketch of all the steps taken in the evaluation of the measured intensities is given in Fig. 3.3.

As already explained, electrons in a solid travel only very short distances before they loose energy in inelastic collisions. The energy loss per inelastic collision is of the order of 30 eV [84, 86]. That means the electrons only loose a small fraction of their initial energy of about 1 keV. For this reason each peak contributes to the background on its lower kinetic energy (higher binding energy) side, as described by the following equation [87]:

$$Bg(E) = \int_{E}^{\infty} K(E' - E)I(E') \, dE' \tag{3.3}$$

where $Bg(E)$ is the background at kinetic energy $E$, which receives contributions from the spectrum at higher kinetic energies $I(E')$. $E' - E$ is the energy transfer in the collision, $K(E' - E)$ is the normalized differential inverse inelastic mean free path, which is approximately independent of the kinetic energy of the electron $E'$ [84].
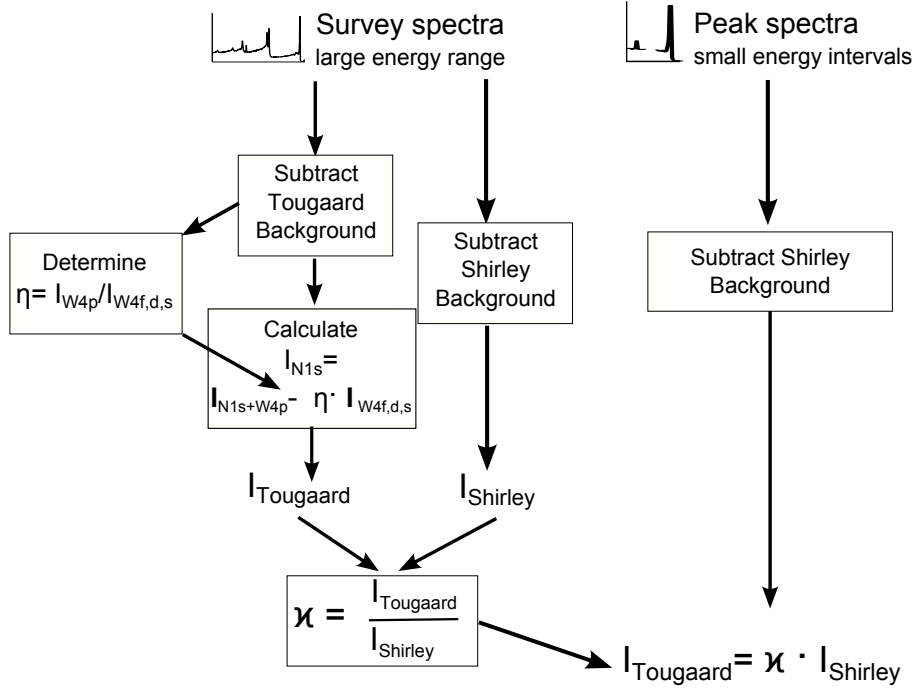
**Figure 3.3:** *During the ion bombardments and temperature ramps only the energy intervals containing the N 1s and the W 4f peak are measured. To correctly deduce the intensities from these measurements a calibration factor is determined from a series of of Survey spectra.*

Two widely used types of backgrounds for XPS spectra of metals are the Shirley background [88] and the Tougaard background [87]. The Shirley background was originally proposed on an empirical basis, but may also be derived from equation (3.3) [89]. An advantage of the Shirley background is, that it can be applied even when only small intervals around the peaks have been measured. However, mainly because start and end points of the background calculation are chosen individually for each peak, the derived intensities may be flawed as illustrated in Fig. 3.4, which is taken from Ref. [85].

The Tougaard Background is directly based on equation (3.3) with a universal cross section for the inelastic electron scattering [86]:

$$K(E' - E) = \frac{B\,(E' - E)}{\left(C + (E' - E)^2\right)^2} \qquad (3.4)$$

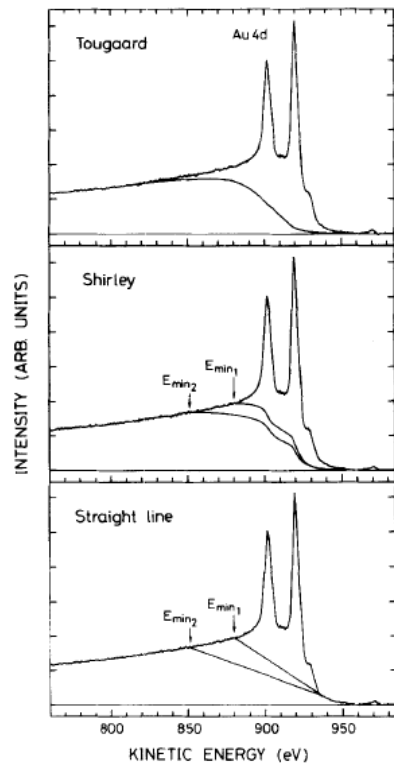This universal cross section does not include special features like plasmon excitation and depends



**Figure 3.4:** *Comparison of background subtraction methods for the Au 4d doublet, from Ref. [85].*

on two parameters, for which the values $B = 2866$ and $C = 1643$ were suggested in Ref. [86]. The analysis of Ref. [90] shows that intensity ratios derived with the Tougaard background are essentially independent of the chosen set of parameters, when they are chosen to fit the background in energy intervals without peaks. Strictly this background subtraction is only valid for homogeneous materials, as it assumes that every peak gives the same contribution to the background. However, the background of N implanted and pure W samples agrees within the scatter observed for pure W surfaces, so this simple background subtraction should still be applicable. To include the composition dependence of background, a full calculation of the spectrum, including the background, would be necessary.

As can be seen in Fig. 3.2 the inelastic background could be well fitted with a Tougaard background with the standard parameters $B = 2866$ and $C = 1643$ [86]. The intensity of the W $4f$ peak was determined by integrating the background subtracted spectrum from 21.5 to 130 eV[a].

## Separation of N 1$s$ and W 4$p$

The determination of the N 1$s$ intensity is more involved. The plasmon loss signal of the N 1$s$ core level is superimposed by the signal of the W $4p$ core level ($4p_{1/2}$ at 490 eV and $4p_{3/2}$ at 425 eV; see Fig. 3.2). However, the plasmon loss signal of the W $4f$ peak is included in the determined intensity. So for a consistent evaluation also the plasma loss signal of the N 1$s$ peak has to be included in this peak intensity.

According to a forward calculations for XPS intensities, see section 3.3.2, the intensity ratio of the different W peaks (W $4f$, W $4d$, W $4p$ & W $4s$) changes only by about one percent during N implantation. Also experimentally it was checked that the ratio of the W $4s$ intensity to the W $4f$ intensity does not change due to the N implantation. Therefore, the W $4p$ intensity can be calculated from the intensity of other tungsten peaks. Then the N 1$s$ intensity can be deduced by subtracting the W $4p$ intensity from the combined intensity of the N 1$s$ and the W $4p$ peaks.

The ratios $\eta$ of the W $4p$ intensity to the intensities of the W $4f$, W $4d$ and W $4s$ peaks were determined from a measurement of pure tungsten and agree within less than 10 % with the values calculated by the forward calculation. Subsequently, a set of spectra including samples that had been implanted with different energies and fluences of nitrogen was examined. For this set again the intensities of the W $4f$, W $4d$ and W $4s$ peaks were determined after a Tougaard background subtraction. Furthermore, the energy interval from 388 to 525 eV was integrated, corresponding to the combined intensities of W $4p$ and N 1$s$. An estimate for the W $4p$ intensity was calculated with the previously determined W peak intensities and $\eta$ ratios W $4p$/W $4f$, W $4p$/W $4d$ and W $4p$/W $4s$. Finally, the N 1$s$ intensity was obtained by subtracting the estimate for W $4p$ from the combined intensities of W $4p$ and N 1$s$.

---

[a]This range includes also the small W $5s$ and W $5p$ peaks. Consequently these peaks are included in the forward calculation with a contribution of about 10 % to the intensity.

## Calibration factor for Shirley background

The measurement of the large energy interval required for the application of the Tougaard background increases the required experimental integration time with detrimental effects on the cleanliness of the surface and number of available measurements. To reduce the effort required for further measurements, another step was taken: For the above mentioned set of spectra the N $1s$ and W $4f$ peak intensities were additionally determined subtracting a Shirley background with integration regions of 393 to 405 eV for the N $1s$ and 26 to 44 eV for the W $4f$ peak.

The ratios of the intensities determined from the procedure using Tougaard backgrounds to the ones determined with a Shirley background are shown in Fig. 3.5. The regression curves confirm that the ratios are constant within the scatter of the data. Using these ratios as calibration factors, it is finally possible to determine intensity ratios with the Shirley background, where the dependence on user chosen parameters has been eliminated and the contributions to the N $1s$ peak located in the region of the W $4p$ peak are included. Exploiting the advantage of the Shirley background, that the measurement of small energy intervals is sufficient, allowed to reach good counting statistics in a short time. The derived calibration factors change the intensity ratio N $1s$/W $4f$ by the factor $2.7/1.9 = 1.4$. That means a direct use of the intensities based on a Shirley background subtraction underestimates the intensity ratio by 40 %.
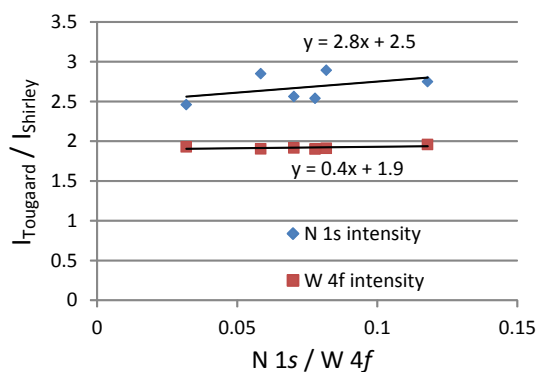


**Figure 3.5:** *The intensities from Shirley and Tougaard background subtraction have a constant ratio of 1.9 for W 4f and 2.7 for N 1s.*

## Interpretation of XPS measurements

The method explained in the last section allows to deduce the N $1s$ / W $4f$ intensity ratio from measured spectra. For homogeneous materials the composition can be deduced from this intensity ratio by using relative sensitivity factors [91]. However, materials, especially if they are studied by XPS, are rarely homogeneous. The inversion of the exponentially weighted averages for depth resolved XPS measurements is difficult[b] [92]. In contrast, the conversion of a given depth profile (assuming lat-

---

[b]This of course requires to measure data with varying contributions from different depths. Such data can be obtained by varying the angle between sample normal and the detector, comparing intensities of peaks from one element with different binding energies or varying the energy of the incoming photons. The possible variation of the angle and the peak energy are limited. The variation of the photon energy is possible in a synchrotron source but the contribution is always

eral homogeneity) to XPS intensity ratios is possible by applying the formula (3.2). That means it is very difficult to derive a depth profile from XPS measurements, but checking the consistency of a given depth profile with XPS measurements is possible.

Earlier studies [10] indicate that the bombardment of W by N is correctly described by SDTrimSP (see section 3.3.1). The approach taken in this work was to compare the fluence dependent XPS intensity ratios from measurements with intensity ratios calculated via a forward model from SDTrimSP simulations (see section 3.3.2). These XPS measurements were complemented with a small number of ex situ measurements of the total N amount by nuclear reaction analysis 3.1.2. Sputter depth profiling of the created layers by argon erosion 4.1.2 was performed to compare the N depth profiles to the SDTrimSP simulations.

## Technical details

The XPS measurements presented in this work were performed in a commercial PHI ESCA 5600 device with OmniFocus III lens. The base pressure was in the $10^{-8}$ Pa range. All measurements except for one were done using monochromated Al $K_\alpha$ radiation with $\hbar\omega = 1486.6$ eV and an angle of 90° between the incoming monochromatic X-ray radiation and the hemispherical electron energy analyzer. The monochromated source was chosen because it provided a better count rate and suppresses the X-ray satellite peaks from two electron excitations in the Al target [77]. For the measurement shown in Fig. 4.7 a non-monochromatic Mg $K\alpha$ source was used with an angle between
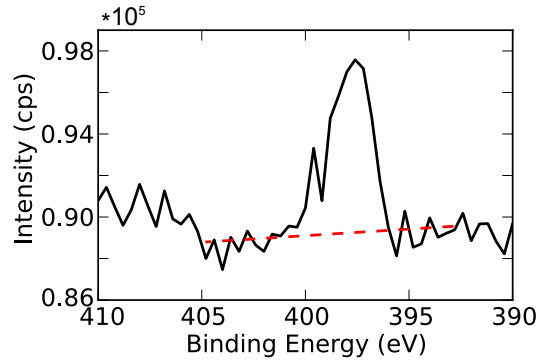


**Figure 3.6:** *N 1s peak after a N fluence of $7.8 \cdot 10^{19}$ N/m². The Shirley background (red dashed line) is a straight line because the background decreases towards higher binding energies.*

X-ray source and detector of 54.7°. The pass energy, which controls the range of electron energies accepted by the detector, was 93.9 eV for the presented measurements. This setting results in a rather low energy resolution of somewhat below 1 eV, but with the advantage of a good count rate and a detector transmission function which varies by less than 10 % over the considered energy range.

The integration time for the measurements has been chosen sufficiently large to make the statistical counting error negligible. This is reflected in the small scatter of the measurements and is demonstrated in detail for one XPS measurement: The cross section for photo electrons from the N 1*s* peak is about a factor of 5 smaller

---

dominated by the uppermost nanometers.

than for the W $4f$ peak. As a worst case one can consider the N $1s$ peak shown in Fig. 3.6, i.e. the first measurement of the 2.5 keV N implantation with a fluence of $7.8 \cdot 10^{19}$ N/m$^2$ resulting in a N $1s$/W $4f$ intensity ratio of 0.014, Fig. 4.1. The measurement is based on a survey spectrum where the energy range from 0 to 630 eV binding energy was measured for 190 seconds. The resulting peak consists of about 2000 counts. The peak-to-peak signal-to-noise ratio is about 4[c]. The intensity variation caused by varying the start and end points of the Shirley background is about 25 %. In most of the measurements both the integration time and N content were larger, further reducing the statistical counting error.

## Uncertainties

There are different sources for systematic errors in the experimental determination of the intensity ratios. The uncertainties introduced by sources like sample roughness, a dependence of the transmission function on the sample position, an uncertainty in the angle between X-ray source and electron detector of $\pm 1°$ and the presence of small amounts of oxygen[d] even for ultra-high vacuum conditions cannot fully be avoided or excluded. They are estimated by comparing different measurements with the same parameters on nominally identical samples: The variations observed in the W $4s$/W $4f$ ratios for 4 clean W samples and in the N $1s$/W $4f$ ratios after the 2.5 keV N implantations to steady state reported in this work, were about 15 %.

The surface structural state was checked by scanning electron microscopy for one sample after polishing and after 2.5 keV N implantation [93]. The bombardment by N induces a roughening on the originally smooth surfaces. For large fluences this roughening is visible by eye as surface discoloration. The scanning electron microscopy images show generation of structures with a lateral scale of the order of 10 nm. The amplitude of the structures could not be determined from these measurements.

The overlap of the N $1s$ peak with the W $4p$ peak presents another possible source of error for the intensity determination. The evaluation described in section 3.1.1 reduces this uncertainty to comparably low values. From the scatter visible in Fig. 3.5 the remaining uncertainty is estimated to 15 %. Considering uncertainties in the energy dependence of the detector transmission function and the observed variation in the W $4s$/W $4f$ intensity ratio, a total uncertainty of $\pm 30$ % for the experimental intensity ratios is used. The relative accuracy of the measurements

---

[c]As described in Ref. [94, p. 80], the signal is calculated as the difference between the highest intensity of the peak to the background intensity at about 380 eV, the noise as the difference between the highest intensity to the lowest intensity in a pure noise interval around 380 eV binding energy.

[d]Small amounts of oxygen, corresponding to $\leq 1\%$ when evaluated via relative sensitivity factors, could be detected during and after long XPS phases like complete surveys. The oxygen was quickly removed when the samples were bombarded with N.

should be much better, especially when considering a single (fluence dependent) implantation experiment, where for example the sample position is fixed.

## 3.1.2 Nuclear Reaction Analysis

To quantitatively determine the surface nitrogen content, nuclear reaction analysis (NRA) was performed on selected samples. The protons emerging from the nuclear reaction[e] $^{14}N\,(^4He,{}^1H)\,^{17}O$ were counted in a detector with a solid angle of 29.95 msr at a scattering angle of 135°.

For the analysis of the pure tungsten samples employed in the laboratory experiments, $^4He$ with an energy of 4.80 MeV was used. In this region the cross section is rather flat [96], so that small changes in the energy (the energy of $^4He$ ions is only known with an uncertainty of a few keV) of the $^4He$ do not change the cross section.

On the samples exposed in the divertor manipulator of AUG (see section 3.2), nuclear reactions with the carbon substrate caused an increased background in the region of the nitrogen peak. Therefore a resonance in the $^{14}N\,(^4He,{}^1H)\,^{17}O$ reaction at a $^4He$ energy of 4.94 MeV was used to increase the signal to noise ratio. A spectrum recorded in one of these measurements is shown as black line in Fig. 3.7, the nitrogen peak is located around channel 120.
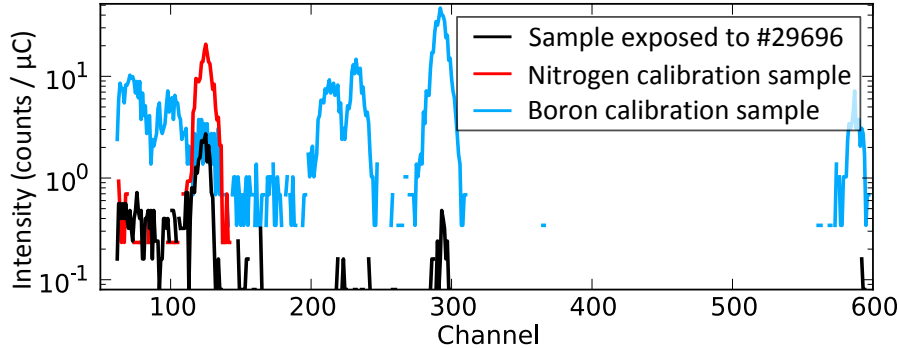


**Figure 3.7:** *NRA spectra from a sample exposed to AUG (#29696) in black, the nitrogen calibration sample (red) and the boron calibration sample (blue).*

The $^{14}N\,(^4He,{}^1H)\,^{17}O$ cross section has been determined for the experimental setup used in this work by measurements of a $C_xN$ layer, with a N areal density measured by Rutherford backscattering (RBS) [97]. According to this cross section a count rate of $1\frac{^1H}{\mu C}$ for 4.80 MeV $^4He^{1+}$ corresponds to an areal density of $1.6\cdot10^{19}\frac{^{14}N}{m^2}$. This cross section is 25 % lower for an energy of 4.80 MeV than the one published in Ref. [96]. A direct measurement of the N content in W with RBS is not possible,

---

[e]Actually this was the first identified nuclear reaction. It was detected by E. Rutherford in 1919 [95].

because small amounts of light elements in a heavy matrix like tungsten cannot be detected.

For a $^4$He energy of 4.94 MeV the cross section is peaked and varies significantly within the uncertainty of the primary energy of 0.01 MeV [96, 97]. A quantification based on reported cross sections is therefore error-prone. To omit the uncertainty of the primary energy in the quantification, a sample with a $C_xN$ layer with a known N areal density was measured at the same time. This allows to directly calculate the calibration factor relating the number of counts to the nitrogen areal density. Because the calibration sample and the analyzed samples are probed with the same energy, the uncertainty in the primary energy does not enter the evaluation. Figure 3.7 also shows a measurement from the $C_xN$ sample (red line).

Finally, a comparison of the spectrum from a boron coated sample (blue line in Fig. 3.7) with the spectrum from the sample exposed to AUG, shows that also boron was deposited on this sample during the exposition to the AUG plasma. The resulting boron areal density was calculated from a calibration based on the known areal density of the boron coated sample.[f]

The evaluation of the NRA measurements is based on the surface approximation: For the considered energies, the nitrogen implantation depth is below 10 nm. Therefore, the energy loss of the primary beam in the material is negligible so that the energy dependence of the cross section can neglected. The N areal density is then directly proportional to the number of proton counts for a given number of $^4$He projectiles. For the NRA measurements of N, all results are based on at least 100 counts, corresponding to a statistical error of $\leq$10 %. It should be kept in mind, that nitrogen is adsorbed on every surface which has been carried through air. The nitrogen areal density on a clean sample is about $10^{15}$ N/m$^2$.

### 3.1.3  Sample preparation

For the XPS ion implantation experiments this work employed hot rolled tungsten samples with a purity of 99.97 wt. % produced by PLANSEE, polished to a mirror-like surface finish and annealed in vacuum with a background pressure of about $2 \cdot 10^{-5}$ Pa at 1200 K for 2 hours.

The XPS device is equipped with sample heating and two SPECS IQE 12/38 ion sources for in situ ion implantation. A schematic drawing of the ion source is shown in Fig. 3.8. The sample temperature is controlled via a measurement located at

---

[f]It can be seen that also the boron calibration sample generates a peak around channel 120, the position of the nitrogen peak. However, this peak could be due to residual nitrogen in the boron sample. Anyways, it cannot corrupt the measurement of the nitrogen content because it has a lower cross section than the boron peak at channel 300, whose intensity is already much smaller than that of the nitrogen peak.
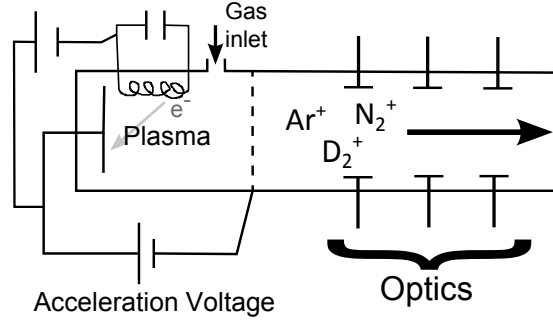
**Figure 3.8:** *This schematic drawing of an ion source, as installed in the XPS experiment, shows the ionization of the working gas by electron impact on the left, the acceleration via an applied voltage and the ion optics used to focus and steer the beam on the right. Between the acceleration stage and the beam optics a Wien mass filter can be installed.*

the sample holder. Though there is no direct contact to the sample, previous experiments indicate that the temperature control is reliable. One of the ion sources is equipped with a Wien mass filter and was used for mass separated implantation with 5 kV acceleration voltage. As the beam consisted of $N_2^+$, the resulting energy per atom was 2.5 keV. Due to technical problems implantation at 500 eV per atom was performed with the unfiltered ion source. Analysis of the mass-filtered beam showed that already the unfiltered beam consists of at least 99 % $N_2^+$, little $N^+$, and traces of impurities like argon or hydrogen. The deuterium bombardment was performed with $D_2^+$ from the mass-filtered ion source at an energy of 2.5 keV per deuterium atom. The N implantation to prepare the erosion by D was performed with the unfiltered source, so that the D bombardment could be done without delay after the N implantation. The angles of the mass-filtered and unfiltered ion sources to the sample surface normal are 45° and 40°, respectively.

To study the nitrogen accumulation and erosion due to ion bombardment also the fluence, i.e. the number of incident particles per area, must be measured. The number of ions reaching the samples was deduced from measurements of the sample current during the implantation. The sample current was measured with a bias of 50 V to suppress secondary electron loss. Measurements of the sample current with varying bias voltage and comparison to Faraday cup measurements confirm that 50 V are sufficient to get a valid ion current measurement. As this voltage is much smaller than the acceleration voltage for the ion implantation, it does not change the implantation conditions.

The mass-filtered ion beam has a Gaussian profile with a full-width-at-half-maximum of about 0.5 mm. The ion source without mass filter had a larger beam, with a full-width-at-half-maximum of about 1.5 mm. For the N implantation both beams were scanned over an area of 6 mm by 6 mm to ensure a homogeneous implantation. The XPS analysis area is circular with a diameter of 0.8 mm. The area used for the fluence calculation was $6.5 \cdot 6.5$ mm$^2$. The fluence was determined by dividing the

total current onto the sample by the beam spot size, as measured with a Faraday cup. The uncertainty in the fluence is estimated from the uncertainty in the area determination to $\pm 20$ %.

To reach the fluences for the D erosion measurements within reasonable time, the bombarded area was reduced to about 9 mm$^2$. With this smaller area the fluence is not entirely homogeneous over the bombarded area. Therefore, the D fluence was deduced from current measurements with a Faraday cup. Within the beam spot the fluence was locally up to 20 % lower than in the center. A comparison of the integral of the Faraday cup measurements over the beam spot with the measured total current onto the sample suggested that the fluence measured with the Faraday cup may be up to 30 % too low. Thus the estimated fluence uncertainty is $-20$ % to $+30$ %.

## 3.2 ASDEX Upgrade Experiment

### 3.2.1 ASDEX Upgrade Tokamak

ASDEX Upgrade (AUG) is a medium sized tokamak with a major radius of 1.65 m and a minor radius of 0.5 m [5, 46]. Typical operational parameters for AUG are a toroidal magnetic field of 2–3 Tesla, plasma currents of about 1 MA and a line averaged electron density of up to $10^{20}$ m$^{-3}$. There are two main operational scenarios, the L-mode and the H-mode with improved energy confinement. The H-mode is induced by a sufficiently high power input into the plasma. It was discovered in the *Axial Symmetric Divertor EXperiment* (ASDEX, the predecessor of AUG) more than 30 years ago [98]. The confinement in H-mode operation is, because of a transport barrier close to the separatrix, by a factor of about two better than in L-mode. Therefore, H-mode operation is is the desired operating scenario for a fusion reactor. However, in H-mode operation an instability called *edge localized mode* (ELM) arises (see Ref. [99]). ELMs complicate the interpretation of plasma-wall interaction experiments in H-mode.

AUG has, as already indicated by its name, a poloidal divertor configuration as described in section 2.2. A distinctive feature of AUG is its tungsten (W) first wall. Most of the other fusion experiments still use carbon as wall material, which is not suited for a fusion reactor [7]. An important consequence of the W wall is a strongly reduced carbon concentration in the plasma, which necessitates impurity puffing for radiative cooling as discussed in section 2.6. Nitrogen has been established by AUG as optimal choice for this purpose [9].

## 3.2.2 Plasma parameters

The plasma scenario chosen for the experiments presented in this work is a well diagnosed L-mode discharge, guided by the philosophy of a 'simple as possible plasma' [100]. The chosen discharge scenario is similar to the configurations studied in Refs. [101, 102]. The direct prototypes for the chosen discharge scenario are #27691 and #28818 with a plasma current of 1 MA, moderate electron cyclotron resonance heating of about 450 kW in the plasma center, a line averaged density of about $4 \cdot 10^{19}$ m$^{-3}$ and a magnetic configuration identical to #27100 described in Ref. [101]. An advantage of the chosen plasma scenario is the availability of good SOLPS plasma backgrounds (see section 3.3.5) [103, 104].
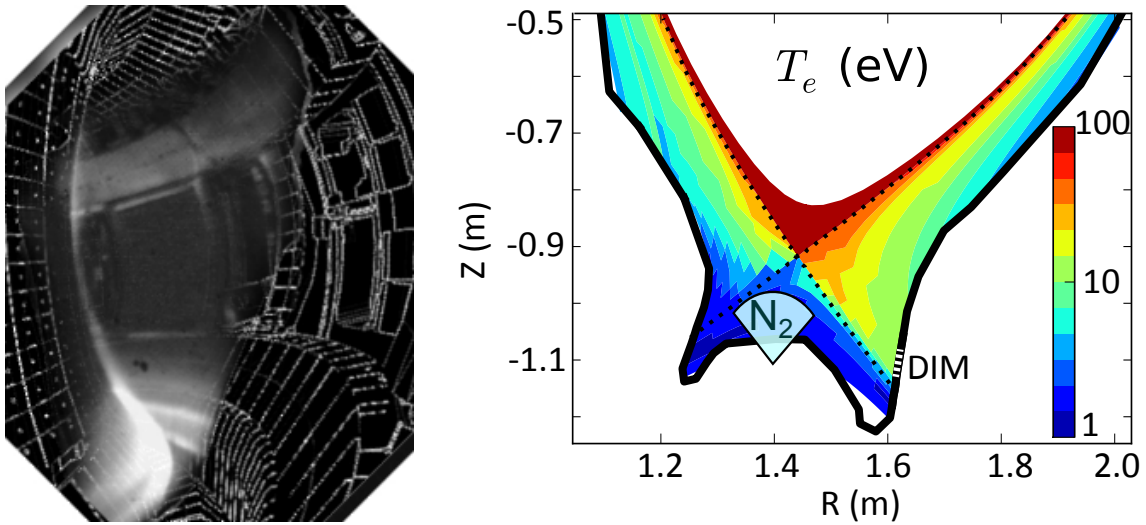


**Figure 3.9:** *The left picture shows a CAD drawing of AUG overlaid with a camera image from discharge #29736. The visible radiation is emitted from neutral deuterium, which is mainly present in the divertor. The right picture illustrates the setup of the presented discharges: The valve used for N$_2$ puffing is located below the magnetic X-point and the divertor manipulator (DIM, dashed region) is located above the low field side strike line. The contours indicate the electron temperatures from the SOLPS plasma background for the nitrogen seeded phase.*

The experiments presented in this work were performed on two different days in the discharges #29695 to #29698 and #29730 to #29732. The magnetic geometry and the electron temperature (from a SOLPS simulation, see section 3.3.5) in the divertor region is shown in Fig. 3.9b. This figure also shows the position of the AUG divertor manipulator (DIM) system (see section 3.2.3), which was used to measure the N accumulation on samples exposed to the divertor plasma. The samples were exposed to different combinations of N-seeded and non-seeded discharges:

- A sample was exposed to discharge #29695, which was a reference discharge without N$_2$ puff.

34

- Samples were exposed to a single N-seeded discharge in #29696 and on the second day for comparison in #29730.

- A sample was loaded with nitrogen in the N-seeded discharge #29697 and then exposed to #29698, which was without $N_2$ puff, to study the re-erosion of nitrogen.

- A sample was exposed to two subsequent N-seeded discharge #29731 and #29732 to study the fluence dependence of the nitrogen accumulation on the sample.

The applied $N_2$ puff should be well above the N background level but should be as low as possible to not disturb the plasma. An average N seeding rate of $2.9 \cdot 10^{20}$ N/s was chosen. This is a rather small puff in comparison to the value of $3 \cdot 10^{21}$ s$^{-1}$ suggested in Ref. [14] and the rates used for radiation control, which are above $10^{21}$ N/s [62, 61]. Valves with 8 toroidally distributed outlets in the roof baffle were chosen for the puff to maintain the toroidal symmetry of the tokamak geometry (Fig. 3.9b). This choice is also of practical relevance, as these valves are



**Figure 3.10:** *N puff (lower curve) and electron temperature close to the outer strike line during discharge #29696.*

regularly used for $N_2$ puffing at AUG. As a minimum flux is required to open the valve, the modulation of the puff visible in Fig. 3.10 (10 ms on, 30 ms off) was required. The valve is connected to the outlets in the roof baffle via a tube of 3 m length. The time required for the $N_2$ to move from the valve location through the tube to the outlet is above 0.1 s, so that the original modulation in the puff is smoothed out. The time dependence of the resulting $N_2$ puff is further discussed in section 5.2.1.
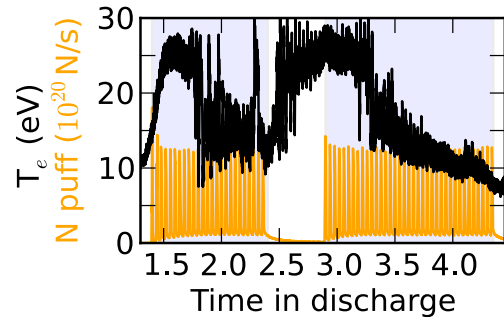
Because of the N history effect (see section 2.6) N-seeded discharges increase the N background in subsequent discharges. There were nine non-seeded discharges prior to #29695 and there were no N-seeded discharges between #29697 and #29730. According to N spectroscopy and residual gas analysis, the initial background N content (N concentration in the core plasma about 0.2 %) was a factor of 2–7 lower than the N content during the N seeded phase. The initial N background for #29695 and #29696 was a little bit higher than the initial N background in #29730.

The phase of the discharge in which the flattop plasma current and heating power were available started at 1.2 s and lasted for 3 s. The $N_2$ puff was switched on at 1.4 s. At 2.4 s the puff was switched off for 0.5 s. This break was introduced to observe the re-erosion of the previously implanted nitrogen. Unfortunately, as discussed in section 5.2.1, the turn-off time of the $N_2$ puff was too slow to draw

conclusions on the N re-erosion. The (modulated) $N_2$ puff and a measurement of the electron temperature at the lower side of the DIM are shown in Fig. 3.10. This temperature measurement is close to the strike line, the intersection of the separatrix with the divertor target plate, where the most intense interaction of the plasma with the walls takes place.

The electron temperature at this position was not constant over the flattop phase but drops to lower values when the $N_2$ puff is switched on. At the same time, the radiation emitted from the divertor plasma starts to fluctuate with a frequency of 4–5 kHz. These observations indicate that, despite the low N seeding rate, the puff induced a transition into the fluctuating detachment state described in Ref. [102]. During the non-seeded phase in the middle of the discharge the plasma nitrogen content drops and the divertor plasma changes back to its original (higher $T_e$) state. Due to the latency of nitrogen in AUG the background nitrogen level rose during our discharges and the low $T_e$ phases became longer. The transition between the high and low $T_e$ divertor plasma state is not instantaneous. Rather the the plasma starts to oscillate between these two states (at about 40 Hz, consistent with the oscillations observed in Ref. [102]) indicated by the spikes in the electron temperature in Fig. 3.10. Thereby, the mean value of the temperature and the amplitude decrease with increasing N content in the plasma. Also short activations of the neutral beam injection system, required for charge exchange spectroscopy measurements as explained in section 3.2.4, can bring the divertor plasma back into the high $T_e$ state (e.g. at t=2.3 s).

### 3.2.3   Divertor manipulator system

Laboratory experiments help to understand the basic processes in the plasma-wall interaction. Nevertheless, the special environment in a fusion reactor, like impact angles, energy spectra and composition of the incoming flux, cannot be fully reproduced under laboratory conditions. Therefore the knowledge gained from laboratory experiments must be verified in fusion experiments. As a good base pressure of about $10^{-5}$ Pa is required for plasma operation[g], most parts of the wall are only accessible between experimental campaigns.

To facilitate experiments where material samples shall be exposed to a limited number of discharges, AUG is equipped with a divertor manipulator (DIM) system. This system employs a load lock to allow exposition of samples to single discharges. After exposition the samples are retrieved for ex situ analysis. As shown in Fig. 3.9b (in section 3.2.2) the divertor manipulator system is located in the outer divertor and could host samples of 1 cm width (in toroidal direction) and 4.5 cm length (in poloidal direction). In the experiments presented in this work, samples with a 2 $\mu$m thick W layer on a fine grain graphite substrate were exposed to the plasma. The W layers were produced by combined magnetron sputtering and ion implantation

---

[g]After venting with air the AUG vacuum vessel is baked for several days at 150 °C [46, Ch. 2]
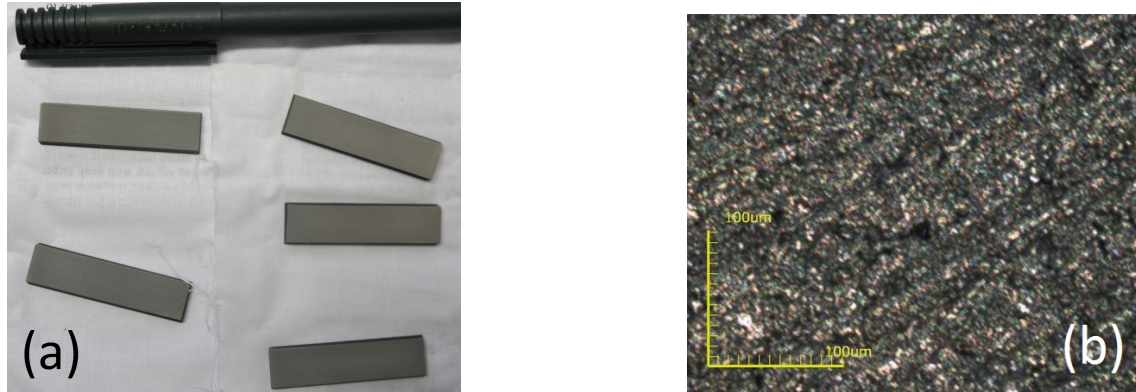
**Figure 3.11:** *Picture of the tungsten coated samples prior to their exposition in the AUG divertor manipulator (a). The microscope image after exposition (b) shows the roughness of the samples, caused by the graphite substrate.*

[105]. This is the same production process as used for coating the AUG tiles. The fine grain graphite substrates have a rough surface which carries over to the tungsten coated surfaces. A picture of the samples prior to exposition is shown in Fig. 3.11a and a microscope image of the rough surface in 3.11b. The increase of the effective surface area by the roughness was one of the proposed explanations for the discrepancy in the nitrogen saturation areal densities deduced from laboratory experiments and AUG measurements as discussed in section 2.6. This is discussed further in section 5.1.1.

After the exposure the samples were stored in a vacuum exsiccator with a dry vacuum environment at a pressure below 700 Pa. The main analysis was done by NRA as described in section 3.1.2. The results are presented in section 5.1. The samples were also analyzed by XPS measurements and optical microscopy, however, without conclusive results.

### 3.2.4 Spectroscopy and Fast Cameras

The light emitted from ions in the plasma is an indication for their distribution in the plasma. Unfortunately, similar to the case of XPS (see section 3.1.1), the interpretation of these measurements is not always straight-forward. This section gives a short introduction into spectroscopic measurements. More details on such measurements, their application and possible problems or pitfalls can be found for example in Refs. [5, 101, 106, 107].

Atoms and (not fully ionized) ions in a plasma can be excited by an electron impact. For the case of a fusion plasma, deexcitation mostly takes place by spontaneous emission of characteristic line radiation. Fusion plasmas are optically thin for impurity radiation so that the emitted radiation leaves the plasma without further interference [108]. While hydrogen is fully ionized already at an electron temperature of a

few eV [108], nitrogen becomes fully ionized only above 100 eV as can be seen from the ADAS data in Fig. 2.8. At lower temperatures it can emit line radiation. This radiation increases the power loss from the plasma and can be used for diagnostic purposes. The number of photons emitted per second is proportional to the density of the emitting ion state but depends on the local electron density and temperature, too.

The measurement of radiation via spectroscopy or cameras is routinely used for diagnostic purposes, but underlies some restrictions. A first problem is that such measurements always give line integrated information, which is difficult to interpret for inhomogeneous plasmas. Special techniques like charge-exchange spectroscopy, which is explained below, allow for a good localization of the measurement but are restricted to certain positions. A deconvolution of line integrated measurements is only possible assuming certain symmetries and requires a large number of lines of sight at suitable positions. The same problem, the interpretation of depth integrated measurements, already appeared in the XPS experiments 3.1.1 and was tackled by a forward calculation. With WallDYN-DIVIMP calculations of the impurity distribution in the plasma, the same approach can be used for plasma spectrometry (see section 3.3.3).

However, the challenges in the forward calculation are different between XPS and plasma spectroscopy. Emitted photons can cross the plasma essentially without further interaction as the plasma is optically thin. Therefore, the mean free path of photons is infinitely long. On the other hand, the generation process of the radiation from the plasma is rather complex. First one has to decide between the different ionization stages of one element. Furthermore the number of emitted photons depends on the local electron temperature and density, which may be subject to larger uncertainties. A simulation result showing the number of emitted photons per ion is shown in section 3.3.3. It shows that this number can vary over orders of magnitude within a few centimeters.

Also technical problems, like reflections from the metallic first wall and the harsh environment in a fusion reactor, complicate the quantitative evaluation of spectroscopic measurements. Because optical equipment in the visible range is much easier available than equipment for shorter wavelength, mostly the visible wavelength region is used for spectroscopic analysis. Unfortunately, not all ionization states of nitrogen are observable in this wavelength region.

The geometric lines of sight used for the passive divertor spectroscopy are shown in Fig. 3.12. Additionally, cameras with suitable filters were used. Cameras have the advantage of giving good spatial resolution. However, the filters may not remove the complete background radiation and cameras are less sensitive than spectrometers. Emission at the following wavelength was analyzed for the present work:

- The emission of neutral nitrogen atoms at 746.8 nm[h]. The calibration of the

---

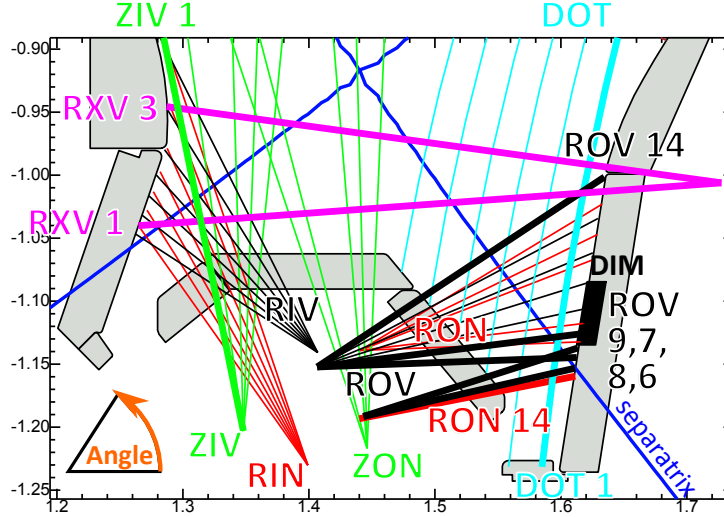[h]The ADAS data does not resolve the total angular momentum. The considered transition is

**Figure 3.12:** *The lines of sight used for the divertor spectroscopy in this work cover most of the divertor volume. From the thick drawn lines timetraces are shown in section 5. All lines of sight are compared in Fig. 5.12, where their angle with the horizontal, as indicated in the lower left, is used as x-axis.*

spectrometer for the low field side lines of sight (RON, ROV) was extrapolated to this wavelength and is therefore associated with some uncertainty. For the high field side lines of sight (RIN) no special calibration was available, so only an average calibration factor could be used.

- The emission of $N^{1+}$ at 399 nm, around 500 nm and at 568 nm.

- The emission of $N^{2+}$ around 410 nm.

- The $N^{7+}$ charge exchange line at 567 nm [109].

- The emission of neutral tungsten at 401 nm.

Emission from neutral atoms has the advantage of being very localized (because of the quick ionization) and is closely related to the influx into the plasma at the observed wall position. However, nitrogen ions may be directly created by dissociative ionization of $N_2^{z+}$. The region around 500 nm is dominated by strong nitrogen emission and therefore the most certain region to observe nitrogen. In return, more information is available with spectrometers observing the wavelengths around 400 nm (with 3 relevant peaks) or 746 nm (with neutral nitrogen). As also the nitrogen peaks in this region could easily be observed, future measurements should focus on

---

a triplet, where three final states with different total angular momentum exist. For a comparison to ADAS all three intensities must be added. Unfortunately, one of the transitions overlaps with another peak. For this reason only the most intense peak at 746.8 nm is used for the evaluation. The relative intensities of the peaks are 1:2:3, corresponding to the degeneracies of the final states. This allows to calculate the total intensity from the measurement of one peak.

these regions. Fast cameras with filters were used to observe the emission around 502 and 747 nm.

A more sophisticated spectroscopic technique is the charge exchange recombination spectroscopy (CXRS) [109]. For this technique the photons emitted after charge exchange collisions are measured. At AUG, CXRS observes the core plasma at the low field side midplane. At this position, charge exchange collisions almost exclusively take place with particles from the neutral beam injection. The neutral beam injection is originally one of the heating methods used in fusion plasmas [5]. It locally injects energetic neutral hydrogen and so the origin of the charge exchange emission can be precisely determined. A detailed analysis of CXRS measurements actually allows to deduce the concentration of (fully ionized) nitrogen in the core plasma [109]. The charge exchange spectroscopy employs different lines of sight to measure radial profiles of the concentration. However, the core nitrogen concentration in the studied discharges was homogeneous, so only radially averaged concentrations are given. As already indicated, the neutral beam injection must be activated for CXRS measurements. Because the applied heating power had to be kept below the H-mode threshold, such measurements are only available at particular times.

### 3.2.5 Residual Gas Analysis

Measurements with mass spectrometry allow to measure the local gas composition. Unfortunately, mass spectrometers can only be installed outside of the main magnetic field [110]. Still residual gas analysis allows to estimate the amount of nitrogen retained in the vacuum vessel and to study the conversion of puffed nitrogen molecules to ammonia.

Two mass spectrometers were installed at AUG at the time of the experiments presented in this work. As Fig. 3.13 shows, the mass spectrometer $HPQI$ was installed below the inner divertor and $HPQO$ was installed in the pumping duct on the low field side. Particles from the plasma must travel through the small slits between the divertor target plates and the roof baffle to reach the mass spectrometers and the pumping system.

The intensities measured with a mass spectrometer can be converted to partial pressures via a calibration. Unfortunately, no special calibration experiments as performed in Ref. [111] are available from the relevant experimental campaign. The calibration was therefore performed via capacitance manometers, installed next to the mass spectrometers, and detection efficiencies: Via the capacitance manometers a calibration factor could be determined for the dominating deuterium molecules, relating the intensity at $m/Z = 4$ (corresponding to $D_2^+$) to the deuterium partial pressure. The calibration factor for $N_2$ was then determined via the detection efficiencies given in Ref. [111].

The actual quantity of interest for this work is the number of pumped molecules
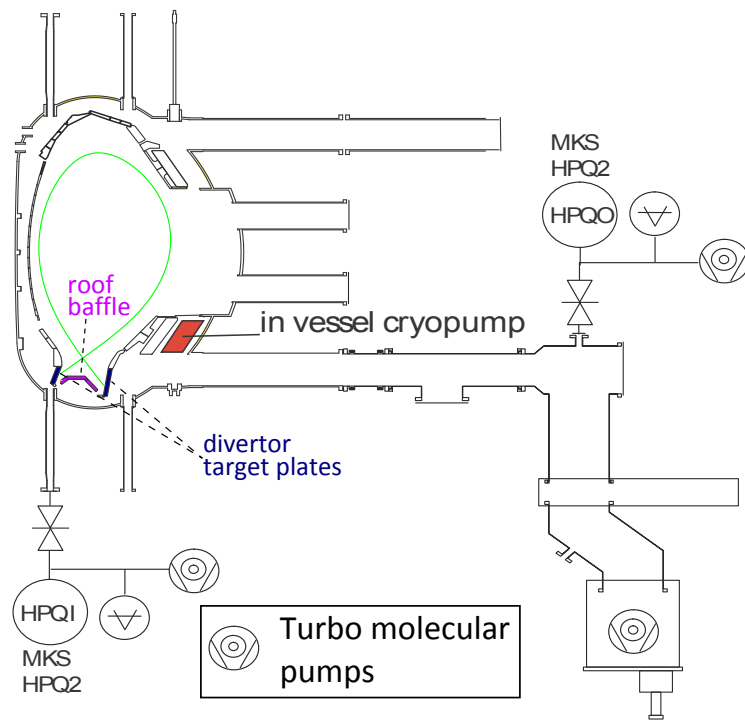
**Figure 3.13:** *The AUG vacuum pumping system comprises continuously operated turbo molecular pumps and a liquid helium cryopump, which is switched on for the experiments. The residual gas analysis is based on two mass spectrometers, HPQI and HPQO. The figure is based on Fig. 1 from Ref. [72].*

($\Sigma$). This number can be calculated from the partial pressure ($p_A$ $[\text{Pa}]$) of species $A$ and the pumping speed ($S$ $[\text{m}^3/\text{s}]$, from Ref. [112]) based on the formula [111]:

$$\Sigma = c \cdot \int_0^\infty p_A(t) \, S(t) \, \mathrm{d}t \tag{3.5}$$

with $c = \frac{1}{k_B\,T} \approx 2.5 \cdot 10^{20} \dfrac{\text{molecules}}{\text{Pa m}^3}$.

The main turbo molecular pumps are installed far away from the plasma (lower right in Fig. 3.13). Further auxiliary turbo molecular pumps are installed for the mass spectrometers and some further diagnostic or heating systems. When the in vessel liquid helium cryopump is in operation, its pumping speed is more than a factor of five larger than the pumping speed of the turbo pumps [112].

More details on the calibration, evaluation and uncertainties can be found in appendix B and Ref. [111].

## 3.3 Computer Models

### 3.3.1 SDTrimSP

SDTrimSP [28, 29] is a code to simulate the interaction of energetic particles with solids in the binary collision approximation (BCA), as described in section 2.3.2. BCA codes like SDTrimSP are routinely applied and in general give a good agreement to experimental measurements for sufficiently high energies [35].

SDTrimSP uses the Monte Carlo approach to simulate the transport of atoms in amorphous solids. Quantities like the path traveled between subsequent collisions and the impact parameter for the collisions are determined with a random number generator independently for each collision. It has been found that this approach also gives good results for polycrystalline samples [32, section 4.2].

For the calculation of the path lengths between subsequent collisions the local density $\rho(d)$ has to be known. For mixed materials this density is calculated by SDTrimSP assuming that the atomic volumes are independent of the composition. For the simulations presented in this work the atomic volume of nitrogen was adapted to match the density of tungsten nitride given in Ref. [69]. A more physical depth ($d$) scale than the length (e.g. in nm) is a depth specification in terms of the areal density:

$$d\,[\text{areal density}] = \int_0^{d_{nm}} \rho\,(d_{nm})\,\mathrm{d}d_{nm} \tag{3.6}$$

This depth scale is used in Figs. 4.10, 4.11 and 5.7.

SDTrimSP can be operated in a static or dynamic mode. In the static mode the target composition is fixed and values like sputter yield or implantation depth are calculated. This mode was used to calculate sputter and reflection yields for WallDYN (see section 3.3.3). In the dynamic mode each particle represents a certain fluence and modifies the depth dependent target composition by sputtering, implantation and recoil generation. This mode was used for the SDTrimSP simulations shown in sections 4.1, 4.2 and 5.1.

In general SDTrimSP is well tested. Still the applicability of SDTrimSP for individual systems has to be verified, especially when chemical effects become important. Therefore, SDTrimSP simulations can be optimized by adjusting available parameters from a comparison of simulations to experimental measurements. Two important parameters are the surface binding energy (SBE) and the maximum concentration of a given species. As already described in section 2.3, the SBE determines whether particles actually leave the sample when they reach the surface.

The chemical interaction between particles is not included in SDTrimSP. Therefore it would be possible in the simulation to form a target of pure nitrogen, while in reality nitrogen would start to effuse from the surface. This behavior can be imitated by setting a maximum concentration for nitrogen, limiting the nitrogen concentration in each depth layer to the given value (see Fig. 4.2). Still this is only a crude model because excess nitrogen is simply removed, while in reality it diffuses through the target. As more advanced simulations (e.g. molecular dynamics) are not available, the validity of this model can only be checked by comparison to experimental measurements.

A depth profile calculated by SDTrimSP for the implantation of N into W is shown in Fig. 3.14. The calculation was done with a N energy of 2.5 keV at 45° impact angle, no restriction on the maximum N concentration and a surface binding energy (SBE) for N which varied with the surface composition from 4.4 eV (pure W) to 3.5 eV (with N). An input file containing the parameters used for the simulations given in this work can be found in appendix A.

### 3.3.2   Forward calculation of XPS intensity ratios

XPS measurements (see section 3.1.1) are weighted averages over a depth of roughly three electron inelastic mean free paths. The weight function is an exponential, strongly emphasizing the contribution from the surface. Quantification of XPS results based on the simple application of relative sensitivity factors is naturally not possible for inhomogeneous materials. However, the conversion of a given depth profile (assuming lateral homogeneity) to XPS intensity ratios is possible by applying the formula (3.2). So it is actually possible to test whether a given depth profile is consistent with measured XPS intensities.

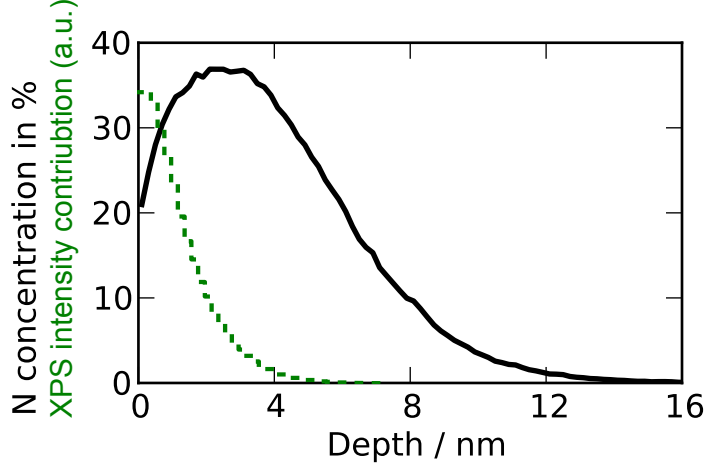The result of adopting equation (3.2) to the discrete output given by SDTrimSP is

**Figure 3.14:** *The black line is the N depth profile calculated for 2.5 keV N implantation. The green dashed line represents the contributions from different depths to the measured XPS intensity, i.e. the contributions to the sum in equation (3.8).*

illustrated in Fig. 3.15. In a first step the intensity emitted from every SDTrimSP depth layer is calculated. Since the composition is homogeneous within one SDTrimSP layer, the outgoing intensity in peak $A$ can be calculated for a layer $k$ analytically:

$$I_{A,k} = \xi_A \, \rho_{A,k} \, \lambda_k \left( 1 - \exp \left( \frac{-\Delta x_k}{\lambda_k} \right) \right) \tag{3.7}$$

In this expression $\xi_A$ contains all the prefactors from equation (3.2), $\rho_{A,k}$ is the number density of species $A$ in layer $k$, $\lambda_k$ the product of the electron inelastic mean free path in layer $k$ with $\cos \alpha$, the cosine of the angle between surface normal and detector, and $\Delta x_k$ the thickness of layer $k$. The fraction of the intensity from layer $k$ reaching the surface after passing through the layers 0 to $k-1$ is $\prod_{j=0}^{k-1} \exp \left( -\frac{\Delta x_j}{\lambda_j} \right)$. The contribution from different layers to the intensity at the surface, $I_{A,k} \cdot \exp \left( -\sum_{j=0}^{k-1} \frac{\Delta x_j}{\lambda_j} \right)$, is shown as green dashed line in Fig. 3.14 for a nitrogen implanted tungsten surface with the XPS parameters described in section 3.1.1. The total intensity is obtained by adding up the intensities from all layers:

$$I_A = \sum_k I_{A,k} \cdot \exp \left( -\sum_{j=0}^{k-1} \Delta x_j / \lambda_j \right) \tag{3.8}$$

The applied cross section data is taken from Scofield [113] and the electron inelastic mean free path is calculated with the G1 equation for inorganic compounds [114]. The angular dependence includes the elastic collision correction calculated with the formulas in Ref. [115] and employs the asymmetry parameters from Yeh [116].
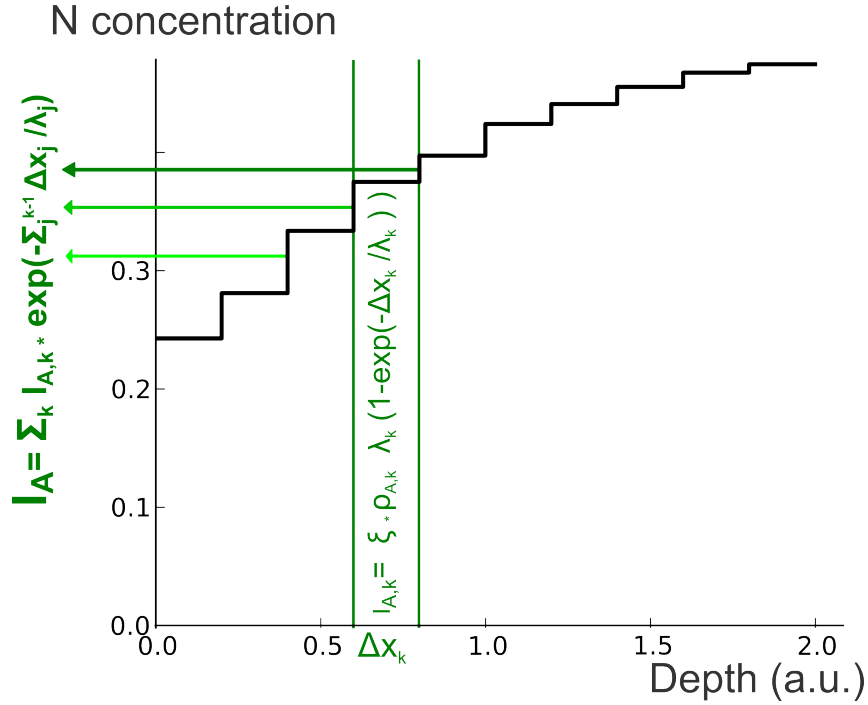
**Figure 3.15:** *For the calculation of the XPS intensities from the concentration depth profile (black line) the emission from each depth interval is calculated and then summed up.*

Due to the uncertainties in the input parameters, like the electron inelastic mean free path [114] and photoelectron cross section, also the result of the forward calculation is associated with an uncertainty. Unfortunately, the uncertainties in the input parameters are not quantified. For this reason a calculation of the uncertainty via error propagation, which is in principle possible with the forward calculation, was not performed. From published comparisons of theoretical calculations with measurements [117, 118] and a comparison of our own calculations with peak ratios of a pure W sample the error is estimated to $\pm 30$ %.

The forward calculation offers the possibility to interpret XPS measurements of ion implantation by a comparison to SDTrimSP simulations. Deviations between measurement and simulation in the initial phase of the implantation would indicate that the reflection process is not correctly described by the binary collision approximation. For large implantation fluences the steady state is set either by the re-erosion of the implanted species or by the chemical processes limiting the maximum concentration of the implanted species (see section 4.1.1). If SDTrimSP simulations agree with the experiment at all energies and fluences, it can be assumed that SDTrimSP describes the implantation and erosion processes correctly.

The application of the developed forward calculation is in no way limited to the problems presented in this work. For instance it has been applied for the interpretation of XPS sputter-depth profile measurements [119]. Sputter-depth profiling is widely used for XPS measurements with a depth resolution in the nanometer scale.

However, the common, direct interpretation of the measurement is difficult and questionable due to effects like preferential sputtering and ion beam mixing. These effects are naturally included in SDTrimSP simulations, so that the combination of SDTrimSP and the forward calculation can improve the reliability of sputter-depth profile interpretation. Finally, the forward calculation is a valuable tool in the planning of experiments, by indicating the experimental parameters which should give the most meaningful results.

### 3.3.3   WallDYN

**Basic WallDYN model**

The migration of impurities, as described in section 2.5, controls net erosion of the walls, impurity content of the plasma, formation of mixed materials and contributes to the retention of radioactive tritium in the walls. A generic model for impurity migration, including erosion, transport through the plasma and re-deposition, can only be handled in computer simulations. Migration is a multiscale problem and therefore most of the available models either simulate only the impurity transport in the plasma (assuming a fixed wall composition) or the evolution of the material surfaces on the microscopic scale (assuming constant impurity fluxes).

To this end the WallDYN code has been developed [15, 22]. It calculates the surface composition and impurity fluxes self consistently. The self-consistent coupling is attained by combining models for implantation, erosion and reflection of impurities with a model for the impurity transport through the plasma. WallDYN can either be used to predict erosion and migration in future fusion experiments like ITER and to support the interpretation of available experimental measurements. WallDYN is a novel tool in the simulation of impurity migration, so comparisons with experimental measurements are desirable for benchmarking.

The WallDYN model is illustrated in Fig. 3.16. For the numerical simulation the continuous wall configuration is discretized into wall tiles[i]. The size of the wall tiles in poloidal direction is chosen according to the expected gradients: Small tiles (with a poloidal extent in the cm range) are used in the divertor region and rather large tiles (up to 0.35 m for the simulations presented in this work) are employed on the main wall. Each wall tile consists of a thin reaction zone surface and an infinite bulk with a fixed composition. The composition of the reaction zone is modified by the incoming impurities and is used to calculate the erosion flux from this tile. The total areal density of the reaction zone, chosen to match a typical implantation depth of 4 nm, is kept constant by a flux of matter from or to the bulk.

---

[i] Currently this is done only in poloidal direction, assuming a toroidally symmetric wall. However, an extension to three dimensional geometries would be straight forward.
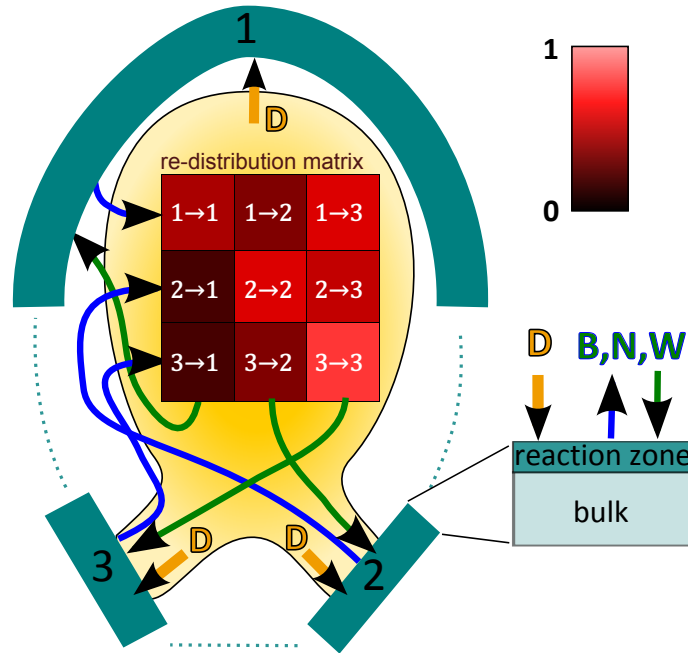
**Figure 3.16:** *For the WallDYN model the wall is discretized into wall tiles. Each wall tile consists of a bulk and a reaction zone. The composition of the bulk is fixed, the composition of the reaction zone evolves according to the incoming particle fluxes. The transport of the impurities through the plasma is parameterized by the re-distribution matrix calculated with DIVIMP. The re-distribution matrix states which percentage of the material eroded from a given tile impinges on another tile. Typically the matrix has strong diagonal terms. A re-distribution matrix for nitrogen in full resolution and the N fluxes calculated from this matrix are shown in Fig. E.1.*

The transport of the impurities from one wall tile to another is described by the so called re-distribution matrix. This matrix is a parametrization of DIVIMP simulations. DIVIMP is a code that simulates the transport of impurities through the edge plasma of tokamaks and is described in more detail in section 3.3.4. For a given source location the charge state resolved re-distribution matrix contains the fraction of particles which are transported to each of the wall tiles in a given charge state. An example for a simple, charge state integrated re-distribution matrix is contained in Fig. 3.16. A realistic charge state integrated re-distribution matrix is shown in Fig. E.1.

An important input for the DIVIMP-WallDYN simulations is the so called plasma background. This term denotes spatially resolved information about the (hydrogen) plasma parameters, like electron density $n_e$, ion densities, electron temperature $T_e$, ion temperature $T_i$ and the ion flow velocity. Firstly, the plasma background is required by DIVIMP to calculate the material transport. Secondly, the fluxes of the main species, usually deuterium, onto the wall are taken from the plasma background and the kinetic energy of the ions is calculated from the background via formula (2.2). Available models for the plasma background generation and more details on the backgrounds used in this work are discussed in section 3.3.5.

The impurity fluxes in the plasma are determined by the amount of material eroded from the surfaces. On the other hand, the impurity fluxes impinging on the walls modify the surface composition and contribute to the sputter erosion of the surfaces. Therefore the foundation of WallDYN is the generation and solution of a self-consistent system of equations for the impurity fluxes and the surface composition.

**WallDYN equations**

The system of algebraic differential equations [120] which self-consistently describes the surface evolution and the impurity fluxes from and to the wall tiles are:

$$
\begin{aligned}
\frac{\partial \sigma_{el,wk}}{\partial t} = \quad & \sum_{ql}^{Z_{el}^{max}} \left(1 - RY(\boldsymbol{\sigma}_{wk}, el, ql, wk)\right) \cdot \Gamma_{el,ql,wk}^{in} \\
& - \sum_{ej} \sum_{qj}^{Z_{ej}^{max}} C_{el,wk} \cdot SY(\boldsymbol{\sigma}_{wk}, el, ej, qj, wk) \cdot \Gamma_{ej,qj,wk}^{in} \\
& + \quad \Gamma_{el,wk}^{Bulk}
\end{aligned}
\tag{3.9}
$$

$$
\begin{aligned}
\Gamma_{el,q,wk}^{in} = \sum_{wj} RedMat_{el,q,wj,wk} \cdot \Bigg( & \sum_{ql}^{Z_{el}^{max}} RY(\boldsymbol{\sigma}_{wj}, el, ql, wj) \quad \cdot \Gamma_{el,ql,wj}^{in} \\
& + \sum_{ej} \sum_{qj}^{Z_{ej}^{max}} C_{el,wj} \cdot SY(\boldsymbol{\sigma}_{wj}, el, ej, qj, wj) \cdot \Gamma_{ej,qj,wj}^{in} \\
& + \quad \Gamma_{el,qj,wj}^{src} \Bigg)
\end{aligned}
\tag{3.10}
$$

The set of ordinary differential equations (3.9) describes the time evolution of the areal densities in the reaction zone. The set of equations (3.10) is purely algebraic and describes the impurity fluxes.

In these equations $\sigma_{el,wk}$ is the areal density of element $el$ in the reaction zone of wall tile $wk$ and $C_{el,wk}$ its concentration. $qj$ and $ql$ are the indices for the sums over the charge states and $Z_{el}^{max}$ the maximum charge state of element $el$. Ions with very high charge states only occur in the core plasma and partly recombine before reaching a surface. Therefore, the contribution of very high charge states to deposition and erosion can be neglected and the set of equations is reduced by limiting the maximum charge state of heavy elements like tungsten. For the

presented calculations the tungsten charge state was limited to $Z = 17$. $RY$ and $SY$ are the reflection and sputter yield, respectively (see below). $\sum_{ej}$ is a sum over all incoming species (including the hydrogen flux taken from the plasma background) which contribute to the erosion of the wall. $\Gamma^{Bulk}$ is used to keep the total areal density in the reaction zone constant and described below.

$\Gamma^{in}_{el,ql,wk}$ is the impurity flux of species $el$ impinging on wall element $wk$ with charge state $ql$. These fluxes and the areal densities $\sigma_{el,wk}$ are the unknowns in this system of algebraic differential equations. $RedMat_{el,q,wj,wk}$ is the charge state resolved redistribution matrix and contains the fraction of element $el$ emitted from wall tile $wj$ ending up on wall tile $wk$ with charge state $q$. A charge state integrated redistribution matrix is shown in Fig. E.1. $\Gamma^{src}_{el,qj,wj}$ represents additional fluxes into the plasma, like impurity puffing.

The plasma wall interaction enters the model through the sputter and reflection yields (see also section 2.3.3). Both quantities are calculated in WallDYN from fits to static SDTrimSP simulations [15]. The sputter yield of species $el$ by species $ej$ with charge state $q$ on wall tile $wk$ is calculated from the Bohdansky formula (2.3), which describes the energy ($E$) dependence of the sputtering, and a term which accounts for a composition ($\boldsymbol{\sigma}_{wk}$) dependence of the sputter yield:

$$SY(\boldsymbol{\sigma}_{wk}, el, ej, q, wk) = Y^{Bohd}_{ei,ej}(E_{q,wk}) \cdot \left( 1 + \sum_{ek}^{N} a_{ek}\ \sigma_{ek,wk} \right) \qquad (3.11)$$

The reflection yield of species $el$ with charge state $q$ on wall tile $wk$ is calculated with the formula:

$$RY(\boldsymbol{\sigma}_{wk}, el, q, wk) = R_{el}(E_{qj,wk}) = \rho\ E^{\alpha}_{q,wk} \cdot \left( 1 + \sum_{ek}^{N} b_{ek}\ \sigma_{ek,wk} \right) \qquad (3.12)$$

The parameters $a_{ek}$, $\rho$, $\alpha$, $b_{ek}$, $E_{th}$ and $Q_0$ (the last two come from the Bohdansky formula (2.3)), are obtained from fits to a large number of static SDTrimSP simulations with varying sample composition and varying incident energy. Sputter and reflection yields for N from the underlying SDTrimSP simulation versus the yields calculated with equations (3.11) and (3.12) are shown in Fig. 3.17a and 3.17b, respectively. The sputter yield from the model is in good agreement with the sputter yield calculated by SDTrimSP (the points are close to the diagonal line). The model for the reflection yield results in somewhat larger deviations, still the model matches the SDTrimSP results mostly within a factor of two. Further comparisons of the WallDYN surface model with SDTrimSP simulations will be given in sections 4.2.3 and 5.1.5.

In WallDYN the kinetic energies of the ions are calculated according to equation (2.2) by $E_{q,wk} = 3\ q\ T^{e}_{wk} + 2\ T^{i}_{wk}$. The required electron and ion temperatures are
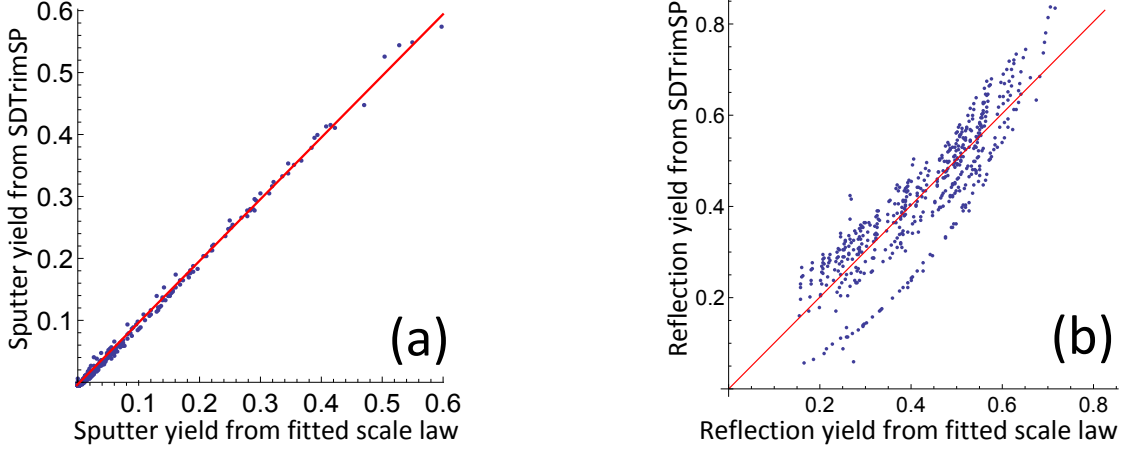
**Figure 3.17:** *Comparison of the sputter (a) and reflection (b) yield from SDTrimSP (y-axes) to the fit (x-axes) of the SDTrimSP results by equations (3.11) and (3.12), respectively. The individual points correspond to different incident energies (which causes most of the variation) and sample compositions. For a perfect fit all data points would lie on the (red) diagonal line. The energy dependence of some sputter yields is shown in Fig. 2.6.*

taken from the plasma background. The reflection yield of nitrogen is modified to reproduce the saturation of the nitrogen content. This model is described in section 3.3.3.

A special term in the equation for the areal densities (3.9) is $\Gamma^{Bulk}$. This term has been introduced to keep the thickness of the reaction zone constant:

$$
\begin{aligned}
\Gamma_{el,wk}^{Bulk} = - \quad & H(\Delta_{wk}) \quad C_{el,wk}\, \Delta_{wk} \\
& - (1 - H(\Delta_{wk})) \quad C_{el,wk}^{bulk}\, \Delta_{wk}
\end{aligned}
\tag{3.13}
$$

with

$$
\begin{aligned}
\Delta_{wk} &= \sum_{el} \Gamma_{el,wk}^{in} - \Gamma_{el,wk}^{reflected} - \Gamma_{el,wk}^{eroded} \\
&= \sum_{el} \left[ \sum_{qj} (1 - RY(el,qj,wk))\Gamma_{el,qj,wk}^{in} - \sum_{ek} \sum_{qj} SY(el,ek,qj,wk)\Gamma_{ek,qj,wk}^{in} \right]
\end{aligned}
\tag{3.14}
$$

The sign of $\Delta$ depends on whether there is net erosion or deposition, i.e. whether the total areal density increases or decreases. For net deposition the Heaviside step function $H(x)$ is 1 ($\Delta > 0$) and a composition ($C_{el,wk}$) dependent flux from the reaction zone compensates for the net influx from the plasma. For $\Delta < 0$ (net

erosion) the step function is zero and the reaction zone is filled up from the bulk (which has the fixed composition $C_{el,wk}^{bulk}$).

The equations (3.9) – (3.14) constitute a complete system of algebraic differential equations and are solved by the IDA solver [121, 122] for algebraic differential equations in Mathematica [123]. For a typical WallDYN setup with 3 impurity species (e.g. elements W, N, B) and 50 wall tiles, the system contains 150 differential and about 1500 algebraic equations. To improve the numerical stability the internal units of WallDYN are chosen to give numbers of the order of one. For example the unit of the fluxes is atoms/Å$^2$/s.

To calculate the re-distribution matrix, a DIVIMP (section 3.3.4) calculation has to be performed for each wall tile and particle species. DIVIMP calculates the transport of impurities through the plasma with a Monte Carlo approach. That means in a DIVIMP calculation a number of numerical particles ($N_{wk}^{el}$) of species $el$ is launched from the wall tile $wk$ and the number of particles impinging on wall tile $wj$ with charge state $qj$ is recorded ($N_{wj}^{el,qj}$). As WallDYN actually calculates the impurity flux densities (number of particles per time and area) the size of the original and final wall tile has to be taken into account and the redistribution of the fluxes can be calculated:

$$RedMat_{el,qj,wk,wj} = \frac{N_{wj}^{el,qj}}{N_{wk}^{el}} \cdot \frac{l_{wk}}{l_{wj}} \tag{3.15}$$

For the calculation of the matrices in this work, $N_{wk}^{el} = 50000$ particles were launched per species and wall tile.

**Model extensions for nitrogen**

A comprehensive description of the implantation and loss processes at the wall is essential to simulate the evolution of the surface composition and the resulting impurity fluxes. The original model implemented in WallDYN is suited for elements whose accumulation on the surface is not limited by effusion. In the course of this work WallDYN was extended to provide a model for saturating species. Also the pumping of nitrogen by the vacuum system and the time dependent boundary conditions resulting from the time dependent N-seeding (see section 3.2.2) had to be included in WallDYN.

Because WallDYN does not include the actual depth profile, only a simplified model for the saturation can be used. Based on the discussion given in sections 4.2.1 and 4.2.3, the model should limit the nitrogen areal density to $\sigma_N \leq 1 \cdot 10^{20}$ N/m$^2$. For a model to be suited for WallDYN, its physical adequateness is not sufficient. The compatibility to the original WallDYN model and numerical efficiency and stability must be considered, too.

These demands could be achieved by introducing an effective reflection yield with a proper concentration dependence. In this model the reflection yield is interpolated between the kinetic reflection yield ($RY^{kinetic}$) at low concentrations, and an effective reflection yield of one at the chosen maximum concentration:

$$RY^{effective} = I(C) + (1 - I(C)) \cdot RY^{kinetic}(\boldsymbol{\sigma}_{wk}, el, ql, wk) \qquad (3.16)$$

In this expression $C$ is the concentration of the saturating species and $RY^{kinetic}$ the reflection yield according to equation (3.12). $I(C)$ is a function with $I(C) = 0$ at small concentrations of the saturating species ($C < c_0$). Between $C = c_0$ and $C = c_{max}$ the value of $I(C)$ must increase from zero to one. This specifies the interpolation conditions ($I(C = c_0) = 0$ and $I(C = c_{max}) = 1$). The additional demand of a continuous first derivative at $C = c_0$ ($I'(C = c_0) = 0$) improves the numerical properties of the function and suggests to use a second order polynomial:

$$I(C) = \begin{cases} 0 & C \leq c_0 \\ \left( \dfrac{c_0 - C}{c_0 - c_{max}} \right)^2 & C > c_0 \end{cases} \qquad (3.17)$$

For $C > c_{max}$, $I(C)$ becomes larger than one. Under these conditions excess material is outgassed and the concentration still approaches $c_{max}$. This property is desirable because numerical effects or a time dependent $c_{max}$ could lead to situations with $C > c_{max}$. $c_0$ is set to $c_{max}/2$. This makes the transition from the kinetic reflection yield to a value of one rather smooth. Physically the smoothness reflects the fact that the considered reaction zone averages over a finite wall element and over depth. So part of the considered reaction zone volume will already be in saturation (and loose N via effusion) when the average concentration is still below $c_{max}$.

According to the laboratory experiments presented in section 4.1, the maximum concentration of N in tungsten is 50 %. However, this value should not be directly used as $c_{max}$ in WallDYN. The concentration of 50 % is only reached in a certain depth interval, while the average N concentration in the uppermost nanometers is smaller. With the default value for the reaction zone thickness of 4 nm[j] and a maximum concentration of 30 % the nitrogen saturation sets in somewhat below $1 \cdot 10^{20}$ N/m$^2$. This is the value suggested for the saturation areal density by laboratory experiments and SDTrimSP simulations in sections 4.1.1 and 4.2. One should note that the N areal density in WallDYN is usually increased above the reaction zone inventory by the bulk flux according to equation (3.13).

An effect which still may increase the N areal density over the value corresponding to a saturated reaction zone, is the so called co-deposition. This mechanism is important when significant amounts of eroded wall material are re-deposited at

---

[j]Corresponding to an initial tungsten areal density of $2.4 \cdot 10^{20}$ W/m$^2$

the considered position. Implantation depth and concentration of nitrogen still are limited, but as the surface continuously is covered with 'fresh' material, the area can collect more and more of the saturating species[k]. Co-deposition is known to be important for tritium retention with carbon walls [7] and should have the same effect on nitrogen retention. It is included in the WallDYN model through the bulk flux: When there is a boron or tungsten influx into a previously saturated reaction zone, part of the N is transferred from the reaction zone to the bulk and additional N may be deposited in the reaction zone. As discussed in section 3.3.3, the model becomes flawed when a wall tile switches from net deposition conditions to net erosion conditions.

Due to regular boronizations [124, 125], parts of the AUG first wall are covered with boron. The initial wall composition in the WallDYN simulations was pure tungsten around the outer strike line (black region in Fig. 3.18) and a mix of 80 % tungsten and 20 % boron for the rest of the wall (gray regions in Fig. 3.18). Boron, similar to tungsten, forms the stable compound BN with nitrogen. Furthermore, the formation of BN can be described in the binary collision approximation, neglecting chemical effects such as thermal diffusion [126]. The WallDYN model for the saturation of N is therefore applied for boron containing regions of the wall, too.

An essential loss mechanism for gaseous species like $N_2$ is the pumping by the vacuum system. An introduction to the AUG vacuum system is given in section 3.2.5. Including the neutral particle transport from the divertor slits (shown in Fig. 3.13) to the pumps would require computer simulations on a kinetic level. As a first approximation the wall areas corresponding to the divertor slits are regarded as pumps. This can be achieved in the WallDYN model by setting the sputter- and reflection yields of the corresponding tiles to zero. This model should rather overestimate the pumping because the backflow of gas from the pumping ducts to the main chamber and sticking of gas to the pumping duct surface is neglected. Also the slit geometry is not reproduced by the simulation in full detail and the inner divertor slit is somewhat larger than in reality. The pumping tiles are shown in Fig. 3.18 as green areas.

Usually WallDYN has been used to simulate the long term evolution of the surface composition for one set of boundary conditions. In the experiments carried out in the course of this work the nitrogen puff was suspended in the mid of each discharge for 0.5 s (see section 3.2.2). Two approaches were used to include the resulting time dependent boundary conditions in the simulations: In the first approach one re-distribution matrix, either more appropriate for the high or the low $T_e$ phase (see section 3.2.2), was chosen and the N puff source and the particle energy at the outer strike line were varied in agreement with the experimental conditions by time dependent boundary conditions. In the second, more refined approach, each phase was simulated by a single WallDYN setup and the SOLPS plasma background corresponding better to the plasma state in this phase was chosen. The main difference

---

[k]This is analogous to sublimation pumps, where materials like titanium are evaporated from time to time to continuously catch reactive gases like oxygen from the vacuum on the surfaces.
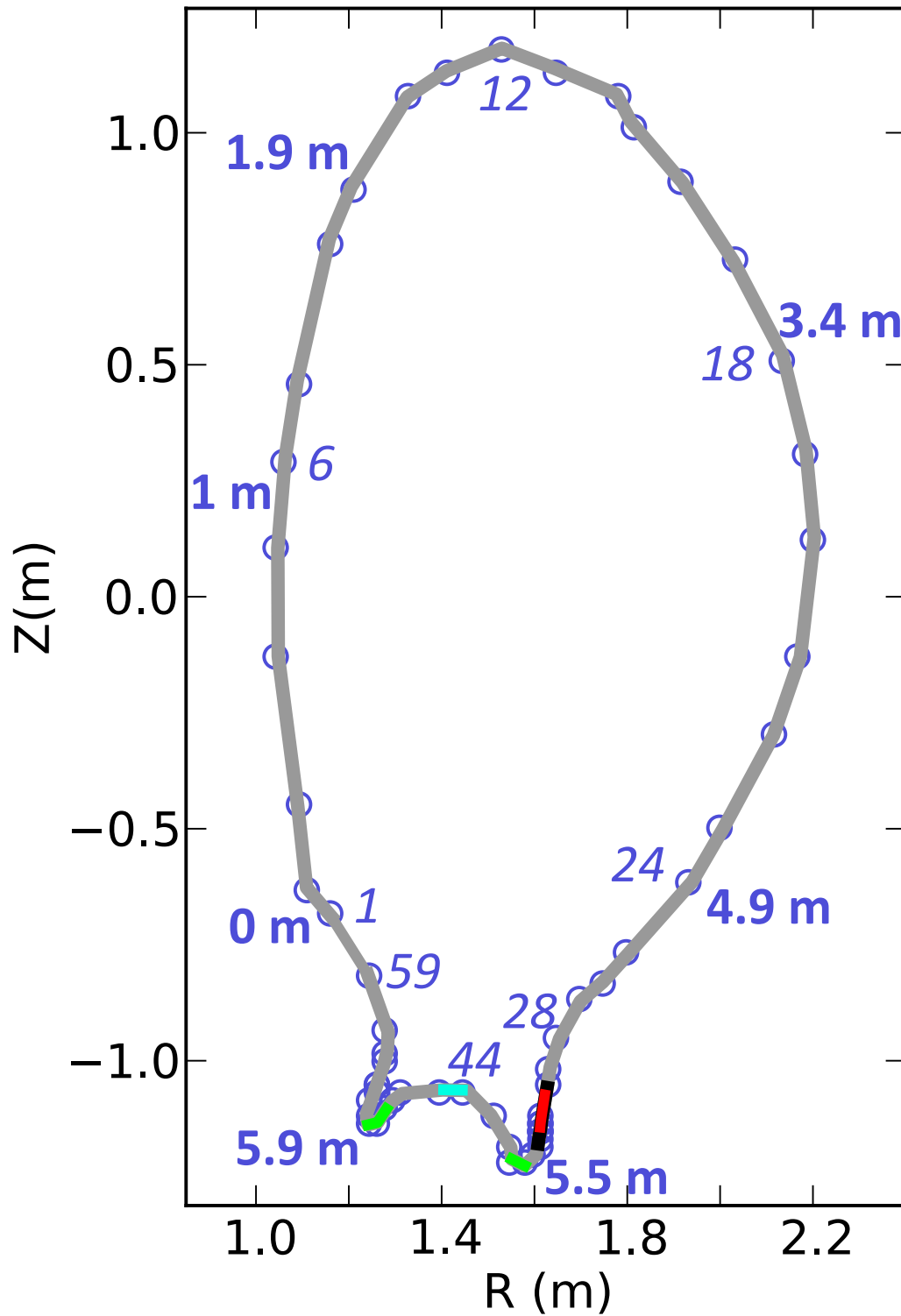
**Figure 3.18:** *Wall setup in WallDYN. The gray lines indicate walls with 20% boron, the black line a pure W wall. The green line shows the pumping tiles, the cyan line the source of the N puff and the red line indicates the position of the divertor manipulator. The circles indicate the wall discretization. The numbers on the inside give the index of the wall tile at this position, the numbers on the outside indicate the distance along the wall from the first tile. A zoom of the divertor area is shown in Fig. 3.9b.*

to the first approach was that also the re-distribution matrix was chosen according to the current divertor plasma regime (low/high $T_e$). The plasma backgrounds and this approach are further discussed in section 3.3.5.

## Limitations of the WallDYN code

WallDYN attempts to summarize all processes which are relevant for the evolution of the plasma facing surfaces. Nevertheless, such simulations can only be performed with some approximations. First, the simplifications and potential uncertainties arising from the WallDYN model for the plasma-wall interaction shall be discussed:

- WallDYN assumes a toroidally symmetric wall. This approximation is not fully fulfilled, especially for the low field side main wall (to the right in Fig. 3.9), where diagnostic and heating systems are installed. Also details like gaps between tiles or shadowed areas are not present in the simulations. Furthermore, WallDYN assumes an infinite ratio of major to minor radius (aspect ratio), i.e. a straight tokamak instead of an actual torus. This means that in WallDYN the surface area on the high magnetic field side is as large as on the low magnetic field side, although in reality this is not the case because of the different radii.

- WallDYN does not calculate the elemental depth distribution but only calculates an average reaction zone composition. To keep the thickness of the reaction zone constant, a bulk flux was introduced in the set of equations 3.9. This becomes problematic, when a wall tile undergoes a transition from net deposition to net erosion conditions. In this case WallDYN cannot reverse the bulk flux[1] but replenishes the reaction zone according to the fixed bulk composition. That means material transported during the net deposition phase to the bulk zone cannot be re-eroded (see also section 5.1.4). As discussed in sections 4.2.3 and 5.1.5 the calculation of the erosion flux from a surface averaged concentration is also a possible source for errors. An improved surface model is under development [127]. The new model simulates the full depth profile based on a convection-diffusion equation. However, effects like ion beam mixing and recoil implantation are not yet included in this model.

- The reflection and and sputter yields are originally determined for smooth surfaces and may be higher or lower for rough, technical surfaces. Also the angle of the incoming ions and their energy distribution are only known approximately.

- The re-distribution matrix is calculated for fixed initial energy distribution of the atoms and for a cosine angular distribution of the initial velocity direction

---

[1]However, it is possible to calculate the areal density deposited in the bulk during post processing.

(see section 3.3.4). In reality, the angular and energy distribution depend on the surface morphology and the generation mechanism of the atoms (gas puff, evaporation, reflection, sputtering). An additional complication for nitrogen is its occurrence in molecular form. This topic is further discussed in section 3.3.4.

- There is a strong dependence on the plasma background. This is mainly caused by the dependence of the re-distribution matrix (i.e. the transport of material through the plasma) on the plasma background.

- The time evolution of the plasma can only be included approximately, especially effects during ramp-up or ramp-down of the plasma are neglected.

- Additional physical effects which are currently not implemented (like arcing, chemical reactions or deposition of dust particles) can play a role.

Another uncertainty in the WallDYN simulations is the initial surface composition. It is only known for freshly installed surfaces. For AUG the original W surface is partly covered with boron and carbon layers [128, 129]. Measurements of the surface composition are associated with a large effort and only performed every few years. It is also not possible to simulate the initial wall configuration with WallDYN, as the variety of performed plasma discharges is too large and the wall conditioning by boronizations cannot be included.

Also the transport of the impurities is treated with some approximations in Wall-DYN (additionally to the approximations made in DIVIMP, see section 3.3.4). Firstly, the charge state of heavy elements like tungsten is limited to reduce the number of equations. However, with the chosen maximum charge state ($Z \leq 17$) less than one percent of the tungsten flux are affected by the cutoff. Secondly, the impurity fluxes are calculated from algebraic equations, assuming that the wall composition only changes little during the time between erosion and re-deposition. That means the transport time of the ions is neglected. Most of the ions are only transported through the SOL plasma and re-deposited within a few milliseconds. Including the transport time by using delay differential equations is not possible with the currently used Mathematica implementation. A possible approximation would be to describe the delay by an exponential function. Under this condition the delay differential equation can be rewritten as ordinary differential equation as described in Ref. [130].

Summing up one has to conclude that a large number of approximations enters the WallDYN simulations. Their impact depends on the considered problem and has to be assessed for the concrete situation. To obtain confidence in the simulations, but also to learn about possible pitfalls, the code must compared to experimental measurements to assess its validity.

When one of the WallDYN approximations is found to be invalid it may still be possible to combine WallDYN results with more specialized codes (like SDTrimSP

or ERO [131]). For example when depth profile effects are expected to become important the fluxes from WallDYN can be used for SDTrimSP simulations as shown in section 5.1.5.

## Synthetic spectroscopy

As described in section 3.2.4, the interpretation of spectroscopic measurements from fusion plasmas is difficult. However, with a given plasma background, charge resolved impurity distribution and known atomic data the resulting spectroscopic measurements can be calculated with a virtual diagnostic. For this work I implemented a virtual diagnostic based on the following expression for the photon emission:

$$\epsilon_{i\to j}^z = PEC_{i\to j}^{exc}(T_e, n_e)\, n_e n_i^{z+} + PEC_{i\to j}^{rec}(T_e, n_e)\, n_e n_i^{(z+1)+} \qquad (3.18)$$

In this formula $\epsilon_{i\to j}^z$ is the number of photons emitted from an ion with charge state $z$ in the transition $i \to j$. This number is calculated by multiplying the *Photon Emissivity Coefficients* ($PEC$) with the electron density and the density of the feeding charge state. Mostly the emission is from ions excited from the ground state of charge state $z$ ($PEC_{i\to j}^{exc}$) by electron impact. However, excited ions with charge state $z$ can also be produced by recombination of an ion with charge state $z + 1$ to charge state $z$ ($PEC_{i\to j}^{rec}$). The PECs depend on the local electron density and electron temperature and are provided for a broad range of ions by the Atomic Data and Analysis Structure (ADAS) project [50].

The number of 399.5 nm photons emitted per volume and time and per $N^+$ is shown in Fig. 3.19. This calculation is based on the SOLPS plasma background (see section 3.3.5) corresponding to the nitrogen seeded low $T_e$ plasma and ADAS data [50].

The ion densities, required for the evaluation of equation (3.18), can be directly computed from the DIVIMP output generated during the calculation of the redistribution matrix: From the DIVIMP calculations the impurity density in the plasma for unit outflux from a given tile is known. In WallDYN the outflux from each wall tile is calculated. In the employed trace approximation the impurity density can then be calculated as the sum of the contributions from the individual wall tiles.
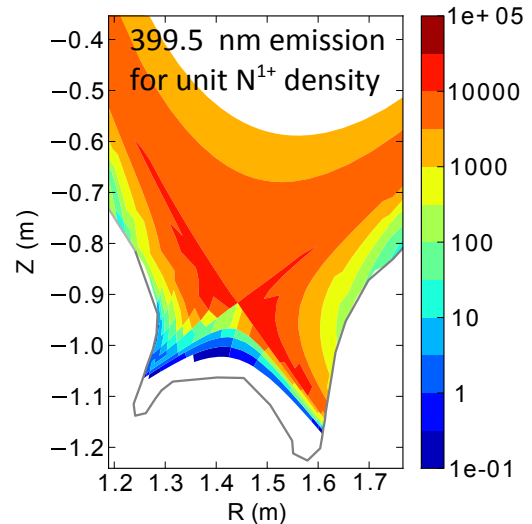


**Figure 3.19:** *Calculated photon emission for $1\frac{N^{1+}}{cm^3}$ per $cm^3$ and second (i.e. product of ADAS PEC and electron density) for the divertor region.*

The number of photons emitted per volume
can be calculated from the photon emission
per ion and the ion density. This quantity is shown in Fig. 5.13a for the emission
from neutral nitrogen. The photons can cross the, optically thin, plasma without
further interaction. The number of photons detected by the spectrometers can
therefore be calculated by a line integral over the number of photons emitted per
volume along the lines of sight. A comparison of simulated spectroscopic intensities
to measurements is presented in section 5.2.

### 3.3.4   DIVIMP

DIVIMP (short for **DIV**ertor **IMP**urity) [132] is a plasma physics modelling code
which simulates the transport of impurities in a fusion experiment with divertor
configuration. It is based on the LIM code (**L**imiter **IM**purity) [133] for limited
plasmas (a magnetic configuration without divertor). The code is based on a Monte
Carlo approach and includes ionization and recombination processes and the motion
due to the forces described in section 2.5.

There are several codes available which can calculate the impurity transport. A
major advantage of DIVIMP (e.g. over SOLPS with a more complete physics model)
is the short time it takes for a calculation. This is important for WallDYN, where
a large number of simulations is required for the re-distribution matrix (like the
one presented in Fig. E.1). Usually several WallDYN simulations with different
re-distribution matrices are performed for one problem, to test the influence of
parameters like the diffusion coefficient and plasma background. The number of
Monte Carlo particles launched (50000 per calculation) was chosen sufficiently large
to make the resulting error in the WallDYN simulations negligible.

The DIVIMP simulations employ a number of approximations for the calculation of
the impurity transport. The most important of them are listed in the following:

- DIVIMP employs the trace approximation to calculate the impurity trans-
  port. That means electron density, temperature and ion flows are taken from
  a plasma background (see section 3.3.5) and do not depend on the impurity
  distribution. Because the plasma background determines ionization, recombi-
  nation and the forces acting on the ions parallel to the magnetic field, DIVIMP
  simulations are very sensitive to it. When the plasma conditions change dur-
  ing the experiment, e.g. because of an increasing impurity content, DIVIMP
  simulations with various plasma backgrounds have to be performed.

- The impurities are launched as atoms with a cosine angular distribution [26,
  Ch. 9.3] and an energy of about 3 eV. This energy is in the range of half the
  surface binding energy, where the energy distribution of sputtered particles has
  its maximum [30]. However, nitrogen may enter the plasma in the form of ther-
  mal $N_2$ or even $NH_3$ molecules and the dissociation chains of these molecules

cannot be calculated with DIVIMP. The most likely effect of molecules would be to change the spatial ionization pattern. To test the sensitivity of the ionization pattern to the initial conditions of the particles, a WallDYN-DIVIMP simulation with an initial energy of the nitrogen atoms of around 0.03 eV was performed. The resulting deposition in the outer divertor was the same as for 3 eV. The impact on the core nitrogen concentration is discussed in section 5.2. These results indicate that there are differences between launching N atoms and nitrogen containing molecules, but that launching N atoms is an acceptable approximation. Also in SOLPS simulations only a small difference was found between starting $N_2$ molecules and N atoms [136].

- The transport of particles perpendicular to the magnetic field lines is modeled in DIVIMP via an anomalous perpendicular diffusion coefficient of $D_\perp$, which is constant over the whole computational domain. A diffusion coefficient of $D_\perp = 0.5$ m$^2$s$^{-1}$ was applied in the calculations presented in this work. This value was adopted from the SOLPS plasma background simulation and is in the typical range [134, 135]. Increasing the diffusion coefficient to $D_\perp = 1$ m$^2$s$^{-1}$ leaves the outer divertor deposition unaffected and decreases the nitrogen concentration in the core plasma. The motion of ions due to classical cross field drifts (see section 2.5) is not included in DIVIMP.

- The standard expression for the temperature gradient force is taken from the fluid approximation and neglects kinetic effects. The importance of the effects described in Ref. [53] was checked by calculating one re-distribution matrix with the DIVIMP implementation of the Reiser collision operator[m]. A significant effect was only found for the tungsten transport in parts of the outer divertor, which has no impact on the presented results.

- DIVIMP assumes (as WallDYN) an infinite aspect ratio, that means the toroidal curvature of a tokamak is neglected in DIVIMP. This curvature causes the so called mirror force which can modify the movement of the ions parallel to the magnetic field. The curvature could also play a role for the neutral transport, because it opens a line of sight transport channel to wall elements which cannot be reached directly in a straight device.

### 3.3.5 Plasma backgrounds

An essential input into WallDYN and DIVIMP is the plasma background, i.e. spatially resolved information about plasma parameters like electron and ion densities, temperatures and the mean ion velocity. Plasma backgrounds can be generated with sophisticated models like SOLPS or with simpler models like the *onion-skin model* (OSM) [8, 132, 137, 138].

---

[m]This implementation of the collision operator has not been tested and results based on it should currently not be published [139].

**SOLPS**

The simulations presented in this work are largely based on plasma backgrounds generated with the SOLPS5.0 code package by L.A. Mantila [103, 104]. SOLPS (*Scrape-Off Layer Plasma Simulation*) consists mainly of two coupled codes, *EIRENE* and *B2.5* [41]. *EIRENE* is a Monte-Carlo code which calculates the neutral transport on a kinetic level [140]. *B2.5* is a two dimensional Braginskii multi-fluid model [52] where electrons and each ion charge state are treated as individual fluid species. SOLPS calculates a self-consistent solution of the plasma background. Version 5.0 of SOLPS includes also the perpendicular transport of ions caused by classical cross field drifts ($E \times B$ and diamagnetic) [141].

Two SOLPS plasma backgrounds are employed to reproduce the observed plasma states (see section 3.2.2). The first one corresponds to the plasma state without N-seeding and higher $T_e$ at the outer strike line. The second solution includes the effect of N-seeding on the plasma, reproducing the low $T_e$ divertor conditions.

SOLPS is a sophisticated model, but still the measured plasma parameters are only partly reproduced. Generally the plasma parameters in the outer divertor are reasonably matched by SOLPS plasmas. Deviations exist mostly in the inner divertor region and in the simulated ion flows [42]. The ion flow is calculated self-consistently in SOLPS, but the simulated flows are smaller than the measured ones (see section 2.4). Another shortcoming of SOLPS is the computational grid, which covers only the part of the SOL directly connected to both divertors via magnetic field lines (see Fig. D.1). For the simulations employed in this work the gap between the SOLPS plasma and the wall was bridged with an OSM solution as described in Ref. [44] (see Fig. D.2).

**Onion-skin model**

In the onion-skin model, the plasma is considered to consist of independent, radially separated one dimensional flux tubes. For each of these flux tubes a solution is generated which interpolates a set of prescribed plasma parameters. Usually the prescribed parameters are taken from measurements and specified at three poloidal positions, an upstream position and the two intersections with the wall. The 2D plasma background is simply assembled by combining 1D solutions. The 1D models are usually based on less sophisticated equations than the fluid equations used in SOLPS. This simplicity of OSM provides a certain flexibility, which is not available in SOLPS.

The equations employed in the *DIVIMP OSM SOL28* model, the DIVIMP OSM

solver applied for this work[n] are [142, 138, 143]:

$$\frac{d}{ds}\left(n_i v_i\right) = S_{particle} + A_{particle}$$

$$\frac{d}{ds}\left(n_i(T_e + T_i) + m_i n_i v_i^2\right) = S_{momentum} + A_{momentum}$$

(3.19)

The equations represent particle and momentum conservation for steady state conditions ($\frac{\partial n}{\partial t} = 0$ and $\frac{\partial nmv}{\partial t} = 0$). In these equations $s$ is the coordinate along the flux tube, $n_i$ the ion density, $v_i$ the ion velocity, $S_{particle}$ and $S_{momentum}$ the particle and momentum source from ionized neutrals. $A_{particle}$ and $A_{momentum}$ are 'anomalous' source terms which are used to fit the model to the boundary conditions. The temperature profile (along a flux tube) is calculated by interpolating the temperature boundary conditions with a model that assumes heat transport via heat conduction.

The source terms $S$ presents an extension to the basic OSM. They are calculated by iterations with EIRENE [140] simulations of the neutral hydrogen transport. Another specific feature of the DIVIMP OSM solver is the possibility to manually specify the ion flow velocity [44]. As discussed in section 2.4, the SOL flow velocities are important for the impurity transport and not correctly reproduced in SOLPS simulations.

**Employed plasma backgrounds**

The most sophisticated approach to reproduce the experimental conditions should be a combination of the SOLPS plasma backgrounds, extended by an OSM solution to the main wall: The background corresponding to the non-seeded high $T_e$ plasma is applied from the beginning of the simulated phase at 1.3 s (discharge time) to 1.7 s and from 2.5 to 3.2 s. The background corresponding to the N-seeded low $T_e$ plasma is employed from 1.7 to 2.5 s and from 3.2 to 4.55 s. This is about 0.2 s longer than the experimental flattop phase. The experimental measurements are mostly compared to this simulation. In simulations which employ only one background the high $T_e$ solution is used for non-seeded discharges (e.g. for the simulation of discharge #29698), for N-seeded discharges (e.g. in section 5.4) the low $T_e$ solution has been applied. In fact, simulations employing only the low $T_e$ SOLPS plasma background give very similar results to the simulation switching between the two SOLPS backgrounds.

On top of this, some of the results are compared to WallDYN simulations based on OSM plasmas. Firstly, this allows to create customized plasma backgrounds which help to better understand the transport of nitrogen through the plasma. Secondly, OSM plasma solutions are routinely used in the interpretation of material migration

---

[n] For the OSM plasma in the far SOL, which is used to extend the SOLPS simulations up to the main wall, simpler equations (instead of (3.19)) are used as described in [44].

experiments, for example in Refs. [134, 22]. The comparison of simulations based on SOLPS and OSM solutions allows to test the applicability of OSM results.

The OSM plasma backgrounds are based on the low $T_e$ SOLPS plasma solution, which has been found to be more appropriate for the simulation of nitrogen deposition. The boundary conditions given by this SOLPS solution are specified at the divertor targets and the low field side midplane. Based on these three radial profiles a 'simple' OSM background has been generated. Two further OSM solutions with customized parameters have been employed for this work:

- A background where the flows are modified with respect to the 'simple' background by imposing additional boundary conditions on the flows (see Fig. D.5).

- A background where the flows and the outer divertor plasma are modified. This OSM solution has a lower plasma temperature in the outer divertor and is closer to the SOLPS background in this region (see Fig. D.6).

The second and the third OSM background are explained more detailed at their application in section 5.1.3. Plots of the electron temperature, electron density and flow velocity of these plasma backgrounds are given in appendix D.

# Chapter 4

# Implantation and erosion of nitrogen in tungsten

This chapter summarizes the results on nitrogen accumulation and loss gained by small scale laboratory experiments and computer simulations. Section 4.1 focuses on the study of the basic interaction of nitrogen and tungsten and the erosion of tungsten nitride by deuterium. The results are derived from well defined ion beam experiments with XPS and NRA analysis. Section 4.2 presents results from SDTrimSP modeling on the simultaneous bombardment of tungsten with deuterium and nitrogen. In the next chapter the migration of nitrogen in ASDEX Upgrade is discussed based on dedicated experiments performed in this fusion experiment and WallDYN simulations.

## 4.1   Results from laboratory experiments

### 4.1.1   Nitrogen implantation at ambient temperature

Nitrogen (N) ions with 2.5 keV and 500 eV per atom were implanted into tungsten (W), which was previously polished and annealed as described in section 3.1.3 and cleaned by in-situ argon sputtering. The N content was monitored by measuring the XPS peak ratio N $1s$/W $4f$ (see section 3.1.1). The results are presented in Fig. 4.1 together with intensity ratios calculated via the forward calculation (see section 3.3.2) from SDTrimSP depth profiles (see section 3.3.1 and 2.3). For the implantation at 2500 eV one simulation with the standard surface binding energy (SBE) for N of around 4 eV and another simulation with $SBE_N = 0$ eV are shown. Also for the implantation at 500 eV two SDTrimSP simulations are shown. They differ in the maximum permitted N concentration (see section 3.3.1). The N concentration is not limited for the dotted curve and limited to 50 % for the red dashed curve. In

this simulation the N inventory exceeding the maximum concentration is artificially removed.
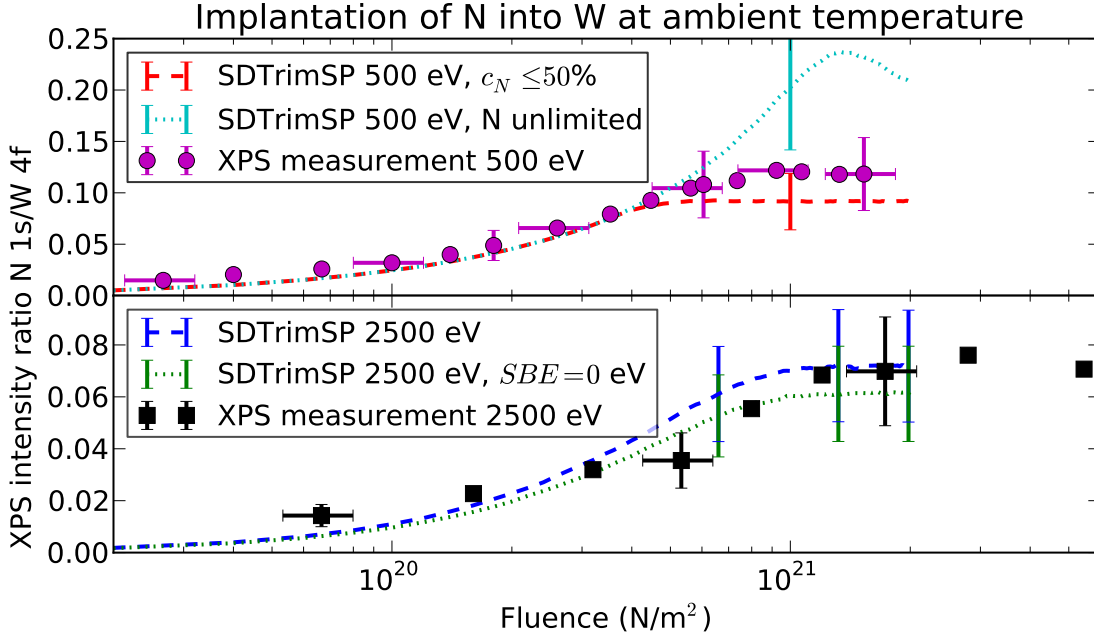


**Figure 4.1:** *XPS measurement of N accumulation in W under N bombardment with 2.5 keV (lower figure) and 500 eV (upper figure): The squares and circles represent the measured data points, the continuous curves were calculated from SDTrimSP depth profiles via the XPS forward calculation (section 3.3.2). For the implantation at 2.5 keV there is a good agreement between experiment and simulations. The surface binding energy (SBE) has only a small influence on the simulation. For the implantation at 500 eV the N accumulation is limited by the onset of N effusion from W, so that the N concentration in the simulation (red dashed curve) must be limited to 50 %.*

For implantation at 2.5 keV both simulations agree within the uncertainties with the measurement. The depth profile calculated by SDTrimSP for 2.5 keV implantation was shown in Fig. 3.14. Reducing the SBE of N to 0 eV only reduces the N content in the uppermost two layers (4 Å), with a very small impact on the predicted XPS intensities. For 2.5 keV N implantation, there is strong sputtering of N and W by the N ions. The resulting re-erosion of N limits the N concentration to less than 50 %. The agreement of measurement and simulation for 2.5 keV verifies that this process is correctly described by SDTrimSP.

This is different for the implantation with 500 eV, where the unlimited and the limited SDTrimSP simulations only agree at low fluences. At such low fluences the N accumulation is governed by reflection yield and implantation depth of N. The saturation of the N content at large fluences is determined by the loss of N from the material due to re-erosion and effusion. The erosion of W and N at the surface by sputtering is visible in the N depth profiles shown in Fig. 4.2. However, the N

re-erosion is significantly lower for 500 eV than for 2500 eV N implantation. Under these conditions the N concentration in the maximum at about 2 nm depth would exceed 50 %. Thus, only the simulation with a manual limit for the N concentration gives a good match to the measurement, while the unlimited simulation is far off (Fig. 4.1). This demonstrates that under these implantation conditions the N accumulation is not sufficiently limited by the physical processes included in SDTrimSP, but additionally the effusion of N from W is important.

One could further improve the fit by adjusting the maximum concentration of N. However, due to the rather large uncertainty in the data, such a further refinement is not justified. Nevertheless, a comparison to the simulation without limit on the N concentration shows a discrepancy which is significantly larger than the uncertainty. Based on these results (good agreement for a maximum concentration of 50 %) and known phases of tungsten nitrides [70], the maximum concentration of N in W at room temperature should be between 33 % and 66 %.

As discussed in sections 3.1.1 and 3.3.2, most of the uncertainty in the measurement and simulation of XPS intensities is caused by systematic effects. Therefore, even though absolute values may not be that precise, the scatter within a measurement series is small and the relative behavior can be compared with significantly better accuracy.

The absolute N areal density retained in the W surface after implantation was measured with nuclear reaction analysis (NRA, see sec-



**Figure 4.2:** *N depth profile evolution with fluence under 500 eV N bombardment simulated with SDTrimSP. The depth is measured from the original surface, so that the erosion is visible in the shift of the depth profile to the right. The maximum concentration of 50 % is reached around a depth of 2 nm.*

tion 3.1.2). At 2.5 keV the measurement yields a N areal density of $2.3 \cdot 10^{20}$ N/m$^2$, which is somewhat above the areal density of $1.8 \cdot 10^{20}$ N/m$^2$ predicted by SDTrimSP. At 500 eV NRA yields an areal density of $1.1 \cdot 10^{20}$ N/m$^2$ which is in agreement with the N areal density from the SDTrimSP simulation of $1.15 \cdot 10^{20}$ N/m$^2$.

## 4.1.2 Erosion of tungsten nitride layers

In order to study the depth distribution and erosion of N implanted into tungsten, such layers have been bombarded with argon and deuterium.

The XPS measurement of the erosion with argon, often denoted as sputter depth
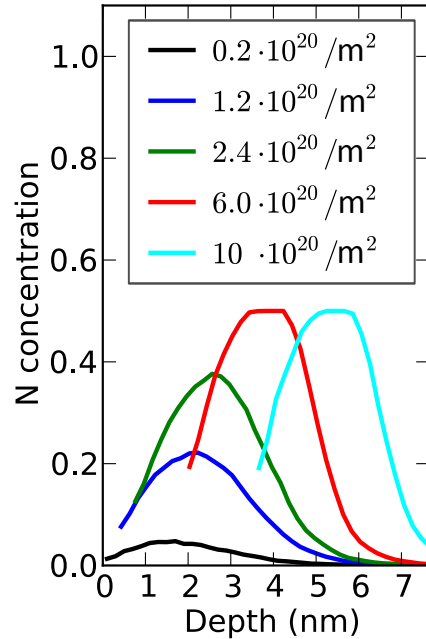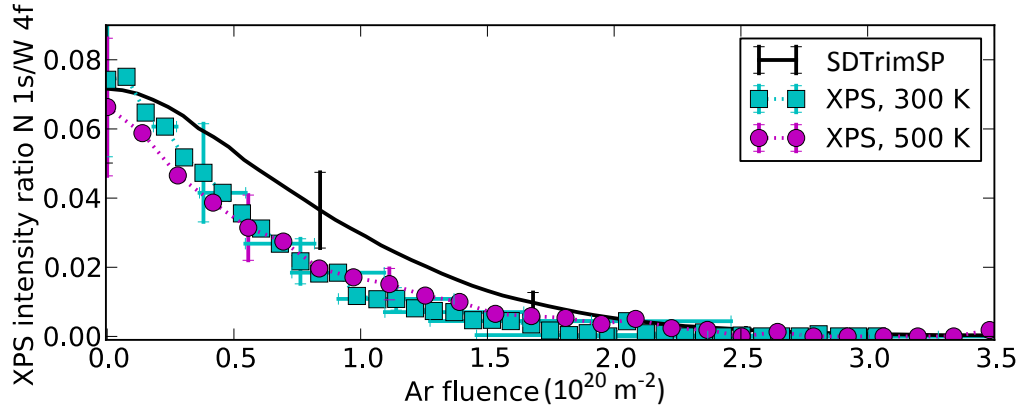
**Figure 4.3:** *A $W_xN$ layer created by 2.5 keV N implantation is eroded by argon at 300 and 500 K. Simulation and measurement show a reasonable agreement.*

profiling [82], is presented in Fig. 4.3. Two samples were prepared by implantation of 2.5 keV N in W at ambient temperature and then eroded by 5 keV Ar bombardment at 300 and 500 K. Apart from a small difference in the initial values (see discussion of uncertainties in section 3.1.1) there is no significant difference between the measurements. In comparison to the simulation, the measured N $1s$ signal drops faster. This could indicate a shorter penetration depth of N. However, within the uncertainty, the measurements still agree with the SDTrimSP simulations.

In a fusion device, the species with the largest fluence impinging on the plasma-facing materials are hydrogen isotopes. To study the interaction of a $W_xN$ layer with incoming deuterium, such a layer created by 2.5 keV N implantation into W was eroded by 2.5 keV deuterium (D). This measurement is also presented in Ref. [93]. Because the mass-filtered ion source was used for the D bombardment, N implantation was performed with the unfiltered ion source. Measurement and SDTrimSP simulation of the D erosion experiment are shown in Fig. 4.4. Due to the steeper N implantation angle (see section 3.1.3), and in agreement with SDTrimSP, the N $1s$/W $4f$ ratio after this implantation is somewhat higher than the corresponding result in Fig. 4.1.

The sputter yield of D on W is very low (see Fig. 2.6). To reach the large fluence required to get a notable erosion, the D beam was only scanned over an area of 3 mm by 3 mm (see section 3.1.3). A lateral scan by XPS subsequent to the D bombardment confirmed that the resulting erosion was still homogeneous within the XPS analysis area.

Figure 4.4 shows a slower decay of the N content under D bombardment than predicted by SDTrimSP. The fluence required to reach a given intensity ratio in the simulation is almost a factor of 2 smaller than in the measurement. In the SDTrimSP simulation a thickness of about 6 nm (the nitride layer is about 10 nm thick, see Fig. 3.14), has been eroded at the final fluence of $1.5 \cdot 10^{22}$ D/m$^2$ (with a total sputter yield that drops from 0.044 to 0.022). According to SDTrimSP, the N erosion is
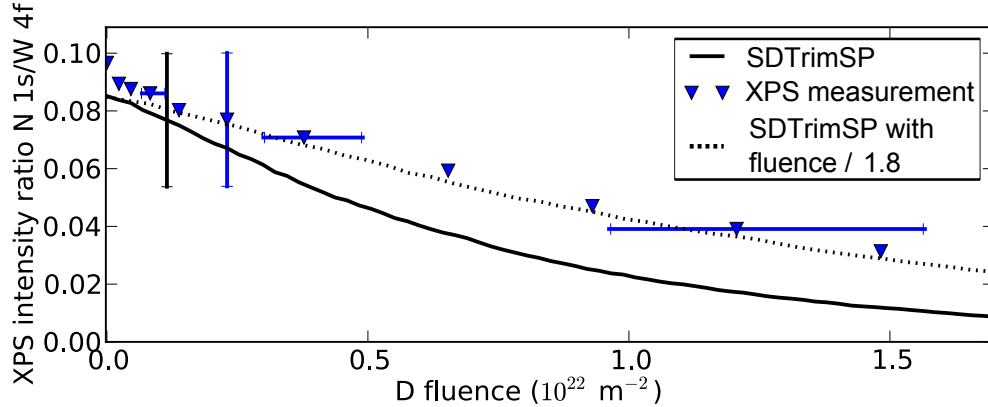
66

**Figure 4.4:** *A $W_xN$ layer created by 2.5 keV N implantation is eroded by D with 2.5 keV. The measured erosion is approximately a factor of two slower than the simulation.*

limited by the fluence needed to remove the W matrix. Therefore a possible explanation for the discrepancy between simulation and experiment is an overestimation of W sputtering by D in SDTrimSP. This explanation is supported by a comparison of sputter yields from experimental measurements and simulations given in Ref. [35, p. 116]. They show that the simulated sputter yield is about a factor of two too large for normal incidence of 2 keV D on W.

As the N erosion is smaller than predicted by SDTrimSP, a significant chemical erosion of N by the formation of volatile molecules with D at ambient temperature can be excluded. This is supported by measurements of the $W_xN$ erosion by D at 500 K. The resulting N erosion is the same as for D erosion at 300 K, while for a chemical erosion process one would expect a temperature dependence.

## 4.1.3 Temperature dependence

To study the temperature dependence of N accumulation and loss, dedicated high temperature experiments were performed. In the first experiment a $W_xN$ layer was created by implantation of 2.5 keV N at ambient temperature. Then the sample was heated and the N content in the surface of the sample was monitored with XPS. Figure 4.5 shows that above 900 K the normalized N $1s$ intensity decreases[a]. This decline is notably faster at 970 K. In a sputter depth profile subsequent to the heating phase, N could only be detected in the uppermost nanometers.

The loss of N from the surface region accessible to XPS suggests that N atoms must diffuse from this region, either to the surface to recombine or further into the sample. Diffusion coefficients for N in W, based on ion implantation and subsequent heating of the sample, have been published in Refs. [68] and [144]. However, tungsten

---

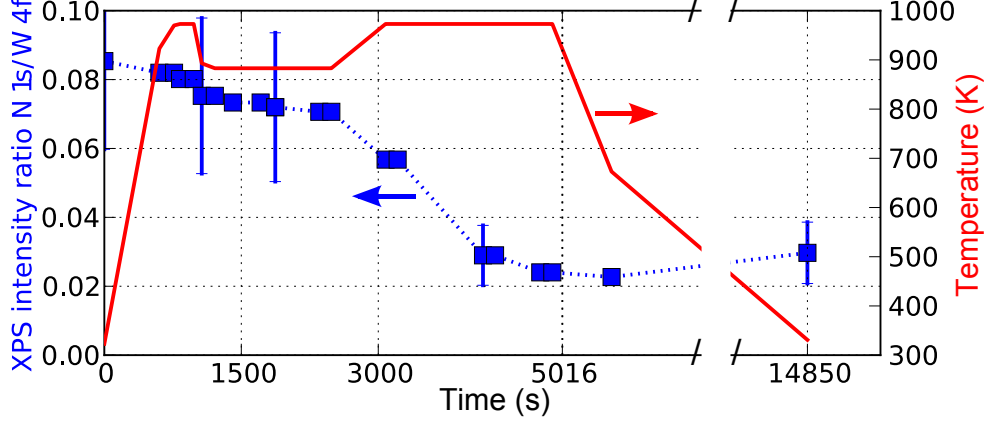[a]As can be seen in Fig. 4.7 there is no loss of N at 800 K.

**Figure 4.5:** *The N 1s/W 4f intensity ratio (blue marks referring to left axis) of a N implanted sample drops when the sample temperature (red curve referring to the right axis) rises above 800–850 K.*

nitride is actually a reaction-diffusion system, where the interplay of phase formation and diffusion has to be considered. According to the thermodynamic calculations discussed in Ref. [10] tungsten nitride should decompose at around 600 K. However, this has not yet been confirmed by experiments and the presented results show no sign for a loss of N at 600 K. This indicates that a phase transition at this temperature does not exist or is delayed by a low diffusivity of N.

To check whether the result shown in Fig. 4.5 is in agreement with published diffusion coefficients of N in W, the timescale for diffusion induced changes in the N content shall be estimated. Typically this timescale is estimated by $\tau \approx \frac{(\Delta x)^2}{D}$ with the diffusion coefficient $D$ and the length scale $\Delta x$. This estimate is only applicable under the assumption that the complete N content can contribute to diffusion. In contrast to that, the approach described in Ref. [145] and used in Ref. [68] to derive the diffusion coefficient, assumes that only solute N contributes to the diffusion. To estimate the timescale of the diffusion for a solubility controlled system, a modified expression has to be used:

The expression suggested in Refs. [68, 145] for the loss ($L$) of N with a solute N concentration $C_0$ and a diffusion coefficient $D$ is:

$$L(t) = 2\,C_0\sqrt{D\,t/\pi} \tag{4.1}$$

From this one can estimate the N loss time by substituting $L$ with the N content after implantation:

$$L \rightarrow \frac{\delta_N}{\rho_W} = \frac{\rho_N \cdot \Delta x}{\rho_W} = \frac{c_N \cdot \rho_W \cdot \Delta x}{\rho_W} = c_N \cdot \Delta x \tag{4.2}$$

$\delta_N$ is the N areal density in the implantation zone, $\rho_W$ the W volume density, $\rho_N$ the N volume density, $\Delta x$ the implantation zone thickness and $c_N$ the N concentration in the implantation zone. Neglecting the factor $\frac{2}{\sqrt{\pi}}$ and solving for $t$ gives:

$$\tau \approx \left(\frac{c_N}{C_0}\right)^2 \frac{\Delta x^2}{D} \tag{4.3}$$

The loss time becomes longer in comparison to the simple estimate $\tau \approx \frac{(\Delta x)^2}{D}$ as only the solute N contributes to the gradient driving the diffusion.

With the diffusion coefficient

$$D = 4.3\,(\pm 8.3) \cdot 10^{-4} \cdot \exp\left(-\frac{2.32(\pm 0.16)\,\text{eV}}{T}\right)\left(\frac{\text{m}^2}{\text{s}}\right) \tag{4.4}$$

from Ref. [68], a solubility of N in W of $C_0 = 2.5\,\%$ given in the same reference for 970 K, and assuming that a layer of $10^{-8}$ m with $c_N \approx 37\,\%$ needs to be depleted at a temperature of 970 K by diffusion, one obtains:

$$\tau \approx \left(\frac{c_N}{C_0}\right)^2 \frac{(\Delta x)^2}{D} \approx (15)^2 \frac{(10^{-8})^2}{5 \cdot 10^{-16}}\,\text{s} \approx 225 \cdot 0.2\,\text{s} \approx 45\,\text{s}$$

Within the error bars given for the diffusion coefficient in equation (4.4), the diffusion coefficient may drop to $D = 1\cdot 10^{-4}\cdot\exp\left(-\frac{2.5\,\text{eV}}{T}\right)\frac{\text{m}^2}{\text{s}}$. With this value for the diffusion coefficient the estimated timescale goes up by almost two orders of magnitude to $\tau \approx 2000$ s. This is comparable to the observed timescale of about 1000 s.

Another value for the diffusion coefficient of N in W was published in Ref. [144]. This study is based on a single crystal so that diffusion along grain boundaries cannot contribute. Unfortunately, the authors do not give error bars and a significant scatter in the raw data is visible. Ref. [144] reports two diffusion coefficients, one for diffusion driven by defects (created by the 100 keV ion implantation) with a very low activation energy, $D = 7 \cdot 10^{-18} \cdot \exp\left(-\frac{0.15\,\text{eV}}{T}\right)\frac{\text{m}^2}{\text{s}}$ and a second diffusion coefficient for bulk diffusion, $D = 1.24 \cdot 10^{-16} \cdot \exp\left(-\frac{0.75\,\text{eV}}{T}\right)\frac{\text{m}^2}{\text{s}}$. Ref. [144] does not distinguish between N in the solute phase and in the nitride, so for consistency the timescales were calculated assuming $\frac{c_N}{C_0} = 1$. The time constants based on these diffusion coefficients are 90 s and 8000 s, respectively. The timescale observed in the present experiments lies between these results.

As a conclusion it can be stated that the observed N loss for heating a $W_x N$ layer is in agreement with published diffusion coefficients. However, the published coefficients have a large scatter and do not consider the possible dependence of the diffusion coefficient on the composition, as observed for carbon diffusion in tungsten [146].

The finding that diffusion only occurs above 800 K differs from the observations reported in Ref. [10], where a reduction in the N content was already observed for N implantation at a sample temperature of 600 K. For this reason, further experiments with 2.5 keV N implantation were performed, where the sample temperature during the implantations was varied. The corresponding XPS measurements are shown in
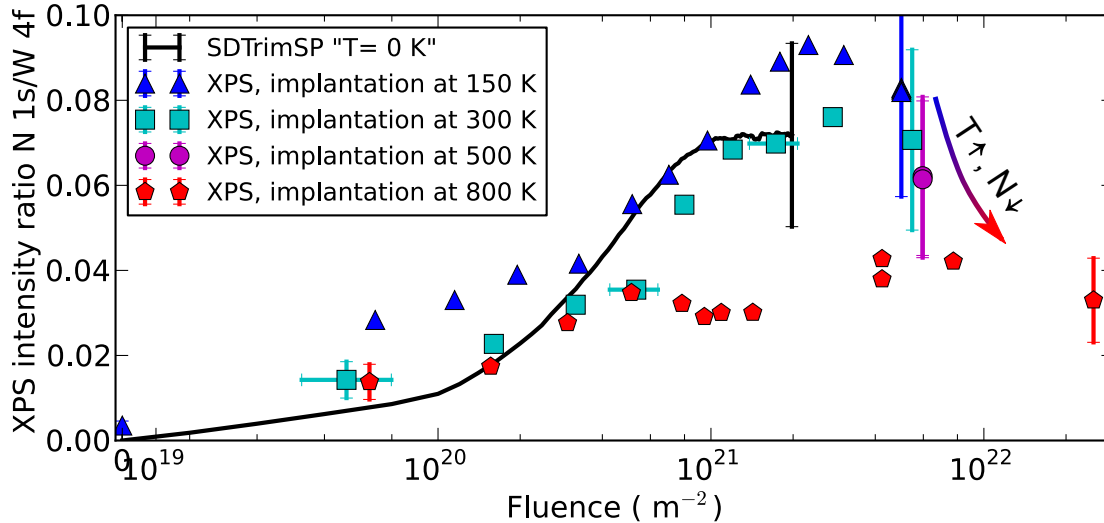
**Figure 4.6:** *N accumulation as a function of the 2.5 keV N fluence for different sample temperatures during implantation. The N 1s/W 4f intensity ratio drops with increasing temperature.*

Fig. 4.6. As discussed in section 3.1.1 the uncertainty is mostly due to systematic errors, so the relative accuracy of the presented measurements is notably smaller than the given error bars. One can see that there is almost no difference between 300 and 800 K implantation at low fluences. However, at 800 K the N content saturates at a much lower level than at 300 K. The implantation at 150 K seems to have a constant offset from the one at 300 K. The adsorption of N at the surface would be a possible explanation. However, the N 1s signal does not drop when the sample is heated to 350 K after the implantation. As discussed in section 4.1.1 the N implantation at 300 K is reproduced by SDTrimSP (without the need to set a maximum concentration). As can be seen from Fig. 4.6, the implantation at 150 K agrees with the 2.5 keV SDTrimSP simulation within the error bars, too. Diffusion and chemical effects, which are not included in the BCA calculations (see section 2.3), become more important with increasing temperature, so the best agreement of SDTrimSP with the experiment can be expected for low temperatures.

From the XPS measurements it cannot be concluded whether the N content after implantation at elevated temperature is actually lower, or whether N has diffused out of the XPS range into greater depths. Therefore, the integral N content was determined with NRA. The N areal density for the 800 K implantation decreased to $1.5 \cdot 10^{20}$ N/m$^2$ (from $2.3 \cdot 10^{20}$ N/m$^2$ for ambient temperature implantation), so that the amount of retained N is actually reduced. These results show, together with the ones presented in Ref. [10], that the N content in saturation drops not only for an implantation above 800 K, but decreases rather continuously with increasing implantation temperature.

To confirm the difference between (1), subsequent implantation and heating, with
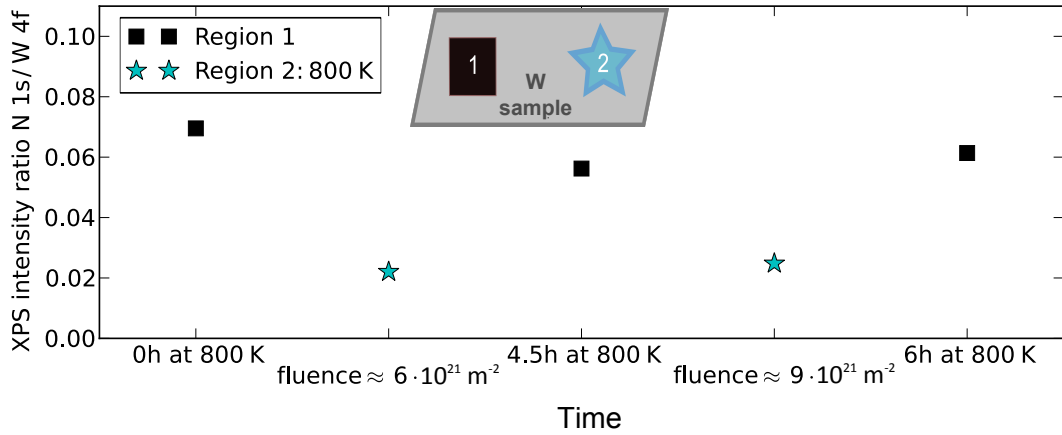
**Figure 4.7:** *The black squares reflect the N content in region 1 of the sample, implanted at ambient temperature with N and heated subsequently to 800 K. There is no indication for a loss of N from this region. Region 2 of the sample was implanted after the sample was heated to 800 K. The N content (cyan triangles) in region 2 saturates at a much lower level. This confirms that there is a difference between subsequent N implantation & heating and implantation into a heated sample.*

(2), the implantation into a heated sample, a special experiment was performed: One part of a sample was implanted at ambient temperature with a N fluence of $6 \cdot 10^{20}$ N/m$^2$. Then the sample was heated to 800 K. XPS measurements shown in Fig. 4.7 confirm that the N signal in the corresponding region 1 (squares) did not change over several hours. Between the XPS measurements in region 1, N was implanted into another part (region 2) of the heated sample. As shown in Fig. 4.7 the N content in region 2 of the sample (stars) saturates at significantly lower normalized N $1s$ intensities.

Due to technical limitations this measurement was performed with the non-monochromatic X-ray source. The shown intensities were derived simply with a Shirley background subtraction. Therefore, the absolute values cannot be compared to others given in this work. Nevertheless, this does not affect the qualitative conclusions.

From the temperature dependence described here and in Ref. [10], it seems clear that there is a gradual reduction of the N content with increasing *implantation* temperature. There is even an indication for a continuation of this trend below ambient temperatures. Possible mechanisms causing this temperature dependent N retention are radiation enhanced diffusion [147, 26] or a competition between diffusion of the solute nitrogen and phase formation. Indications for an impact of damages created by ion bombardment on the diffusion coefficient have already been found in Ref. [144], however, for a significant higher ion energy and for subsequent implantation and heating.

## 4.1.4 Summary of results from laboratory experiments

This section presented experimental results on the implantation and retention of nitrogen in tungsten surfaces. In laboratory experiments the surface of tungsten samples was observed by in situ XPS diagnostics, which allowed to follow the surface composition evolution during N implantation, subsequent argon and deuterium bombardment and temperature variations. A special evaluation procedure has been developed for $W_xN$ XPS spectra as described in section 3.1.1. It employs calibration factors to correct Shirley background based peak intensities for the dependence on user chosen parameters and the N $1s$ peak extending into the W $4p$ peak. The measurements of N implantation and erosion could be interpreted by SDTrimSP simulations based on the binary collision approximation. To this end a forward calculation has been developed which converts depth profiles from SDTrimSP simulations to XPS intensity ratios (section 3.3.2). The forward calculation is not restricted to the studies presented in this work but for instance can be used for the interpretation of sputter depth profiles.

The main conclusions from this section are:

- 2.5 keV N implantation in tungsten at ambient temperature is well described by SDTrimSP. For this implantation energy, the achievable N concentration is limited by physical re-erosion to below 50 %.

- For N implantation at 500 eV the N content is limited by effusion of N. Effusion limits the concentration of N in tungsten to $c_N \leq 50$ %, in agreement with the known phase of WN.

- The erosion of tungsten nitride layers by argon is correctly described by SDTrimSP. The erosion of tungsten nitride by 2.5 keV D is overestimated by SDTrimSP. There is no evidence for chemical erosion of N by D, as the sputtering is even lower than predicted by SDTrimSP.

- The diffusive loss of implanted N is negligible up to 800 K, sets in at about 900 K and is significantly faster at 970 K. The observed time scale for the N loss is in agreement with published diffusion coefficients for N in tungsten.

- For implantation into a heated tungsten sample, the N loss is already enhanced below 800 K. This difference between N implantation before heating the sample and implantation into a heated sample resolves the apparent contradiction between Refs. [10] and [11]. A possible explanation for this behavior is the occurrence of radiation enhanced diffusion.

- With these new results the sudden release of large amounts of N from tungsten walls at a possible phase transition at 600 K [10] appears unlikely. Further studies of the temperature dependence, for example high resolution XPS measurements to look for indications of a phase change, are required to better understand the observed behavior.
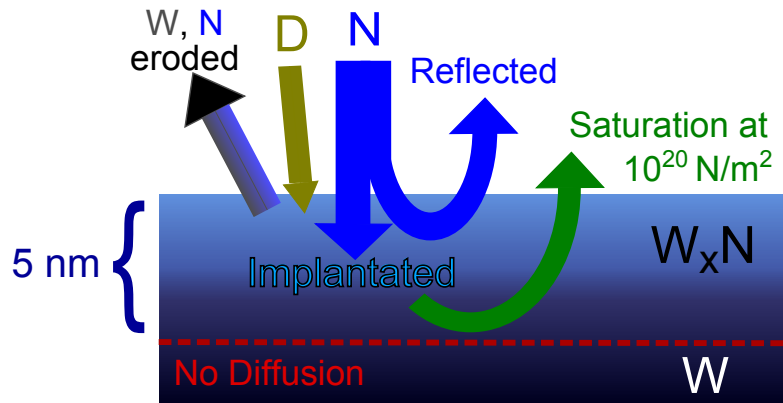
**Figure 4.8:** *Impinging N atoms are either implanted or reflected. The implantation depth of N is about 5 nm. Energetic D and N can (re-)erode N and tungsten atoms. An additional diffusive loss channel limits the N concentration to about 50 %, corresponding to an areal density of about $10^{20}$ N/m$^2$.*

The resulting picture on the interaction of D, N and tungsten is summarized in Fig. 4.8: N implantation induces the formation of tungsten nitride. N does not diffuse in tungsten below 800 K and is bound to the implantation zone. At some point the losses of N caused by re-erosion or effusion[b] balance the implantation. This saturation takes place for N areal densities of the order of $10^{20}$ N/m$^2$. The precise value of the saturation areal density depends through the implantation depth and physical re-erosion on impact angle, energy and composition of the incoming beam.

For a more accurate determination of the maximum concentration to be used in SDTrimSP and to study the implantation at lower energies, the presented work was continued by a diploma student under my supervision [93]. In the course of this work the forward calculation proved to be a valuable tool for planning experiments. It indicates the experimental parameters which should give the most meaningful results and and helped to improve the depth resolution of argon sputter depth profiling by optimizing the energy of the Ar projectile. The new measurements, including N implantation at tokamak relevant energies of 300 eV/N, confirmed that SDTrimSP simulations with a maximum N concentration of 50 % give a precise prediction of the experimental observations.

## 4.2 Simulation of D and N co-bombardment

### 4.2.1 SDTrimSP simulations

The first wall of a nuclear fusion experiment is exposed to simultaneous bombardment of D and N with varying energies and composition. In sections 4.1.1 and 4.1.2

---

[b]A physical picture of the N loss mechanism which could be responsible for the observed behavior is given in section 4.2.4.

it was shown that the implantation of N in W and its erosion by Ar are well described by SDTrimSP simulations. Considering the uncertainties on particle fluxes and energies in a fusion reactor, the discrepancy between measurement and simulation for the erosion of W and $W_xN$ layers by D is acceptable. Furthermore, in the presence of heavier ions, like N, sputtering is done dominantly by the heavier species (see section 2.3.3). Motivated by the success of SDTrimSP in simulating the laboratory experiments, this code was used to simulate the N accumulation in W under D-N co-bombardment as it occurs on the first wall of a fusion experiment.

The predicted fluence dependent N areal density in W is shown in Fig. 4.9. The simulations were done with varying energies of the ions and a varying beam composition. The fraction of N in the beam is shown in Fig. 4.9 by the gray numbers next to the curves. Results are given for N fractions in the beam of 100, 15 and 2 %. In N-seeded fusion plasmas, core N concentrations in the low percent range are reached [148, 136] and the concentration in the divertor plasma is typically somewhat higher [62]. The energy of the ions is indicated by the color of the line and the legend gives the values for D (15 eV, 80 eV, 160 eV and 500 eV). As N becomes multiply ionized above an electron temperature of 4 eV and the energy of impinging ions is mainly determined by the sheath acceleration (see section 2.3), the impact energy of N was set to twice the energy of D. The maximum N concentration in the simulations was set to 50 %, based on the experimental results from section 4.1.1. The impact angle for the presented result was, as in the XPS experiments, 40° with respect to the surface normal. A somewhat larger number of simulations was given in Ref. [16].
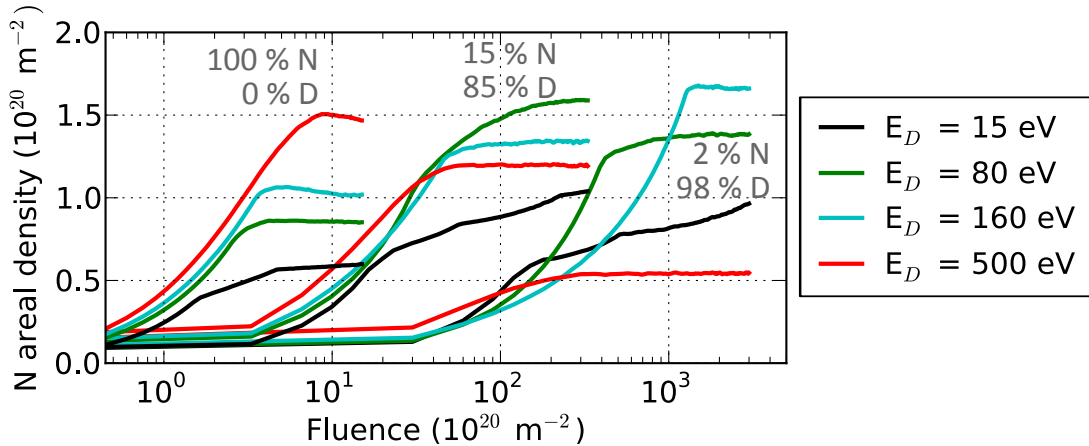


**Figure 4.9:** *SDTrimSP simulations of the N accumulation in a W surface under D-N co-bombardment for different energies and beam compositions. The N energy was twice the D energy, $E_N = 2\,E_D$, the angle of incidence 40°. The gray numbers indicate the beam composition for the nearby curves. The saturation N areal density varies between $0.5 \cdot 10^{20}$ N/m² and approximately $1.5 \cdot 10^{20}$ N/m².*

The most notable effect of the beam composition is the required fluence to reach steady state. While it is obvious that the total fluence (D + N) required to reach steady state increases with decreasing N fraction in the beam, a closer look shows

that also the partial N fluence (total fluence times N fraction) needed to reach saturation increases. This is partly due to the erosion of N by D, working against the N implantation. Finally, the slow increase of the N content at high fluences can be attributed to the recoil implantation of N by D. This will be discussed later in more detail. For N concentrations in the percent range and a flux of $10^{23}$ m$^{-2}$s$^{-1}$, as it is typical for the strike line region of N seeded fusion plasmas, it takes 0.1 s to 1 s until the N content saturates.

The steady state N content at large fluences is given by the balance of N implantation and loss. The N areal density in steady state varies from about $0.5 \cdot 10^{20}$ N/m$^2$ (for low energies with pure N bombardment and high energies with low N fraction) to approximately $1.5 \cdot 10^{20}$ N/m$^2$ (for high energies with pure N bombardment and medium energies with low N fraction). The large N accumulation for medium energies and low N fractions in the beam is again caused by the recoil implantation of N by D, as will be discussed in the next paragraph. Further simulations, published in Ref. [16], show that the N areal density has a maximum at a N fraction in the beam of 5–10 % and decreases for even lower N fractions.

The same set of simulations as just discussed for an impact angle of 40°, was also performed with an impact angle of 60° with respect to the surface normal, as suggested in Ref. [25]. These simulations are shown in appendix C. On average, the N areal densities are reduced due to a smaller penetration depth of the impinging ions and increased sputtering for this more oblique angle.

## 4.2.2  Depth profiles and recoil implantation

The N depth distribution could be expected to be mainly governed by the implantation depth, i.e. energy, of the N ions. However, from the SDTrimSP results it becomes apparent that recoil implantation of N by D significantly increases the implantation depth of N and thereby increases the N content. In both cases, D-N co-bombardment (Fig. 4.10) and subsequent implantation of N and bombardment with D (Fig. 4.11), the N content directly at the surface is reduced, but N is also pushed into greater depths by D.

The dependence of the steady state N content on the beam composition in Fig. 4.9 is different between D energies of $E_D = 500$ eV and lower values. At $E_D = 500$ eV the N content decreases with increasing D fraction in the beam, because the erosion by D has a larger impact than the recoil implantation. At lower energies the erosion by D becomes less effective, so for 160, 80 and 15 eV the N content first increases with decreasing N fraction, as more N can be recoil implanted before it becomes eroded. Around a N fraction in the beam of 5–10 % the N areal density reaches a maximum and then drops for even smaller fractions of N in the beam [16]. This maximum in the N areal density for a given energy is accompanied by a change in the shape of the depth profile as can be seen in Fig. 4.10 for simulations with $E_D = 160$ eV. A

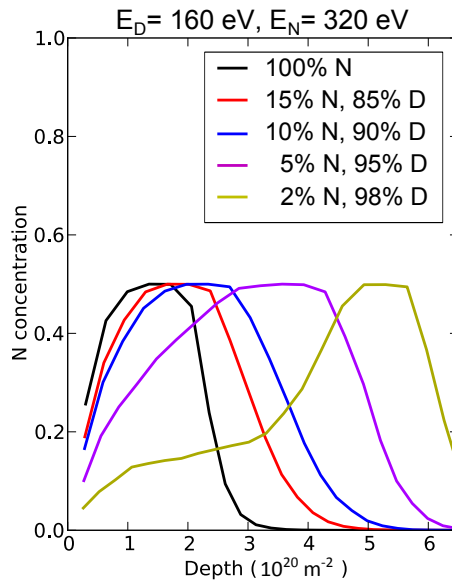**Figure 4.10:** *Simulated N depth profiles for $E_D$=160 eV and $E_N$ = 320 eV at large fluences. A depth of $10^{20}$ m$^{-2}$ corresponds to about 1 nm. The depth profile for 5 % N has the largest N areal density of all presented simulations.*
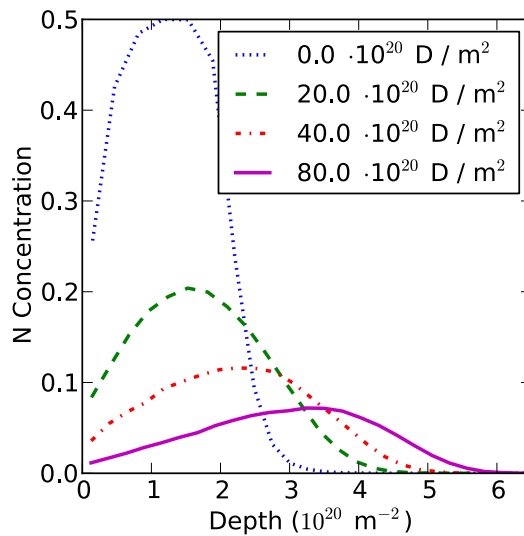


**Figure 4.11:** *Evolution of N depth profile under D bombardment from a SDTrimSP simulation: A $W_x N$ layer created by 320 eV N implantation into W is eroded with D at 160 eV. With increasing D fluence N is eroded, but also implanted into greater depth. D with 160 eV cannot erode tungsten directly. Still D-N collisions in the surface create N recoil atoms with an energy sufficient to sputter some W atoms. A depth of $10^{20}$ m$^{-2}$ corresponds to about 1 nm.*

plateau with about 15 % N concentration reaching from a depth[c] of $1 \cdot 10^{20}$ m$^{-2}$ to $3 \cdot 10^{20}$ m$^{-2}$ develops. At a depth of $5 \cdot 10^{20}$ m$^{-2}$, where no N is present in the pure N simulation, a peak in the N concentration with up to 50 % N appears. This shape is formed by the combination of preferential erosion at the surface and recoil implantation into the depth. A peculiar feature of the simulations with 160 eV D energy and low N fraction are the sharp edges in the fluence dependence. These edges are caused by the limitation of the maximum N concentration. They are especially sharp for the given parameters because this maximum concentration is reached over a large depth interval at the same time. This is different from the other simulations where the maximum concentration is first reached at a smaller depth interval, while recoil implantation still increases the N content in larger depth.

Due to the low momentum transfer in collisions between D and W, W is mainly sputtered by N (see Fig. 2.6). Even for $E_D = 500$ eV and an N fraction of 2 % in the incident beam, more than 50 % of the W erosion is due to N. No W sputtering at all takes place in the simulations with $E_D = 15$ eV. As already observed in Ref.[10], for pure N bombardment the accumulation of N reduces the W surface concentration and as a consequence the W partial sputter yield drops by up to 30 %. This shielding effect is reduced under D-N co-bombardment, as the N concentration close to the surface decreases (Fig. 4.10), and totally vanishes for 2 % N in the beam.

### 4.2.3    Comparison to WallDYN surface model

The BCA model used in SDTrimSP successfully reproduced the experimental observations in section 4.1 and could be used to simulate D-N co-bombardment. However, this model is too expensive to be directly used in large scale migration simulations like WallDYN. Anyways, it is questionable whether such a detailed model would be reasonable, as the composition (including further impurities) and impact parameters of the incoming flux are only known approximately and the surface has a considerable roughness.

It thus seems appropriate to include a model which just limits the N areal density to about $10^{20}$ N/m$^2$. This value reproduces the SDTrimSP simulations within a factor of two, a reasonable accuracy regarding the uncertainties in the input parameters. A model based on this idea has been presented in section 3.3.3.

Figure 4.12 gives a comparison of the SDTrimSP D-N co-bombardment simulations with $E_D = 80$ eV from Fig. 4.9 to calculations employing the WallDYN surface module. There are three WallDYN simulations (dashed curves) using the saturation model described in section 3.3.3. For pure N bombardment there is a good agreement between SDTrimSP and WallDYN simulations. The N concentration has to be limited in both simulations to get this result: In SDTrimSP the maximum concentration for each interval is limited to 50 %. In WallDYN, the N concentration in the

---

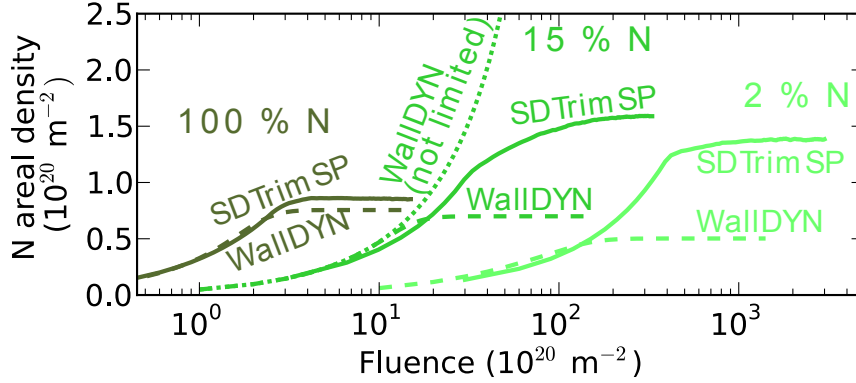[c]The depth is given as an areal density as discussed in section 3.3.1.

**Figure 4.12:** *Comparison of the WallDYN surface model (dashed lines) to the SDTrimSP simulations (solid lines) for $E_D=80$ eV $E_N=160$ eV presented in Fig. 4.9. The N content in the WallDYN model without limitation of the N concentration (dotted curve) rises continuously.*

reaction zone, with a nominal thickness of 4 nm, is limited to 30 %. With decreasing N fraction the discrepancy between the SDTrimSP simulation and the result from the WallDYN surface model increases. One simulation without limitation of the N concentration in the reaction zone is shown for a N fraction of 15 % in the incoming flux (dotted curve). One can see that the N areal density in this simulation rises steadily, in contradiction to the experimental observations given in sections 2.7 and 4.1.

As explained in section 3.3.3 erosion and reflection fluxes in WallDYN are based on fits to static SDTrimSP simulations. For small fluences the N inventory is determined by the reflection yield and therefore very similar in both models. At larger fluences N re-erosion and effusion limit the N accumulation. The N content saturates when effusion and re-erosion balance the implantation. In detail, these processes depend on the depth distribution of N which is not taken into account by WallDYN. With decreasing N fraction the re-erosion increases in the WallDYN simulation and the predicted N areal density consequently decreases. In reality, N re-erosion is lower than predicted by the WallDYN model due to depth profile effects. Hence, the WallDYN model has a tendency to underestimate the N areal density. Further comparisons between WallDYN and SDTrimSP simulations are given in section 5.1.

## 4.2.4 Summary of co-bombardment simulations

This section presented simulations of the N accumulation under D-N co-bombardment. The main results are:

- SDTrimSP predicts a strong modification of the N depth distribution due to N recoil implantation by D. This mechanism increases the N penetration depth

by more than a factor of two. It can be expected that this mechanism of recoil implantation is not restricted to the implantation of N in tungsten, but generally appears when a heavy substrate is bombarded with hydrogen and a further intermediate element (like the fusion relevant elements Be, B, C and maybe even Fe).

- The N content in the uppermost 1–2 nm is depleted due to preferential erosion by D. This preferential erosion seems to undo the W shielding effect, which in Ref. [10] lead to a reduced tungsten erosion under pure N bombardment.

- The N saturation areal density depends on impact angle, energy and composition of the incoming flux. A maximum appears in the saturation N areal density at a N fraction in the incoming beam of a few percent. Nevertheless, a value of $1 \cdot 10^{20}$ N/m$^2$ for the saturation areal density matches all simulations within a factor of 2.

- Based on the above results a saturation model for N in tungsten has been implemented into WallDYN as described in section 3.3.3. A comparison of this model to SDTrimSP simulations shows a good agreement for pure N bombardment but a tendency to overestimate N re-erosion under D-N co-bombardment.

It should be noted that the results are based on simulations and their experimental confirmation is still pending. Unfortunately it is difficult to reach the required parameters, i.e. low N fraction in the incoming flux, rather high fluences and preferably low particle energies, in ion beam experiments.

An open question remains the mechanism for the N loss when the N concentration in a depth of a few nanometer exceeds 50 %. The experiments showed a good agreement to SDTrimSP, where excess N is simply removed (see section 4.1.1). In a more physical picture N cannot simply disappear. Instead, above a N concentration of 50 % it is thermodynamically unfavorable to include more N in the tungsten matrix. The excess N diffuses towards the surface and potentially through the tungsten nitride towards the bulk. At the surface it may recombine to either N$_2$ or NH$_3$. However, the N atoms may also get bound in the unsaturated region before reaching the surface (see Fig. 4.10) from where they may then be eroded by physical sputtering.

# Chapter 5

# Nitrogen transport and retention in ASDEX Upgrade

This chapter summarizes the results from the AUG experiments described in section 3.2 and compares them to WallDYN-DIVIMP simulations (as described in the sections on WallDYN (3.3.3), DIVIMP (3.3.4) and the plasma backgrounds (3.3.5)). This comparison on the one hand supports the interpretation of the experimental results, on the other hand serves for benchmarking WallDYN.

The first section reports the experimental results on N deposition and re-erosion on the samples exposed on the divertor manipulator (DIM) to AUG divertor plasmas. Hereafter, the experimental observations are compared to WallDYN and SDTrimSP simulations. In section 5.2 the impact of N retention and release from the walls on the N distribution in the plasma is studied by means of spectroscopic measurements. An overview of sample exposures and spectroscopic measurements can be found in Fig. 5.8. The measurements from the AUG residual gas analysis and their implications are discussed in section 5.3. In section 5.4 a WallDYN simulation of the long term evolution of the N retention in AUG is compared to results from Ref. [9]. Finally measurements and simulations of the tungsten erosion in the outer divertor are presented in section 5.5.

## 5.1   Nitrogen retention in tungsten exposed to the AUG divertor plasma

### 5.1.1   Experimental results

This section presents the measurements of the N accumulation on the samples exposed on the DIM to the AUG discharges. An overview over the performed discharges is given in table 5.1 (see also section 3.2.2).

| | Discharge # | N puff | Sample Exposure |
|---|---|---|---|
| Day 1 | 29695 | X | Reference sample |
| | 29696 | ✓ | N accumulation |
| | 29697 | ✓ | N Re-erosion |
| | 29698 | X | |
| Day 2 | 29730 | ✓ | N accumulation (repeat 29696) |
| | 29731 | ✓ | Fluence dependence |
| | 29732 | ✓ | |

**Table 5.1:** *For this work 5 samples were exposed in 7 AUG discharges. The experiments are described in more detail in section 3.2.*

The N areal densities measured on the samples are shown in Fig. 5.1. As expected, the N content of the samples exposed to N-seeded discharges is larger than for the sample exposed only to the non-seeded discharge #29695. However, the sample exposed to #29696 has a notably larger N content than the sample exposed to the nominally identical discharge #29730. The N content from the sample exposed to two N-seeded discharges, #29731 & #29732, is located between the samples exposed to #29730 or #29696. The N profile in the poloidal direction is rather flat for all samples. The N content of the samples exposed to N-seeded discharges increases slightly towards the strike line.

The N inventory of the sample exposed to the N-seeded discharge #29697 and the non-seeded discharge #29698 is smaller than after exposure to N-seeded discharges only. It is slightly above the inventory of the sample exposed to the non-seeded discharge #29695. The purpose of this discharge combination was to analyze the re-erosion of the previously implanted N.

There are several possible reasons for the differences in the N content of the samples exposed to the nominally identical discharges #29696 and #29730: The most likely cause is a difference in the background impurity content of #29696 and #29730. Spectroscopic measurements (Fig. 5.8) show that the N fluxes in #29696 were larger than in #29730. A complicating feature is that a different impurity content in the plasma can lead to different plasma conditions. Especially the electron temperature at the outer strike line was observed to decrease with increasing N plasma content. A change in the electron temperature can modify the N deposition by changing the N ionization pattern, the temperature gradient force, re-erosion, implantation energy or implantation angle.

Another observation that may be linked to the variation in the N content is the larger boron deposition found on the sample exposed to #29696 compared to the sample exposed to #29730 (see Fig. 5.5b). This indicates that co-deposition of N with boron could have increased the N retention. The boron deposition is discussed in more detail at the end of this section. Finally, the difference is in a range where
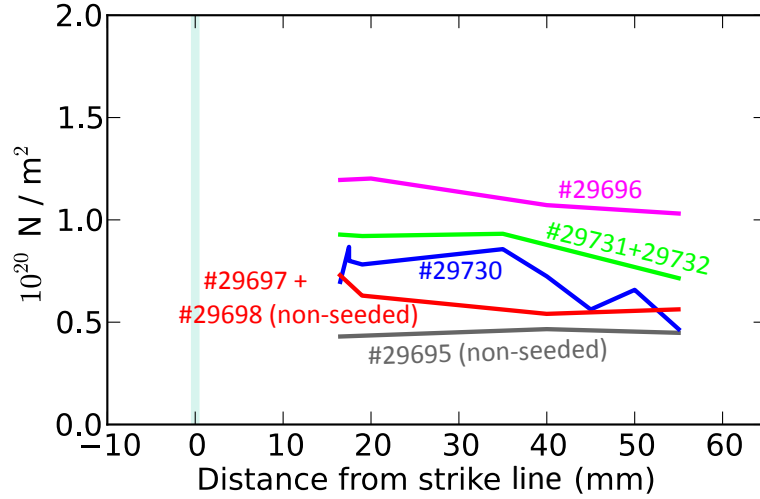
**Figure 5.1:** *N areal density measured on the samples exposed in the Divertor Manipulator to AUG plasmas. There is a small variation of the N content as function of the poloidal position. The discharges are described in section 3.2.2.*

also the contribution from N adsorbed on the sample surface could play a role. The temperature dependence of the N retention described in section 4.1.3 is unlikely to play a role. According to an estimate based on the heat equation the surface temperature during the exposure remained below 420 K. Although the lack of a definite explanation is not fully satisfactory, one has to conclude that the variation observed between #29696 and #29730 indicates the limit of accuracy which could be reached in the present experiments.

## Fluence dependence

A fundamental question in the study of the N retention is whether the N content saturates as found in the laboratory experiments or depends on the accumulated fluence. The particle flux (and therefore the accumulated fluence) decreases with increasing distance from the strike line. In the present exposures the accumulated fluence decreases roughly by a factor of five over the sample length. Nevertheless, the N content of the samples exposed to the N-seeded plasmas only shows a decline of about 20 %. This decline is much smaller than the variation in the fluence. Furthermore, the accompanying variation in plasma temperature and density may have caused this variation. That means the poloidal variation of the N content gives no indication for a fluence dependence.

A dedicated experiment to test the fluence dependence was the exposure of a sample to two N-seeded discharges, #29731 and #29732. This sample accumulated twice the fluence of the samples exposed to one N-seeded discharge with nominally identical plasma parameters. The resulting N content of this sample is somewhat larger

than the content of the sample exposed to the preceding discharge #29730. Still, the N content of the sample exposed to #29696 is even larger. This indicates that the variation is rather caused by changes in the background plasma, as discussed above. It should also be mentioned that according to SDTrimSP simulations (section 4.2 and Ref. [16]) the saturation N areal density can drop with an increasing N fraction in the incoming flux[a]. According to these results, the fluence is most likely an insignificant parameter under the given conditions. The N content apparently reaches a steady state, where it is limited by effusion and/or re-erosion, within one discharge. The areal density in the saturated state depends on parameters like the composition of the incoming flux, which cannot be determined with a sufficient accuracy in a tokamak experiment.

## Impact of surface roughness on the nitrogen retention

The N saturation areal density in the W surfaces of AUG has been estimated in Ref. [9] to $10^{21}$ N/m$^2$. This number is one order of magnitude larger than the areal densities found in laboratory experiments on smooth samples and SDTrimSP simulations (see Ref. [10] and sections 4.1 and 4.2). One possible explanation for this discrepancy is that the N areal density of $10^{21}$ N/m$^2$ refers to the macroscopic surface area, simply calculated from the sample size, and not to actual microscopic surface area. Both areas are identical for the polished surfaces used in the laboratory experiments. However, the first wall surfaces of AUG have a considerable roughness. Therefore the (microscopic) surface area is larger than the macroscopic surface area. Assuming that the (microscopic) saturation areal density is limited by chemical processes, a higher (macroscopic) saturation N areal density should emerge[b] [9].

The surface roughness of the samples exposed in the DIM (Fig. 5.2) is identical to that of the other AUG first wall surfaces and much larger than in the laboratory experiments. As just discussed, the N content of these samples seems to be saturated. Nevertheless, the N areal density[c] on the exposed, rough sample is in the range of $10^{20}$ N/m$^2$, the value expected for smooth surfaces and implemented in the WallDYN model. This indicates that the N ions can only reach parts of the surface not shadowed by a protruding surface structure [25] and the N retention in rough surfaces is not increased over smooth surfaces.

In the following these results will be compared to WallDYN simulations. This helps to gain a better understanding of the N retention process and the transport of N in the plasma.

---

[a]According to the simulations there is a maximum for about 5–10 % N in the incoming flux. According to the WallDYN simulations the N fraction in the DIM region should be about 5 %.

[b]The implantation depth is much shorter than the length scale of the roughness (in the $\mu$m range).

[c]All areal densities shown in this work refer to the macroscopic surface area.

## 5.1.2 WallDYN simulation of nitrogen deposition in the outer divertor

Figure 5.2 compares the measured N deposition to several WallDYN simulations. The dashed curves in dark red and dark green are simulations of one N-seeded discharge. The dark red curve is based on the SOLPS plasma backgrounds. Thereby, as described in section 3.3.5, the simulation switches between the high $T_e$ background and the low $T_e$ background, which includes the effects of N seeding. Unfortunately, the measurements and reconstruction of the plasma parameters is not accurate enough to include the subtle changes in the plasma parameters, which seem to cause the discrepancy between #29696 and #29730. The dark green curve is based on the 'simple' OSM plasma background created by imposing the boundary conditions from the low $T_e$ SOLPS solution. The yellow curve is again based on the SOLPS solutions but represents the predicted N deposition on the sample exposed to #29731 & #29732.
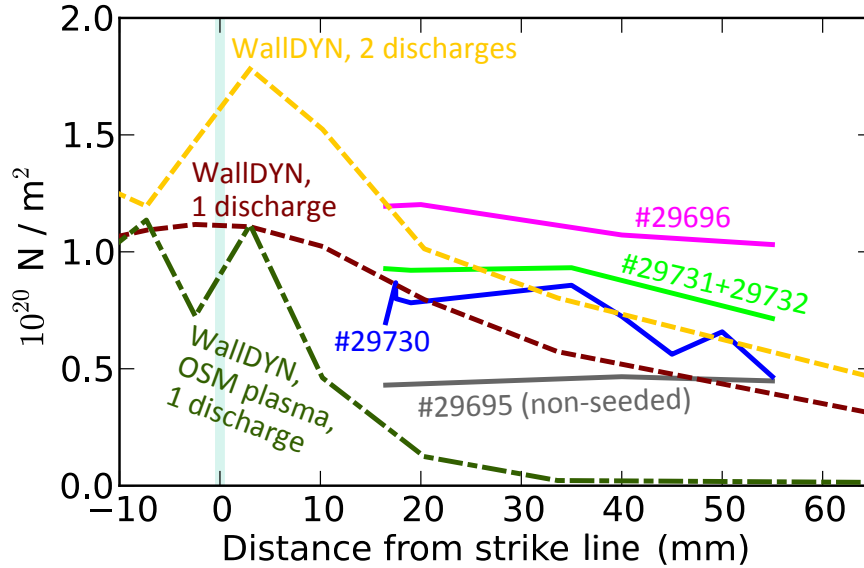


**Figure 5.2:** *N content of samples exposed to AUG divertor plasmas (solid lines) together with WallDYN simulations based on the SOLPS (dashed lines) and OSM plasma backgrounds (dash-dotted).*

The dark red curve is somewhat below, but in the range of N areal densities measured on the samples exposed to #29696 and #29730. Also the spatial dependence shows a decline of the N content away from the strike line, consistent with the experimental observations. In contrast, the N content predicted by the WallDYN simulation based on the OSM background (dark green curve) is significantly too low.

In the DIM region the WallDYN simulation corresponding to two discharges (yellow curve in Fig. 5.2) shows only a little increase in the N content in comparison to

the red curve. This is in agreement with the experimental finding that the steady state N content is established within one discharge. The decline of the simulated N content away from the strike line persists with the increased fluence. This shows that also in the simulation a steady state is reached within one discharge. Thereby the equilibrium N content depends on the fraction of N in the incoming flux. This fraction decreases with increasing distance from the strike line. Therefore, close to the strike line the N content is limited by saturation, while a few centimeters away the re-erosion of N by D limits the N areal density in the simulation.

### 5.1.3 Impact of flows and divertor conditions on N migration

The preceding section demonstrated that the SOLPS based WallDYN simulations give a good agreement to the N deposition in N-seeded discharges. It remains to be discussed what causes the discrepancy of the OSM based WallDYN simulation and to identify the processes governing the N deposition in the outer divertor.

It is well known that the flow of the main ion species has a strong impact on the impurity transport (see section 2.5). The 'simple' OSM solution (green curve Fig. 5.2) features a strong flow to the inner divertor on the high field side (Fig. D.4). However, the flow on the low field side is mainly directed to the outer target, in contradiction to the experimental measurements. Furthermore, the OSM flow pattern in the region of the magnetic X-point is strongly different from the flows predicted by SOLPS.

The difference in the flow pattern between the SOLPS plasma backgrounds and the 'simple' OSM background is a possible reason for the difference in the simulated N deposition. To study the role of the flows in the N migration, WallDYN simulation based on another OSM plasma background were performed. This plasma background is also based on boundary conditions from the low $T_e$ SOLPS simulation, but the ion flow pattern was manually modified to have flows to the inner divertor in the SOL and stagnant flows around the X-point. (Fig. D.5).

The N deposition in the divertor region predicted by a WallDYN simulation employing a re-distribution matrix based on this plasma background (light blue curve) is shown in Fig. 5.3. One can see that the modified flow pattern does not notably change the N deposition in the outer divertor and the simulated deposition is still too small.

Another possible reason for the deficiency of the simulations based on the OSM backgrounds is the plasma temperature in the outer divertor (see appendix D). In the OSM backgrounds the temperature is almost constant along most of the separatrix and only drops directly in front of the divertor target. In the SOLPS solutions the plasma notably cools down already between the X-point and the target.
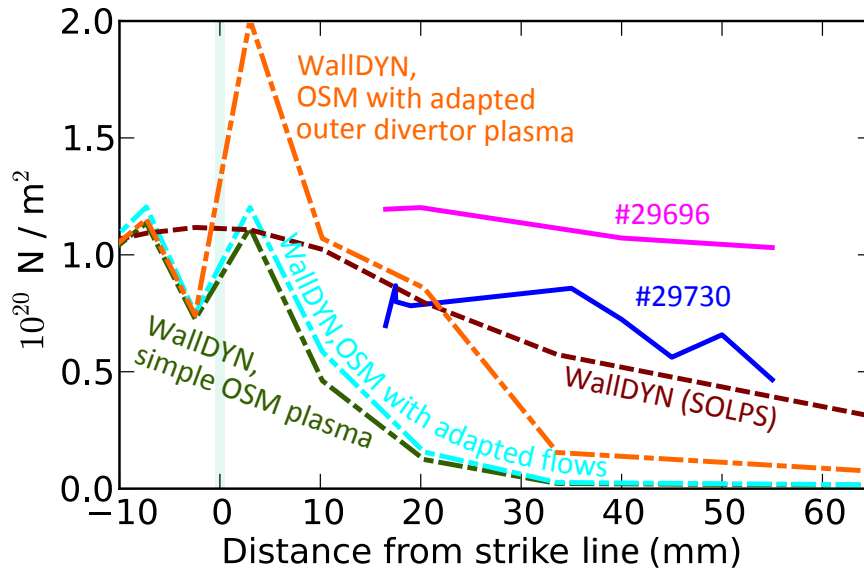
**Figure 5.3:** *N content of samples exposed to one N-seeded AUG plasma (solid lines) together with WallDYN simulations based on SOLPS (dashed line) and OSM plasmas (dash-dotted). The cyan curve is based on the plasma background with the manually imposed flow pattern. For the plasma background of the orange curve also the plasma temperature in the outer divertor was modified.*

The plasma temperature controls the temperature gradient force acting on the ions and is especially important for the ionization pattern. Actually, the spatial ionization patterns in the outer divertor calculated with the SOLPS background and with the OSM background are different. To test the influence of the plasma temperature in the outer divertor, the OSM plasma background was modified to achieve an earlier temperature drop in the outer divertor.

The N deposition pattern calculated with this background plasma is shown in Fig. 5.3. The modification obviously has the desired effect, the N deposition extends further away from the strike line. The remaining discrepancy does not affect this conclusion, as the OSM plasma is closer but not yet identical to the SOLPS solution. This result is consistent with WallDYN simulations applying either the high or the low $T_e$ SOLPS background: Simulations based on the low $T_e$ background give the same result as the simulation based on both SOLPS background. In simulations based solely on the high $T_e$ plasma, the N content drops faster with increasing distance from the strike line, similar to the OSM based simulation. This confirms the finding that high temperatures in the divertor volume lead to a more localized N deposition.

## 5.1.4   Re-erosion of retained nitrogen

So far WallDYN simulations of the N deposition have been discussed. Figure 5.4 shows the N areal density profile of the sample exposed to the N-seeded discharge #29697 and the non-seeded discharge #29698, and a WallDYN simulation of N re-erosion in a non-seeded discharge.
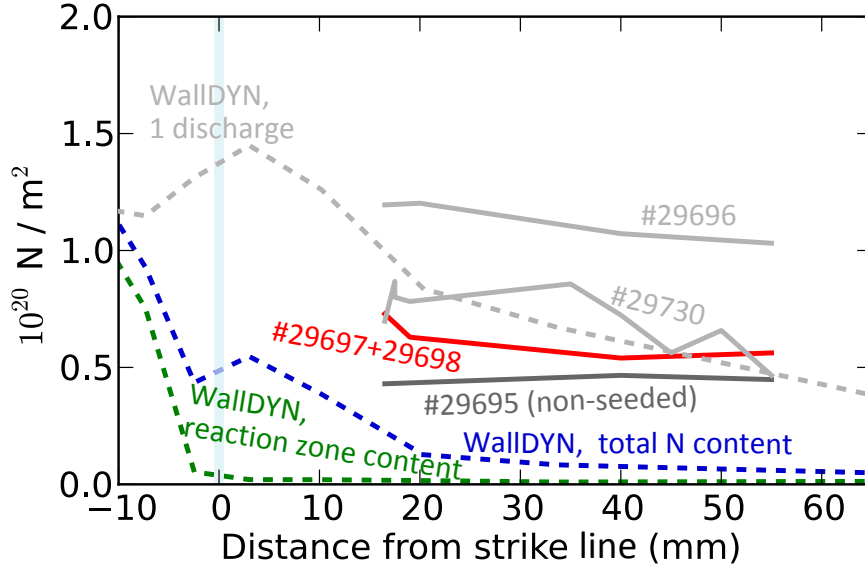


**Figure 5.4:** *The red line is the N content of the sample exposed to the N-seeded discharge #29697 and the non-seeded discharge #29698. The N inventory of some further samples is shown (gray lines) for reference. The dashed lines are results from a WallDYN simulation and discussed in the text.*

The initial wall composition state for the re-erosion simulation was generated by simulating two subsequent N-seeded discharges (#29696 and #29697) and setting the N content of the divertor manipulator region to zero in between. Then this initial wall condition (the gray dashed curve in Fig. 5.4) was used for a WallDYN simulation without N puff and based on the high $T_e$ (non-seeded) plasma background. In the initial wall configuration not the complete N content is stored in the reaction zone, but N has also been transported into the bulk-zone. As discussed in section 3.3.3 this may cause problems because N from this zone cannot be re-eroded. For this reason two results from the simulation are given: The blue curve, where N in the bulk zone is included, and the green curve, where only the N content of the reaction zone is shown. The green curve indicates a very low N content in the divertor manipulator region, that means essentially all N has been eroded from the reaction zone. The blue curve is somewhat higher and shows residual N, which cannot be eroded.

In comparison to the measurements the simulated areal density is too low. One possible explanation for this discrepancy is an overestimation of the N erosion by the WallDYN surface model. According to SDTrimSP, the implanted N largely

resides (due to recoil implantation, see section 4.2) in a few nanometer depth and the tungsten matrix must be eroded to remove the N from this depth (see sections 4.1.2 and 4.2). In contrast, the WallDYN model assumes a homogeneous distribution of N within the uppermost 4 nanometers and therefore overestimates the erosion rate. This topic is further discussed in section 5.1.5 on the basis of the N implantation in discharge #29695. Also the surface morphology of the rough samples could reduce the erosion rate below the value predicted by WallDYN. Spectroscopic measurements performed during #29698 are in line with this conclusion and can be found in Fig. 5.14. Nevertheless, the discrepancy could also be caused by a N source which is not included in the simulation. Such a source would increase the N flux to the wall and reduce the net erosion of N.

## 5.1.5 SDTrimSP analysis of N retention in #29695 and boron deposition

Figure 5.5a gives a comparison of the measured N deposition and a WallDYN simulation of the non-seeded discharge #29695. The simulation is based on the SOLPS background corresponding to the non-seeded plasma with a N puff rate which was a factor of 10 smaller than in the N-seeded simulations. This puff rate is a lower limit on the N fluxes in #29695, estimated from spectroscopic measurements in the outer divertor (Fig. 5.8) and residual gas analysis (Fig. 5.19).

In the experimental measurement the N content of the sample exposed to the non-seeded discharge (black curve in Fig. 5.5a) is at most a factor of two below the N content of the samples exposed to the N-seeded discharges. In contrast, the N content in the corresponding simulation (gray dashed in Fig. 5.5a) is about a factor of ten lower than for the N-seeded simulation and does not match the experimental result.

Additionally to N, also boron has been deposited on the exposed samples. Boron is introduced into AUG by boronizations to improve the plasma performance and was included in the WallDYN simulations via the initial wall configuration (see section 3.3.3). The boron deposition is of interest here as it can offer additional information on the impurity migration and because co-deposition of N with boron could increase the N retention.

The areal densities from the evaluation of the boron peak observed in the NRA spectra[d] are shown in Fig. 5.5b and range from $0.2 \cdot 10^{20}$ to $1.2 \cdot 10^{20}$ B/m$^2$. This is in the range of the measured N areal densities and could be sufficient to modify the N deposition. The similar areal densities of N and boron reflect their similar abundances in the plasma, with a typical boron content of 1 % [149]. The boron content of the samples exposed on the second day is somewhat lower than on the

---

[d]Some of the boron peaks (Fig. 3.7) only consist of a few counts, so that a notable statistical uncertainty emerges especially for low boron contents.
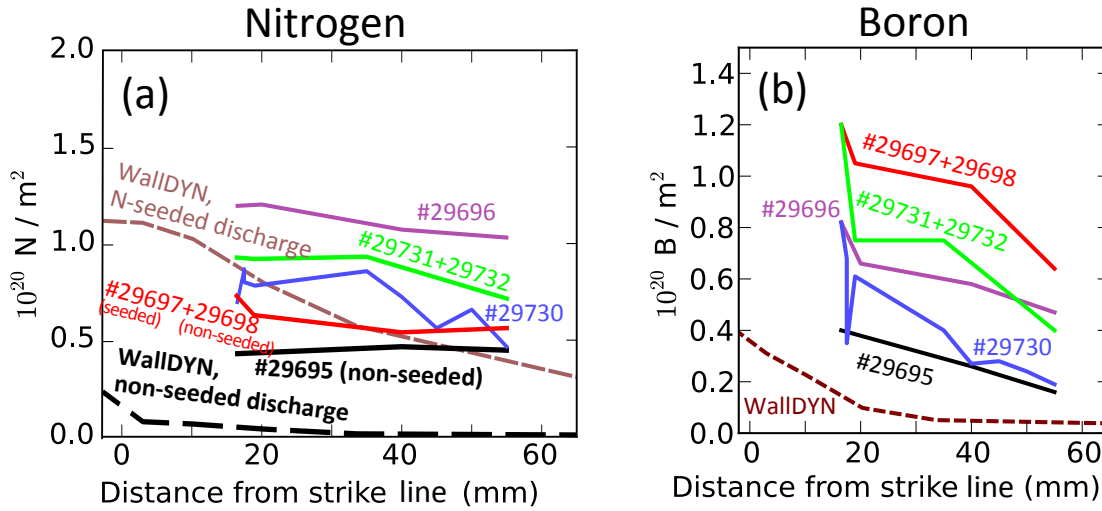
**Figure 5.5:** *The outer divertor deposition of N in the non-seeded discharge #29695 (black line in (a) ) and the boron deposition of all samples (b) are underestimated by WallDYN (dashed lines). The boron deposition pattern indicates a fluence dependence.*

samples exposed on the first day, probably because the boron was eroded by the discharges performed in between. The boron deposition in the non-seeded discharge #29695 is lower than in the further discharges, so probably N increases the erosion of boron and thus the boron flux to the DIM sample.

Figure 5.5b also shows the boron areal densities from a WallDYN simulation representing a N-seeded discharge. The simulated boron deposition is below $0.1 \cdot 10^{20}$ B/m$^2$ and therefore too low. The presented results show that the boron deposition in all discharges and the N deposition in the non-seeded discharge #29695 are underestimated by WallDYN. A closer analysis indicates that in both cases the boron or N content in the simulations has already reached a dynamic equilibrium, where the implantation is balanced by the erosion and the areal densities do not increase anymore with fluence. This is in contrast to the experimental results for boron: The boron content increases towards the strike line and the boron content from the samples exposed to two subsequent discharges is about a factor of two larger than in the samples exposed to one discharge. This strongly indicates that the boron content in the experiment is approximately proportional to the fluence.

One obvious reason which could cause this discrepancy are underestimations of the N and boron sources. The N source is a manually applied puff, whose strength had to be estimated for the non-seeded discharge. Figure 5.8 shows that the spectroscopic signals in #29695 and the end of #29696 vary by a factor of 3–10. The N puff used to model the background N content, being a factor of 10 smaller than for the N-seeded discharges, is on the lower limit of this range. Nevertheless, the observed discrepancy appears rather too large to be explained by the uncertainty in the background flux. The source flux might also be underestimated for boron, which is introduced into the simulations via the initial wall configuration. An analysis of the boron transport

in the simulations indicates that an increase of the initial boron content in the outer divertor target, especially at the poloidal position of the DIM, would increase the boron influx. This, however, is in contrast to the findings that the outer divertor usually is a zone of net erosion [129, 7], where one would not expect large amounts of boron several weeks after a boronization.
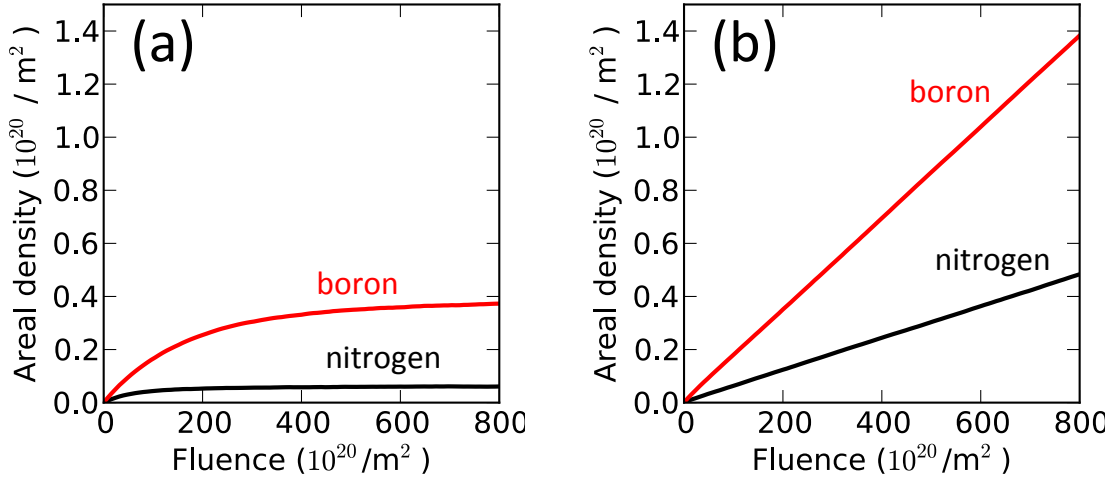


**Figure 5.6:** *N and boron accumulation in tungsten under D-B-N-W bombardment from SDTrimSP simulations. The particle fluxes are based on a non-seeded WallDYN simulation. For the simulation with 10 nm tick layers (a) re-erosion leads to low steady state areal densities. In the simulation with a good depth resolution (b), N and boron deposition rise to higher values.*

Another possible reason for the discrepancy is an overestimation of the re-erosion by WallDYN. This could be due to the surface roughness of the employed samples or the negligence of depth profile effects in WallDYN. As already discussed in section 3.3.3 and indicated by the results from section 4.2 the depth distribution of light elements in a tungsten matrix may play an important role. As the wall model of WallDYN does not take into account the depth distribution of the elements, such effects are not included and could cause errors in the simulation. This hypothesis has been tested by performing SDTrimSP simulations. The impact angle for all species was 60° and the ion fluxes are based on the WallDYN/SOLPS simulations:

- $0.1 \cdot 10^{20}$ W/m$^2$/s (100 eV)

- $0.5 \cdot 10^{20}$ N/m$^2$/s (100 eV)

- $1 \cdot 10^{20}$ B/m$^2$/s (100 eV)

- $100 \cdot 10^{20}$ D/m$^2$/s (50 eV)

Here one has to keep in mind that the ion fluxes are subject to a significant uncertainty because the WallDYN simulations also depend on the input for the N

91
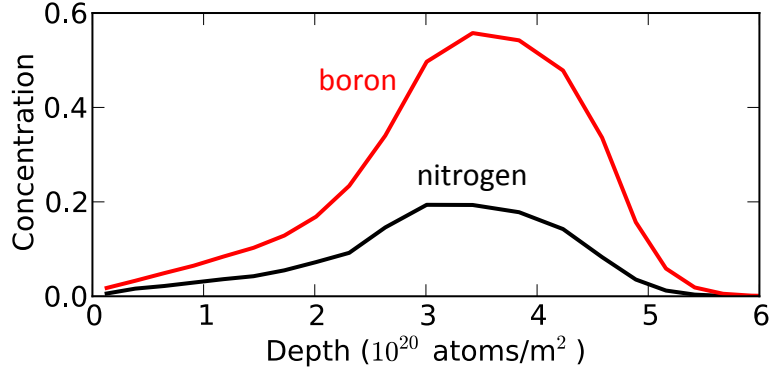
**Figure 5.7:** *Depth profile of N and boron after D-B-N-W bombardment with a total (mainly D) fluence of $800 \cdot 10^{20}$ $m^{-2}$. The concentration of boron and N directly at the surface are much smaller than in a depth of $3$–$4 \cdot 10^{20}$ m$^{-2}$ ($4$–$5$ nm).*

source and the manually specified boron wall coverage. Also the influence of surface morphology or sputtering by other residual impurities like carbon are not included.

The results of the simulations are shown in Fig. 5.6. First a SDTrimSP simulation with a very coarse depth resolution of 10 nm was performed. According to Fig. 5.6a this simulation behaves similar to the WallDYN simulations, that means the areal densities saturate on a rather low level. Figure 5.6b shows a SDTrimSP simulation with a layer thickness of 0.4 nm, giving a good depth resolution. With this depth resolution the result is very different: The areal densities rise linearly with the fluence and reach much higher levels, comparable to the ones found in the measurements.

As can be seen in Fig. 5.7, in the simulation with a good depth resolution the N and boron profiles peak in a depth of 4–5 nm. This peak stores a notable amount of material while it does not increase the sputter erosion because only material from the uppermost nanometer is sputtered (Fig. 2.7). In models with a coarse depth resolution the material is more homogeneously distributed, the concentration in the uppermost nanometer is higher and the resulting erosion is overestimated. This finding is consistent with the previous discussion of N re-erosion. So a possible reason for the discrepancy between measurements and simulations in Fig. 5.5 are depth profile effects. Nevertheless, it cannot be exclude that also the surface roughness or an underestimation of the source terms contribute to the discrepancy.

To investigate the impact of N co-deposition with boron, a simulation without boron influx was carried out. According to this simulation the N retention is initially the same. However, for larger fluences (about $1.5 \cdot 10^{23}$ N/m$^2$), the N content saturates without boron co-bombardment but increases unlimited under co-bombardment with boron due to the formation of N/B co-deposited layers.

## 5.2 Nitrogen fluxes and distribution in the plasma from spectroscopic measurements

Ex situ analysis of the samples exposed to AUG plasmas allows to measure the retention of N in tungsten. However, this method is restricted to one position and integrates over complete discharges, so that the the interpretation of the measurements is challenging. Spectroscopic measurements offer complementary information with good temporal and some spatial resolution. For the interpretation of the spectroscopic measurements one should note that large parts of the divertor plasma have an electron temperature above 5 eV (Fig. D.1). In these regions the low ionization states of N observed by divertor spectroscopy only exist transiently before they are further ionized (see Fig. 2.8). Thus these measurements are rather sensitive to the influx of atoms from the walls (see left part of Fig. E.1) than to the total density of N ions.
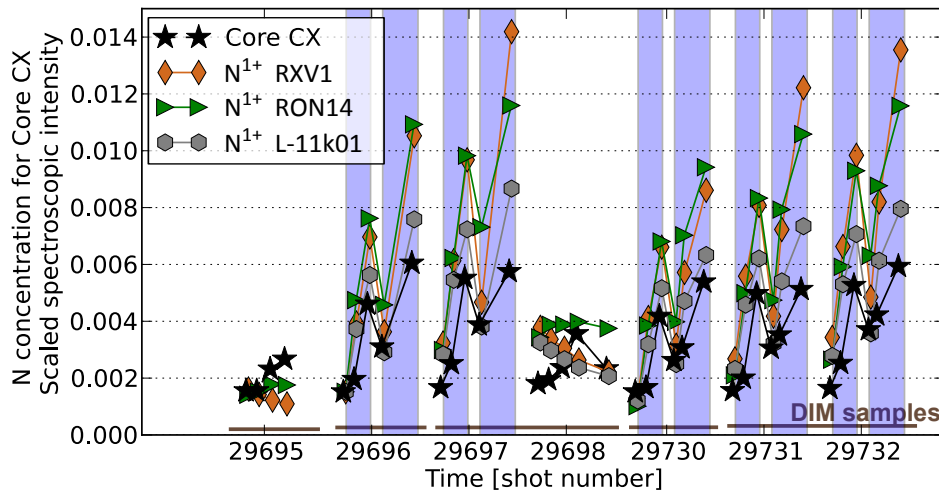


**Figure 5.8:** *Overview of spectroscopic N measurements recorded in the discharges performed for this work. Core CX measures the absolute N concentration in the core plasma. The measurements from passive spectroscopy were scaled to match the core N concentration in the beginning of #29696. The lines of sight in the divertor are shown in Fig. 3.12. The N content rises during the $N_2$ puff (indicated by the blue background) and latency increases the long-term N content after the puffs.*

Figure 5.8 shows an overview of some spectroscopic measurements from the various discharges discussed in this work. The black stars are measurements of the N concentration in the core plasma from charge exchange spectroscopy. This measurement is discussed in more detail in section 5.2.2. The other curves shown in this figure represent photon emission from singly ionized N. Their intensities were scaled to match the measured core N concentration in the beginning of #29696, to be able to compare their time evolution in the same graph. From the charge exchange spectroscopy only a limited number of measurements is available and for the plot also

the measurements from the passive spectroscopy were restricted to these times. As discussed in section 3.3.3, the photon emissivity depends on the plasma parameters which partly change during the discharges. Figure 5.8 shows only measurements from lines of sight which seem to be unaffected by the changing plasma conditions. The positions of the divertor spectroscopic lines of sight used for this work are shown in Fig. 3.12.

The initial discharge #29695 without N-seeding exhibits a N background resulting in a core concentration of about 0.2 %. During the N-seeded phases the core N concentration rises to 0.4–0.6 %. The core N concentration at the beginning of each discharge is 0.15 to 0.2 %. In the measurements later in the discharges one can observe the history effect as the N concentration rises in consecutive N-seeded discharges.

The measurements from passive spectroscopy behave similar to the core N concentration. Nevertheless, the variation in the amplitude is different for different spectroscopic lines of sight. The gray curve from a line of sight looking at limiter structures of the low field side wall behaves rather similar to the core N concentration. In contrast, the variation of the green curve, which measures emission from the outer divertor, and the yellow curve, which measures horizontally across the whole divertor region, vary stronger than the core concentration. Assuming that the observed variation is due to a change in the N density and not caused by changes of the emission per ion or the charge state distribution, this means that the N density along these lines of sight may rise stronger than in the core plasma. Different from the core concentration measurements, the passive spectroscopy indicates that the N content is already increased in the beginning of #29697, #29698, #29731 and #29732. This shows that a N inventory is built up during the N-seeded discharges and part of this N is released in
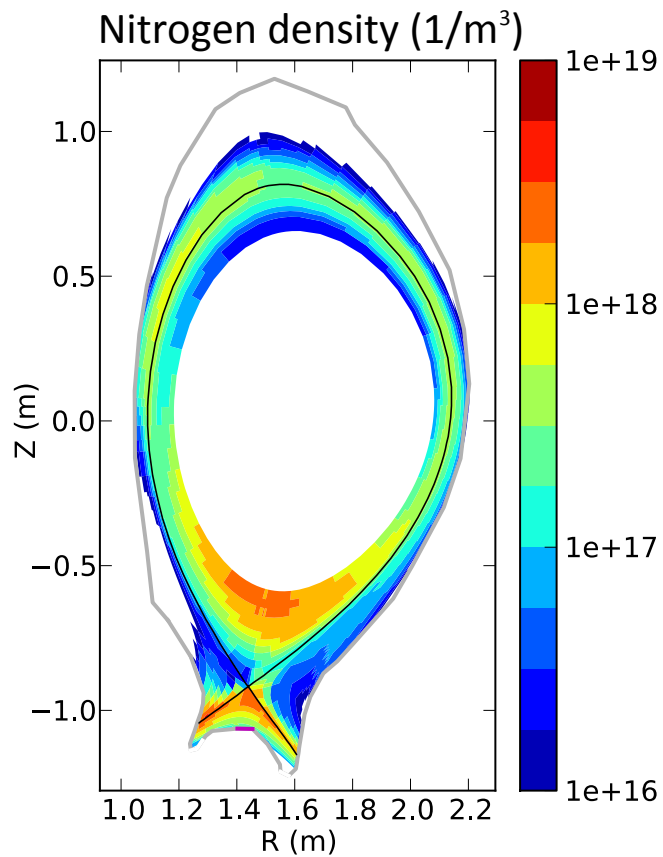


**Figure 5.9:** *N density in a N-seeded discharge at 3.7 s calculated with DIVIMP-WallDYN. The corresponding electron density is given in Fig. D.2. The poloidal variation in the core plasma may be an artifact caused by the combination of a background including classical drifts with DIVIMP simulations, which do not include such effects.*

ventory is built up during the N-seeded discharges and part of this N is released in

subsequent discharges. N re-erosion in discharge #29698 is discussed on the basis of Fig. 5.14.

## 5.2.1 Passive spectroscopy measurements

In this section the emission from low ionized charge states, measured by passive spectroscopy, will be discussed in more detail and compared to WallDYN simulations. For this comparison the charge state resolved N density is calculated on the basis of the WallDYN and DIVMP simulations. From these densities the spectroscopic intensities are derived via the synthetic spectroscopy described in section 3.3.3. The charge state integrated N density calculated with WallDYN during the N-seeded phase at 3.7 s is shown for reference in Fig. 5.9.

### Time evolution

The spectroscopic measurements have a good temporal resolution. This should allow to compare the simulated time evolution of the N fluxes to the spectroscopic measurements. As discussed in the following, this comparison is hampered by two problems: The shape of the experimental N puff is unknown and the transition from the high $T_e$ divertor plasma regime to the fluctuating state with reduced plasma temperature (see section 3.2.2) disturbs the spectroscopic measurements.
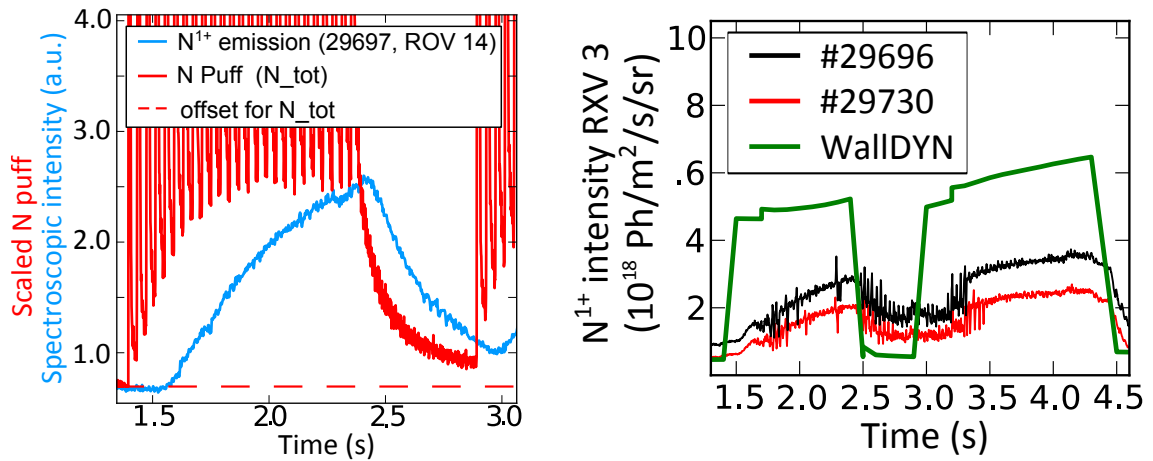


**Figure 5.10:** *Time evolution of $N^{1+}$ emission in N-seeded discharges. The left figure indicates that the observed time evolution is related to the shape of the $N_2$ puff. The simulated N emission for a line of sight crossing the divertor rises much faster than observed in the experiment (right figure).*

The valve used for the $N_2$-puff is located remote from the plasma and connected to outlets in the divertor roof baffle via a 3 m long tube (see section 3.2.2). Figure

5.10a shows a pressure measurement (red curve) next to the valve at the beginning of the tube and the time evolution of $N^{1+}$ emission in the outer upper divertor region (blue curve). The modulation of the puff, visible in the pressure measurement, was required to reach low seeding rates. One can see that the pressure during the phases where the valve is closed rises over about 0.5 s. This means that the N content in the tube, and thereby the effective puff rate, needs at least 0.5 s to reach the steady state value. A comparison of the pressure measurement with the spectroscopic signal shows that, due to the transport time in the tube, the rise of the N density in the plasma is delayed. Furthermore, the emission rises on a similar timescale as the $N_2$ puff rate and also both quantities decay on a similar timescale. The observed rise and decay times of the N content are therefore strongly influenced by the puff shape.

Figure 5.10b shows a spectroscopic measurement from a line of sight which goes horizontally through the divertor region (the lines of sight are shown in Fig. 3.12) together with the corresponding curve from the synthetic spectroscopy in WallDYN (see section 3.3.3). One can see that the simulated curve rises steeply with the onset of the N puff at 1.4 and 2.9 s. As just discussed, the measured intensity only rises with a delay. It would of course be possible to adapt the puff in the simulation to match the measured time evolution. However, it is not the primary aim of this work to perfectly fit the experimental measurements, but to benchmark the simulation for a given input. The pressure measurement presented in Fig. 5.10a cannot be directly used as input, because the 3 m tube between the pressure gauge and the plasma will further modify the puff shape.

The oscillations visible in Fig. 5.10b indicate the second challenge in the interpretation of the spectroscopic measurements: The N seeding induces the transition to another divertor plasma regime with lower plasma temperatures and oscillations between the high and low $T_e$ state. The most obvious effect of these transitions are jumps in the spectroscopic intensities, especially for lines of sights close to the X-point but also at the outer strike line (see Fig. 5.14).

The spectroscopic measurements are difficult to interpret in this case, because the effect of the changes in the plasma parameters on the spectroscopic measurements is twofold. First, the changing plasma parameters can modify the spatial ionization pattern and thereby the N distribution. Second, the photon emission per ion depends on the plasma parameters. The rather large amplitude of the oscillations in Fig. 5.10b indicates that the spectroscopic measurements are strongly modified by the transition from the high to the low $T_e$ mode. Because two plasma backgrounds, one for the high and one for the low $T_e$ phase, are employed (see section 3.3.5), this modification should be included in the simulations. The transition between the two plasma backgrounds is indicated by the steps in the simulated intensities. However, only a part of the jumps in the spectroscopic signals are reproduced in the simulations, while others are not.

It is therefore not clear whether the discrepancies between simulated and measured intensities are due to shortcomings in the plasma background or in the WallDYN-

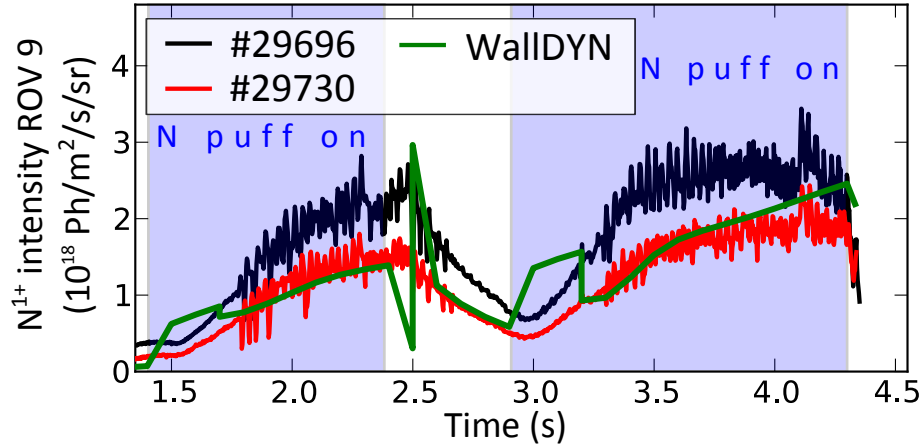DIVIMP physics model, like the negligence of the $N_2$ dissociation chain.



**Figure 5.11:** *Comparison of measured and simulated $N^{1+}$ emission in the outer divertor line of sight ROV 9.*

The situation is somewhat better for the lines of sight (e.g. ROV 9 in Fig. 5.11) viewing the region of the divertor manipulator. In this region the SOLPS plasma background should reproduce the plasma reasonably well and the plasma parameters seem to change rather little between high and low $T_e$ state. In this region also the time evolution matches nicely as shown in Fig. 5.11. This may seem to be in contradiction to the foregoing statement that the time evolution of the N content is dominated by the unknown time evolution of the $N_2$ puff. However, the line of sight used for Fig. 5.11 is close to the outer strike line, where the N fluxes mostly vary due to N accumulation in the surface. The good match between the spectroscopic measurements and the WallDYN simulations shows that the simulation correctly reproduces the evolution of the N surface content.

**Spatial variation of nitrogen line emission**

In general the absolute agreement between measured and simulated spectroscopic intensities from $N^{1+}$ and $N^{2+}$ ions is reasonable. This can be seen in Fig. 5.12b–d which shows a comparison between simulated and measured intensities for a large number of lines of sight and various wavelengths. The x-axis is the angle in degree between the line of sight and the horizontal direction as indicated in Fig. 3.12. The best agreement between measurements and simulation is found in the outer divertor. The camera equipped with a filter for emission from singly ionized N exhibits, in agreement with the simulations, a pretty homogeneous emission from the divertor region (not shown in this work). This result is encouraging because the SOLPS plasma background, which is a large source of uncertainty in other regions, should give a good reproduction of the plasma parameters in the outer divertor.

The agreement between measurements and simulation is not as good for emission from neutral N atoms, shown in Fig. 5.12a. The obtained intensities are about a
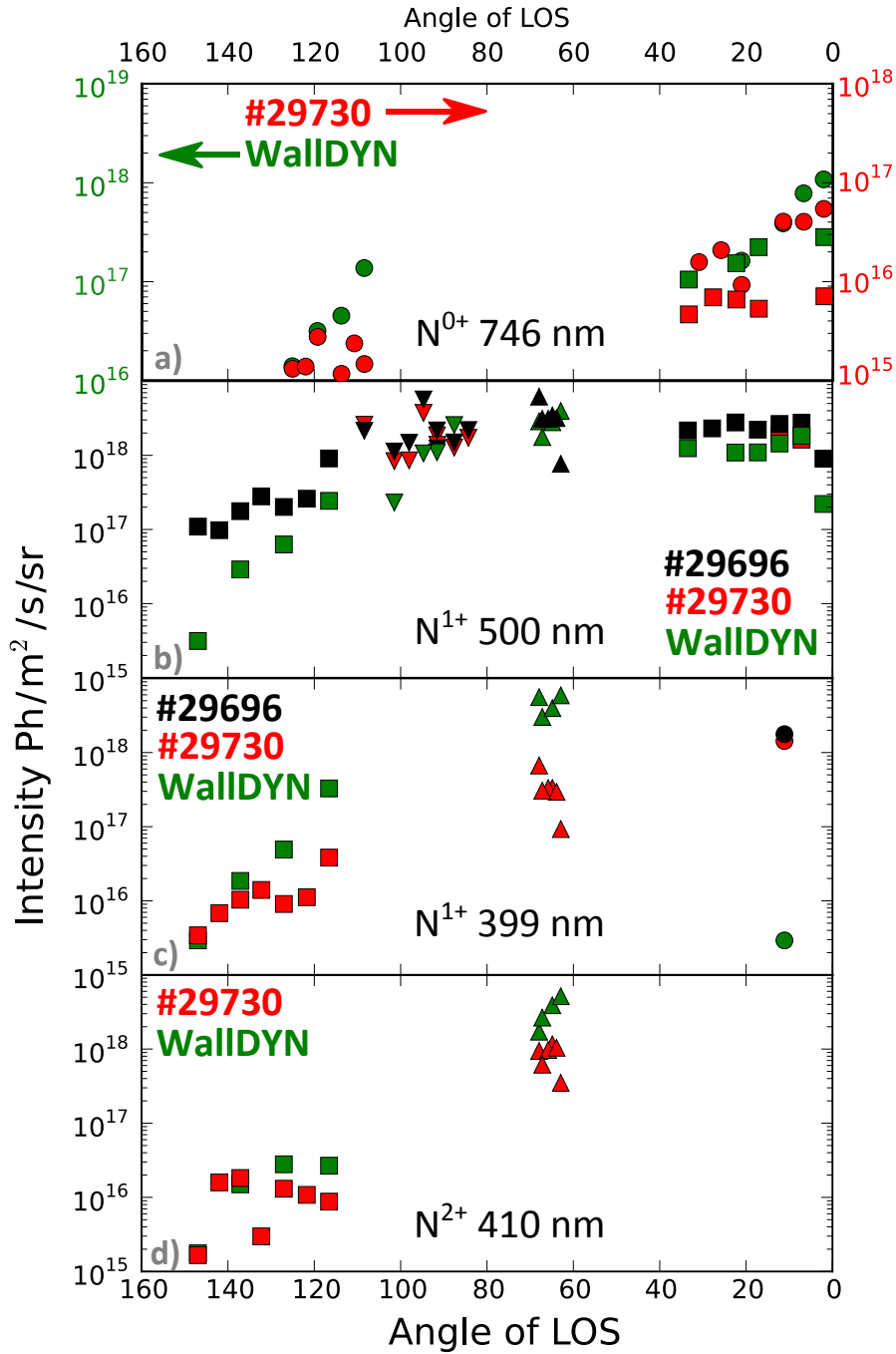
**Figure 5.12:** *Comparison of measurements from passive divertor spectroscopy to synthetic data from a WallDYN simulation during the second N seeded phase at 3.75 s. The x-axis is the angle between the line of sight and the horizontal direction (see Fig. 3.12). The symbols indicate different lines of sight: ■ are ROV and RIV lines of sight, ● RON and RIN lines of sight, ▲ DOT lines of sight and ▼ ZIV and ZON lines of sight. The color distinguishes between experimental and simulated values. Figure part (a) for neutral N emission employs different y-axis for experiment and simulation and the calibration for these lines of sight is associated with a large uncertainty (see section 3.2.4). The circle in the lower right in the 399 nm graph is the line of sight RON 14 (DVL) which lies below strike line, see section 5.5. In general there is a good agreement between simulated and measured intensities.*

factor of ten below the simulated values. To allow a relative comparison the y-axis for the experimental measurements was scaled by a factor of ten with respect to the simulation. One possible reason is the uncertain calibration for the wavelength region around 747 nm. For the low field side lines of sight (0–40°) the calibration is based on an extrapolation from lower wavelengths. For the low field side lines of sight (around 120°) no calibration for the individual lines of sight is available, so only an average calibration factor was applied. Another possible reason for the discrepancy between simulated and measured intensity is that $N^{1+}$ ions may be generated directly from $N_2^{z+}$ or $NH_y^{x+}$ molecules, without the appearance of neutral N atoms. The relative comparison of different lines of sight shows that the simulated intensities have a more pronounced spatial dependence than the the measured intensities. A reasonable agreement in the spatial distribution of the radiation from neutral N is visible from Fig. 5.13, which shows a picture from the camera equipped with the filter for 747 nm wavelength and the simulated photon emission. One can see that the emission from neutral N, which reflects the N influx (see Fig. E), is very localized.
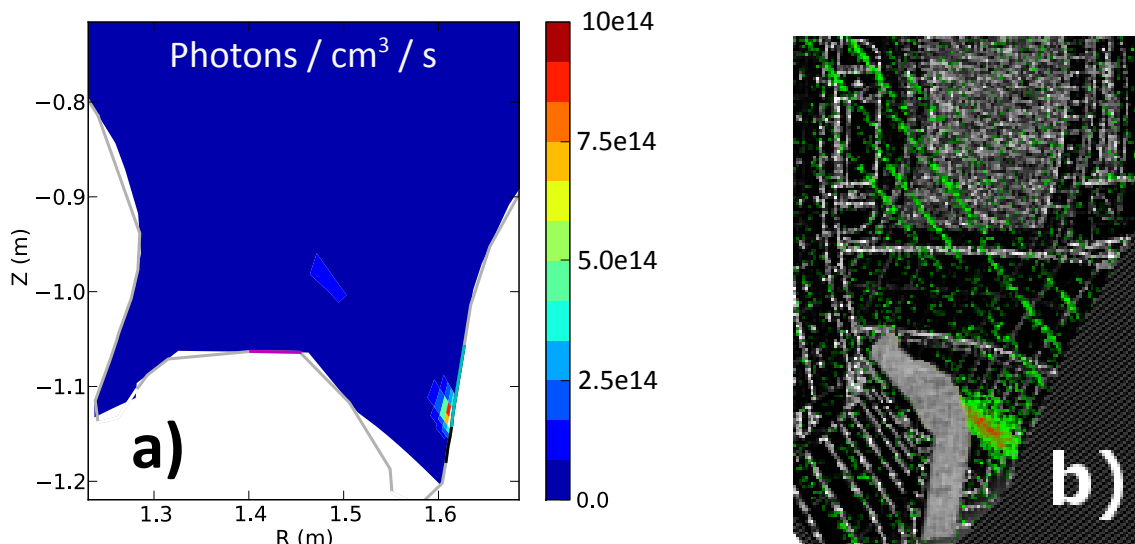


**Figure 5.13:** *Emission from neutral N atoms (747 nm) at 3.7 s calculated with the synthetic spectroscopy of WallDYN (a) and measured with a filtered camera (b). The inner divertor region in the camera image is corrupted by deuterium radiation. An image from this camera without filter can be found in Fig. 3.9a.*

**Re-erosion of retained nitrogen**

Figure 5.14 shows the time evolution of a spectroscopic line of sight viewing the outer strike line. For the N seeded discharges #29696 (gray curve) and #29697 (blue curve) one can see that there is a large variation between the low and high $T_e$ divertor plasma states. For this line of sight the WallDYN simulation (light green curve) qualitatively reproduces the change caused by the plasma variation, for

example the measured and simulated intensity in the intermediate phase without N puff is larger than in the phases with puff.

Figure 5.14 also includes a measurement from the non-seeded discharge #29698 (red curve), which shows a slow decrease of the $N^+$ emission. Here it has to be mentioned that also during the non-seeded discharge #29698 the plasma conditions change slightly over the discharge, so that the measured intensity evolution not necessarily reflects the evolution of the N content. Discharge #29698 was performed to study the re-erosion of N retained from the previous two discharges, as described in section 5.1.4. The dark green curve is from the corresponding WallDYN simulation. In the beginning of the simulation (dashed region) the calculated intensity is very high: N is eroded from the surface but returns to its origin. However, the tile is saturated with N so that the N is not directly re-deposited but fully reflected. This causes large gross N fluxes. A comparison of the simulation (dark green curve) to the measurement (red curve) indicates, consistent with section 5.1.4, that the N erosion is overestimated by WallDYN. In the beginning the intensity from the simulation is too high. As N is depleted too fast from the walls the N intensity quickly decreases and the simulation drops below the measurement.
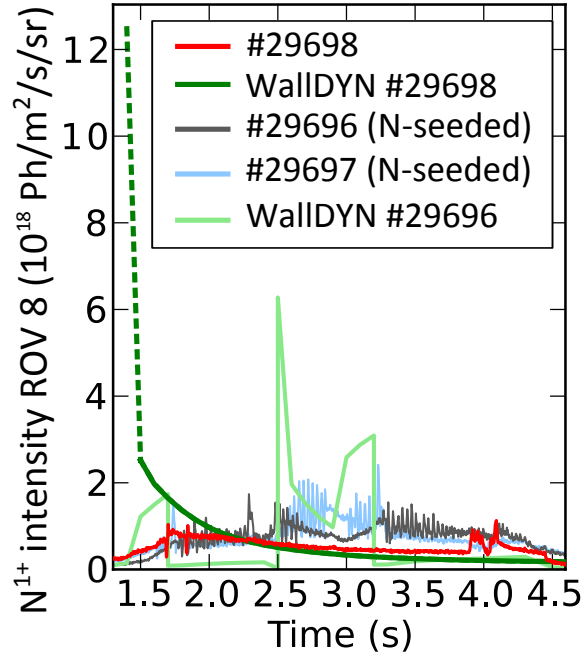


**Figure 5.14:** $N^{1+}$ *emission close to the outer strike line. Discharge #29698 shows how N is re-eroded from the walls. The emission in the N-seeded discharges is strongly affected by switch between high $T_e$ and low $T_e$ phases and the divertor plasma oscillations.*

## 5.2.2 Core nitrogen content

Radiation control by impurity seeding is currently the favored operation scenario to meet the material limits in a fusion reactor (see section 2.6). The applicability of this scenario depends on a low contamination of the core plasma with the seeded impurities, which would deteriorate the fusion performance. The concentration of N in the core plasma, measured by charge exchange recombination spectroscopy (see section 3.2.4), is shown in Fig. 5.15. The time resolution of the measurements is limited by the need to activate the neutral beam heating system for the measurement. Figure 5.15 also includes measurements from two lines of sight viewing the emission from singly ionized N, where the intensities were normalized to the charge exchange

spectroscopy concentration in the beginning of discharge #29696. The gray curve is from a line of sight going horizontally through the main plasma and viewing the limiter on the low field side main wall, where the N fluxes could be expected to be related to the core plasma concentration. The agreement to the time evolution of core N concentration is even better for the ZIV 1 line of sight, with a rather vertical view from the inner divertor to the high field side main wall (magenta curve, line of sight is shown in Fig. 3.12). This good agreement indicates that the core N concentration is related to the N fluxes in this high field side region. The long term evolution of the N concentration has already been discussed on the basis of Fig. 5.8.
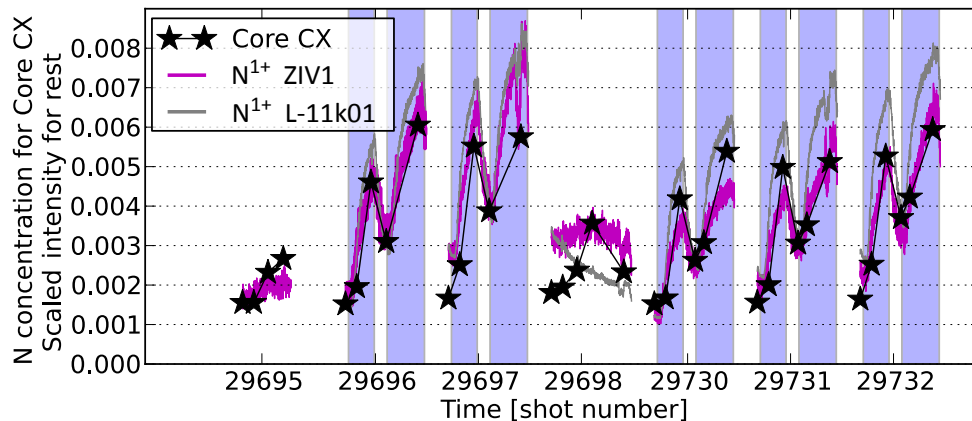


**Figure 5.15:** *The time evolution of the core N concentrations is reproduced by the $N^{1+}$ emission from the low field side main wall limiters (gray curve) and a line of sight looking from the inner divertor to the high field side main wall (violet curve).*

With WallDYN-DIVIMP the core impurity concentration can be calculated as follows: For each wall tile the "core averaged"[e] impurity density for a unit influx is taken from the DIVIMP simulations performed to generate the re-distribution matrix. These contributions for a given flux span a wide range because the probability for a particle to reach the core plasma varies strongly. It is low, less than 1 % according to the DIVIMP simulations, for particles originating from the strike line regions. For particles launched from the main wall the probability to reach the core is much higher, more than 50 %. With the actual impurity fluxes from the wall tiles calculated in WallDYN, the total impurity density can be calculated as superposition of the contributions from each wall tile. The distribution of the impurity source fluxes is just opposite to the core entry probabilities: They are large close to the strike lines and small on the main wall (see Fig. E.1). The impurity concentration

---

[e]In the DIVIMP simulations, which cover only the outer part of the core plasma, the N density depends on the poloidal and radial position as shown in Fig. 5.9. This is caused by the use of a SOLPS background including drifts. However, the DIVIMP model is not suited to resolve such effects and therefore averaging over the core region is expected to be appropriate. The charge-exchange spectroscopy measurements show that the N density is independent of the radial position. Available measurements also indicate a poloidally symmetric impurity distribution in the core region of L-mode plasmas [150].

is finally calculated in the trace approximation by dividing the impurity density by the electron density in the core plasma.
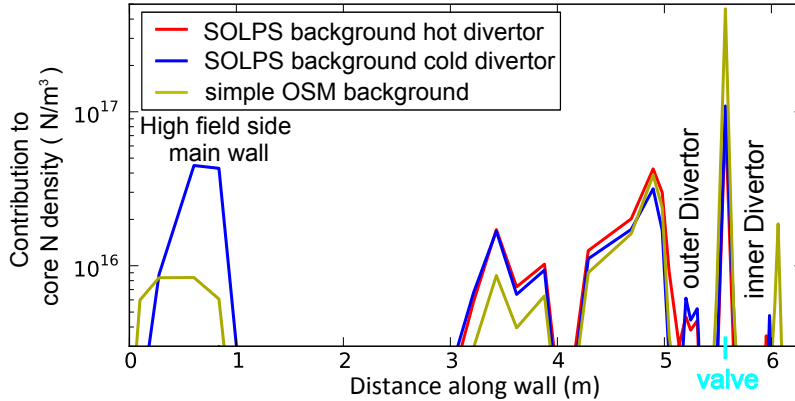


**Figure 5.16:** *Sources of N in the core plasma at 2.3 s (end of first N-seeding phase) from WallDYN simulations. The distance along the wall, used as x-axis, is shown in Fig. 3.18. The largest source is the N puff. For the low $T_e$ background (blue curve) also the high field side main wall gives a significant contribution to the core N density.*

Figure 5.16 shows the contribution of the different wall tiles to the core N content at 2.3 s (calculated with WallDYN assuming initially N free walls). The red and the blue curve were calculated with the high and the low $T_e$ SOLPS plasma background, respectively. The yellow curve is based on the 'simple' OSM plasma. The largest source for all simulations is the original N puff. This contribution is similar for both SOLPS based simulations and about a factor of four higher for the OSM plasma based simulation. The N fluxes from the outer divertor target plate are larger than the flux from the puff (see Fig. E.1). However, the probability to reach the core plasma from the outer divertor is very low so the outer divertor gives no significant contribution to the core N density.

A notable difference between the SOLPS based simulations arises in the contribution from the high field side wall. It is negligible for the SOLPS solution corresponding to the high $T_e$ state and much larger with the low $T_e$ SOLPS background. This difference is mostly caused by a larger transport of N to the high field, resulting in a larger N source flux at this location. These finding are in agreement with the interpretation of Fig. 5.15, because the ZIV 1 line of sight measures contributions from both main core N sources, the original puff and the high field side main wall.

Figure 5.17 shows the time dependence of the core N concentrations from the Wall-DYN simulations and the measurement from discharge #29730. The green curve is the standard SOLPS based WallDYN simulation. It switches between both SOLPS backgrounds according to the measured time dependence in the plasma parameters (see sections 3.2.2 and 3.3.5). The core concentration in the N-seeded phases calculated with this simulation is about a factor of two above the measured values. The yellow curve is from the WallDYN simulation based on the 'simple' OSM plasma. It exhibits an even higher N concentration, which is a factor 4 above the measured

values.

For the comparison one has to consider that the simulations treat the core transport in a simple manner: For example it employs a constant diffusion coefficient on the whole computational domain, only covers the outer part of the core plasma and neglects poloidal asymmetries. An absolute agreement within a factor of two seems therefore acceptable. The OSM based prediction is, as for the divertor deposition studies, notably worse than SOLPS based result.
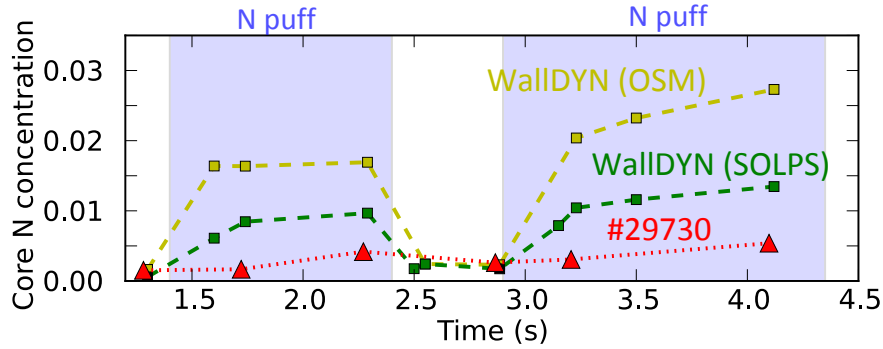


**Figure 5.17:** *N concentration in the core plasma measured in discharge #29730 (▲) and simulated with WallDYN-DIVIMP. The WallDYN simulations, especially the one based on the OSM plasma, overestimate the N concentration in the N-seeded phases.*

A notable difference is again visible in the time evolution of the N content. The simulation predicts an immediate rise of the core content when the N puff is switched on, while the measured concentration rises only slowly. The measured time evolution of the core N concentration is very similar to the time evolution of the passive spectroscopy (see Fig. 5.15). Therefore a determining factor for the time evolution of the core N concentration should be the $N_2$ puff shape, as discussed in section 5.2.1. Another possible contribution to the difference in the time evolution between measurement and simulation is the transport time. It is neglected in the simulation but could be of relevance for the dynamic evolution of the core concentration (see section 3.3.3). Both, transport time and puff shape, should lead to a slower rise and decay of the N content than predicted by the simulation.

### Impact of neutral energy, ion flows and temperature gradient force

Similar to the discussion of the outer divertor N content in section 5.1 two questions remain: What controls the core N content and what causes the discrepancy between the SOLPS plasma backgrounds and the OSM plasma background.

From Fig. 5.16 it is obvious that the transport of N from the puff region to the main plasma dominates the core N concentration in the OSM based simulation. The DIVIMP simulations show, that only 5 % of the N reaching the core from the puff location are ionized in the core plasma. That means that N enters the core

region mainly in the form of ions. Two important contributions to the movement of the ions are the background ion flow and the temperature gradient force (see section 2.5). Also the ionization location could still play a role in the transport of the impurities to the core plasma. To test the effect of these contribution some further WallDYN calculations have been performed.

The rate coefficient for the ionization $K_{iz}$ is essentially independent of the neutral velocity. Therefore, the ionization mean free path $\lambda_{iz} \propto \frac{v_{neutral}}{K_{iz}}$ increases with the initial velocity of the neutral $v_{neutral}$. The impact of the ionization pattern on the WallDYN simulations was therefore tested by varying the initial energy of the particles in DIVIMP. The cyan curve in Fig. 5.18 is based on DIVIMP calculations where the N atoms were launched with thermal velocities[f]. This simulation reproduces the absolute core concentrations better than the standard simulation (green curve, initial energy of atoms is a few eV as discussed in section 3.3.4). Because the $N_2$ puff is the main source for the core N content, this result indicates that the dissociation of the puffed $N_2$ molecules is better represented by thermal atoms than by energetic atoms (which could be generated in the dissociation process). This is in agreement with the finding of Ref. [57], that the dominant ionization path for $N_2$ is via ionization of the $N_2$ molecules and subsequent dissociative ionization.
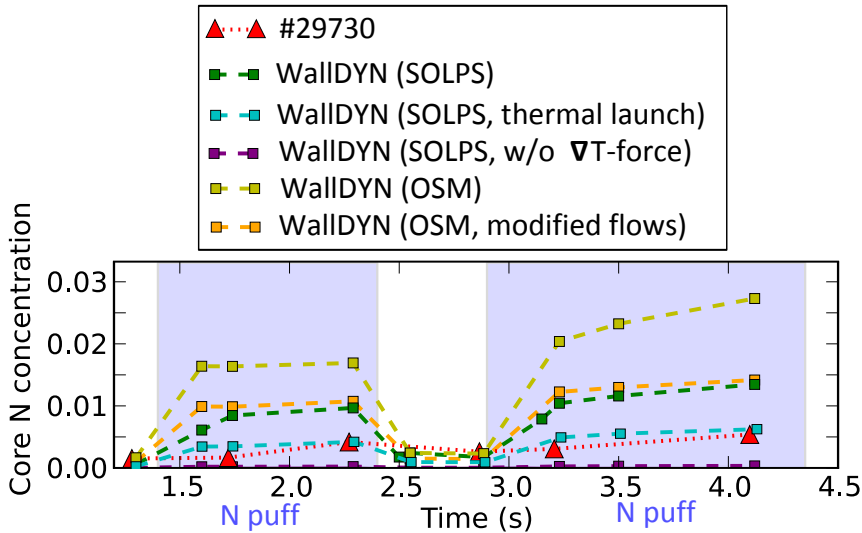


**Figure 5.18:** *Core N concentration calculated with different models. An adjustment of the X-point region flows in the OSM plasma reduces the predicted N concentration to the level of the SOLPS based simulation. Starting the atoms in the DIVIMP simulation (on the SOLPS backgrounds) with thermal velocity gives the best agreement with the experimental measurement. Without temperature gradient forces the predicted core concentration drops almost by a factor of 50.*

The violet curve in Fig. 5.18 shows a WallDYN simulation based on DIVIMP calculations with the temperature gradient force switched off. One can see that this strongly reduces the predicted core N concentration below the measured values.

---

[f]The DIVIMP parameter *ebd* controlling the initial energy was set to 0.03 eV

This confirms the importance of this term for the impurity transport out of the divertor region, into the main chamber SOL[g].

Finally, the orange curve in Fig. 5.18 is based on the OSM solution with the adapted background flow profile (Fig. D.5 and section 5.1.3). The resulting core N concentration is very similar to the one obtained with the SOLPS backgrounds and gives an acceptable match to the experimental result. Similar to the presented result with the SOLPS backgrounds, the core N content should drop further when the atoms in DIVIMP were launched with thermal velocity.

The reduction of the core concentration caused by the modified flow pattern around the X-point indicates that this flow pattern was the main reason for the deviation from the SOLPS based simulations. Altogether, this discussion shows that all three processes (ionization, temperature gradient force and background flows) play an important role for the impurity contamination of the core plasma.

## 5.3   Residual gas analysis and ammonia production

During each of the N-seeded discharges presented in this work about $7 \cdot 10^{20}$ N atoms have been puffed into the plasma. By residual gas analysis it is possible to estimate the number of N atoms that have been pumped by the vacuum system (see section 3.2.5). Figure 5.19 shows for the experiments performed for this work:

- The number of puffed N atoms (blue).

- The number of pumped N atoms based on mass spectrometer HPQO (red).

- The number of pumped N atoms based on mass spectrometer HPQI (green).

The number of pumped N atoms is calculated from the $N_2$ partial pressure, contributions to N pumping from other molecules are not included. Discharge #29673 had the same plasma parameters as #29695, but followed directly after a N-seeded discharge. The mass spectrometer HPQO failed during #29698. The numbers derived from HPQI and HPQO are pretty similar, apart from #29673 which was, however, not analyzed in more detail.

The most notable result from Fig. 5.19 is that the $N_2$ molecules recorded by the residual gas analysis only account for 2–3 % of the puffed N atoms. This percentage is essentially the same for all N-seeded discharges. The background level is indicated by the number of atoms pumped in #29695. In discharges following N-seeded

---

[g]Though the importance of this force is not surprising it is not yet included in all codes employed for migration simulations [57].
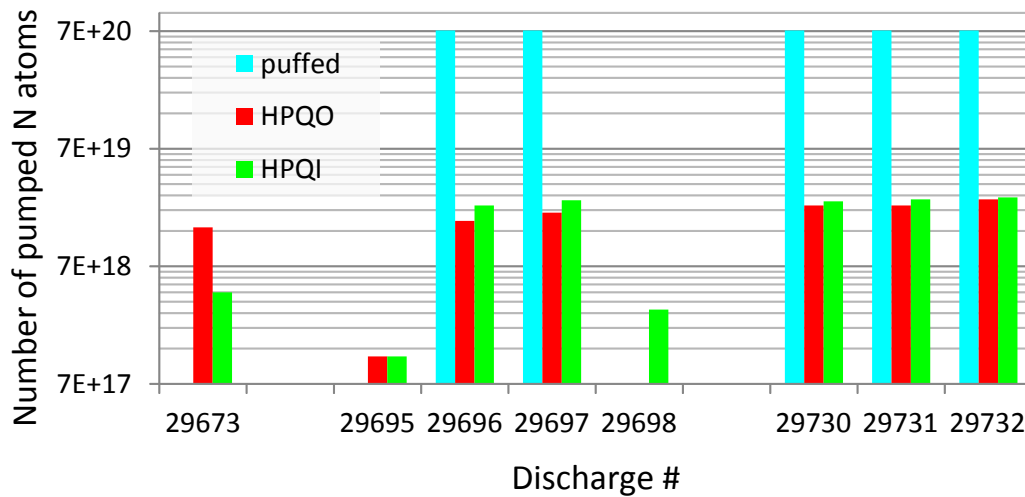
**Figure 5.19:** *Number of N atoms pumped in form of $N_2$ molecules according to the residual gas analysis of AUG. The numbers were calculated based on data from two mass spectrometers, HPQI and HPQO. Only a small fraction of the puffed atoms was recorded as pumped. Furthermore this fraction is essentially constant for all N-seeded discharges.*

discharges, like #29673 and #29698, the latency of the N release can be observed. Different from the spectroscopic measurements, the residual gas analysis indicates that the N content in #29730 was rather higher than in #29696.

The large difference between the number of puffed and pumped atoms can have three reasons: The retention of N in the vacuum vessel, the pumping of N in form of $NH_3$ or deficits in the calibration of the residual gas analysis (see appendix B).

The error introduced by the calibration can be estimated from discharge #29386. This discharge is the last one of a series with high density, high heating power and strong N-seeding. According to the evaluation of the residual gas analysis, 1/3 of the puffed atoms are pumped in the form of $N_2$ molecules. This would indicate that the calibration is wrong by a factor of three, assuming that the N storage capabilities of AUG are fully saturated and all puffed N atoms are pumped by the vacuum system. An even larger error in the calibration factors could be caused by a dependence on discharge specific parameters like partial pressures. Though the uncertainty in the calibration is quite large, it still seems to be too small to account for the large discrepancy between the number of puffed and pumped N atoms.

Another possible explanation for the discrepancy was the pumping of N in a form different from $N_2$. Here especially ammonia, $NH_3$, is a possible candidate. However, during the discharge the partial pressure of ammonia is much lower than the partial pressure of $N_2$. So, at least on a short timescale, the pumping of ammonia does not contribute to the pumping of N atoms. This points to a very strong retention of N in the vacuum vessel, notably larger than the 30 % found in Ref. [72]. From a physical point of view this could indicate a larger amount of retained N for the present conditions with lower N-seeding level, lower density and lower heating power
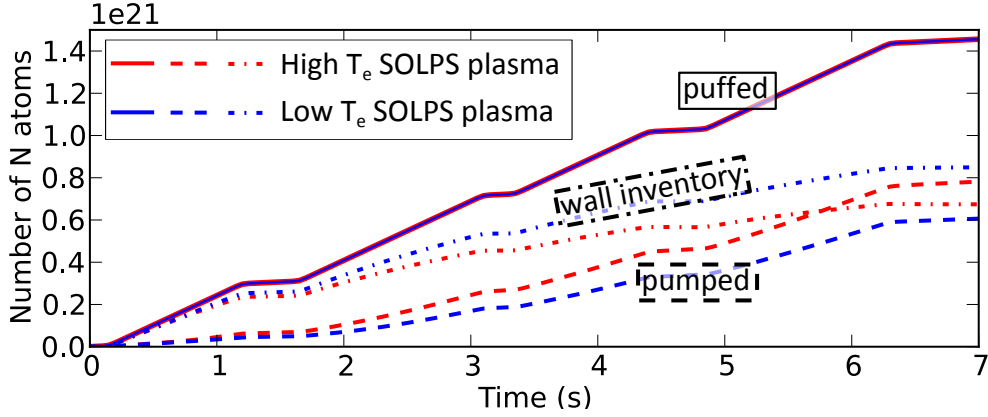
**Figure 5.20:** *Number of N atoms puffed (solid lines), retained in the walls (dash-dotted lines) and pumped by the vacuum system (dashed lines) from WallDYN simulations based on the SOLPS plasma backgrounds. Because only the flattop plasma phase is simulated in WallDYN, one discharge corresponds to 3.2 s.*

compared to Ref. [72].

Also the WallDYN simulations include a model for the pumping of N by the vacuum system (see section 3.3.3). Figure 5.20 shows the number of puffed, pumped and retained N atoms from WallDYN simulations. These simulations, one based on the high and one on the low $T_e$ plasma background (section 3.3.5), cover two subsequent discharges. According to these simulations 1/4 to 1/3 of the puffed N atoms should be pumped within the initial discharge. This number is much higher than the value of 2–3 % determined by the residual gas analysis. In the simulation corresponding to the non-seeded discharge #29698 (not shown here), $3 \cdot 10^{19}$ N atoms have been removed from the walls and were recorded as 'pumped'. This amount is again much larger than the N accounted for by the residual gas analysis in this discharges.

Besides the discrepancy in the absolute amount of pumped particles also the fluence dependence of the N retention differs between simulation and experiment. In the simulations the number of pumped atoms increases notably from the first to the second discharge, where more than 50 % of the puffed N atoms are pumped. In contrast, the number of pumped molecules is essentially constant in the experiment. This result makes the explanation of the observed discrepancies by an error in the calibration factor less likely, as the relative amounts should be independent of the calibration.

A possible explanation for both, the absolute discrepancy and the different fluence dependence is an additional, large reservoir for the N storage. Assuming that the retention of N caused by implantation and nitride formation in the walls is correctly described in WallDYN (as indicated by the results presented in sections 5.1 and 5.4), another storage mechanism must create an additional reservoir for N. The formation and retention of ammonia molecules is a candidate for such a mechanism (see section 2.7).
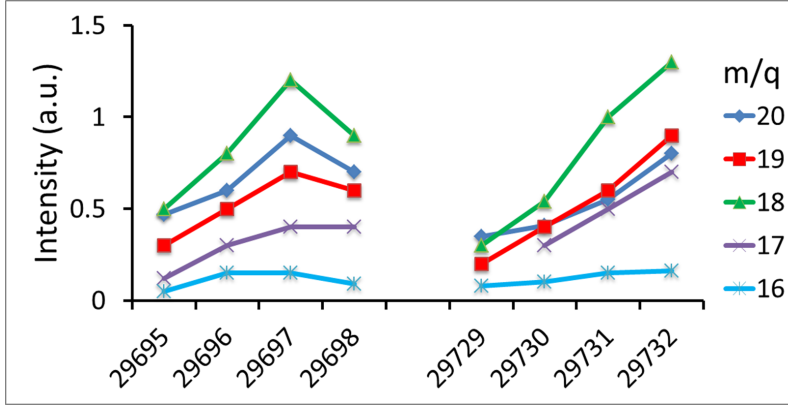
**Figure 5.21:** *The intensities at m/q values associated to (deuterated) ammonia measured with HPQI about 100 s after the discharge rise after N-seeded discharges.*

The amount of ammonia adsorbed on a surface is expected to be at most one atomic layer [72]. The resulting N areal density would therefore be lower than the areal density from N implantation and nitride formation. However, implantation only takes place on plasma wetted surfaces, so that the contributing area is limited. In contrast, ammonia can adsorb on all surfaces of the vacuum vessel, so that the available surface area may be larger than the plasma wetted area by more than a factor of ten. Ammonia desorbs only slowly at ambient temperatures, so the ammonia could only be pumped by the vacuum system on a timescale of hours or days [111].

Unfortunately, the direct measurement of ammonia molecules is difficult in AUG. AUG is operated almost exclusively with D as main species. This causes an overlap of the main (fully deuterated) ammonia peak, $ND_3$ at $m/Z = 20$, with the main peaks from fully deuterated water $D_2O$ and fully deuterated methane $CD_4$. This makes the measurement of ammonia very challenging [111]. Nonetheless, the signals from $m/Z = 17$ ($NH_3$) to $m/Z = 20$ ($ND_3$) can give an indication of the ammonia production and are shown together with m/q=16 (baseline corresponding to $CH_4$ and O) in Fig. 5.21. Assuming that the production of water and methane is similar in the N-seeded discharges and the non-seeded discharge #29695, the ammonia partial pressure rises with the number of N-seeded discharges, thus supporting the assumption of $NH_3$ as a large N storage reservoir.

## 5.4 Long term nitrogen retention

In section 5.1 it has been shown that the N content in samples with a surface comparable to that of AUG tiles is not higher than expected from laboratory experiments on smooth samples. This raises the question on what causes the discrepancy in the N saturation areal densities observed in laboratory experiments and those deduced previously from the feedback model for N seeding in AUG [62]. To study this

question, a simulation of the long term N retention in AUG was performed. This simulation used the N-seeded plasma background and a constant puff of $8.6 \cdot 10^{20}$ N/s, comparable to the one used in Fig. 7 of Ref. [62].

The N saturation areal density in AUG has been deduced in Ref. [62] from a model developed to feedback control N-seeding in AUG. The storage and release of N from the walls modifies the N content in the plasma and had to be included in the model. For this model the plasma wetted area in AUG was estimated to 3.5 m$^2$, less than 10 % of the actual geometric surfaces, because most of them receive only a small particle flux from the plasma. A value of $1 \cdot 10^{21}$ N/m$^2$ for the saturation areal density was determined by fitting the measured temporal behavior of the nitrogen flux. However, the model measures rather the storage capacity of AUG, $3.5 \cdot 10^{21}$ N atoms, than the saturation areal density.
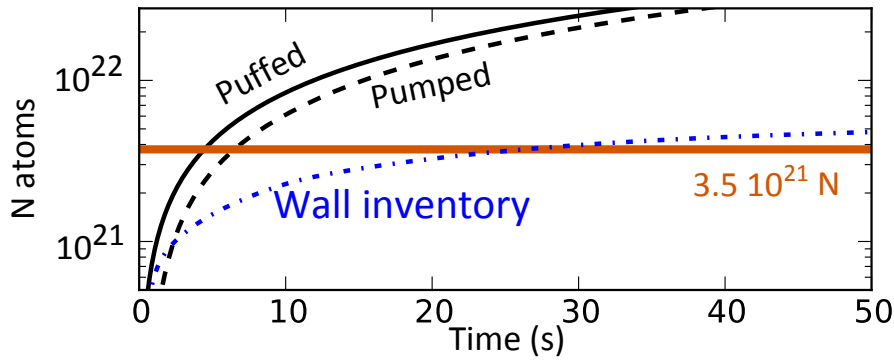


**Figure 5.22:** *WallDYN simulation on the long term N retention in AUG: Number of puffed N atoms (solid line), pumped atoms (dashed) and wall content (dash-dotted). The orange line represents the long term retention derived for AUG in Ref. [62].*

The amount of N retained in the simulation is given in Fig. 5.22 (blue curve) and saturates at about $5 \cdot 10^{21}$ N atoms. This is comparable to the $3.5 \cdot 10^{21}$ N atoms derived from experimental measurements in Ref. [62], although the numbers are based on very different models: The value of $3.5 \cdot 10^{21}$ N atoms is the product of an areal density of $1 \cdot 10^{21}$ N/m$^2$ with the estimated plasma wetted area of 3.5 m$^2$. In contrast, the N content in WallDYN saturates at an areal density of about $1 \cdot 10^{20}$ N/m$^2$ and the 'plasma wetted surface' is not manually specified but is a result from the DIVIMP calculations.

Still, it is not only necessary to match the retained number of atoms but the saturation actually has to be reached within a reasonable time. A look at the simulated time evolution confirms that also this is the case. A wall inventory of $3.5 \cdot 10^{21}$ N atoms is reached in about 25 s, corresponding roughly to 4–5 discharges. Also another comparison to Fig. 7 of Ref. [62] shows that for $2 \cdot 10^{21}$ puffed N atoms the wall content is similar in WallDYN ($1 \cdot 10^{21}$ N atoms) and the feedback model ($1.4 \cdot 10^{21}$ N atoms).

Figure 5.23 shows the simulated N concentration in the wall at 15 s. To store $1.4 \cdot 10^{21}$ N atoms with a maximum areal density of $10^{20}$ N/m$^2$, parts of the main wall must contain N. The transport of N to the main wall is connected to some uncertainty because it involves transport of ions perpendicular to the magnetic field. In the presented simulation a perpendicular diffusion coefficient of $D_\perp = 0.5$ m$^2$s$^{-1}$ has been used. This should be a rather conservative estimate. For instance, the diffusion coefficient in the underlying SOLPS solutions varies between



**Figure 5.23:** *N wall inventory at $t=15$ s for puff of $8.6 \cdot 10^{20}$ N/s. The asymmetric wall area reaches roughly from 3.4 to 4.9 m.*

0.5 m$^2$s$^{-1}$ close to the separatrix and 1 m$^2$s$^{-1}$ in the far scrape-off layer. In a WallDYN simulation based on a diffusion coefficient $D_\perp = 1$ m$^2$s$^{-1}$, the wall inventory builds up somewhat faster. Another source of uncertainty is the toroidal asymmetry of the low field side main wall in AUG (Fig. 3.9a), which is not included in the WallDYN model. On the one hand the asymmetry should lead to an increased flux to the protruding structures. On the other hand the fluxes to the recessed surface areas are strongly suppressed, so that the available area is reduced. A lower limit of the retained N can still be calculated by assuming that the asymmetric low field side part of the wall does not contribute to the N retention at all. According to Fig. 5.23 this would reduce the inventory by about 30 %, resulting in a prediction of $3.3 \cdot 10^{21}$ N atoms. This value agrees, even better than the previous one, to Ref. [62].

The agreement found for the long term N retention in this section might appear to conflict with the disagreement found in the previous section for the number of pumped N atoms. This indicates that one has to decide between two types of N retention:

- N retention in the vacuum vessel: Here N adsorbed (in form of ammonia) to the walls may play an important role and explain the low amounts of N pumped by the vacuum system. However, the adsorbed ammonia only desorbs slowly and has a low probability to return through the pumping slits to the main volume with the plasma.

- N retention in and on the plasma facing materials: This is probably dominated by N implanted into the walls, because this storage can host larger amounts than adsorption. N re-eroded from the plasma facing components directly enters the plasma and increases the N content in the plasma.

Of course the existing uncertainties, e.g. the strong toroidal asymmetry of the low field side main chamber, transport of N perpendicular to the magnetic field and the possible contribution of ammonia to the N retention, do not allow to give a precise

number but only a rough estimate. Still the agreement of our simulations with the measurements presented in this work and in Ref. [62] indicate that the saturation of the N retention in AUG can be reasonably described by the WallDYN model. The apparent contradiction between AUG and laboratory measurements reported in Ref. [62] seems to be caused by the underestimation of the area contributing to N retention.

The N implanted into the tungsten surfaces of AUG seems to be stable over a long time. The N content in the sample exposed to #29696 was measured a second time after storing it for half a year under rough vacuum conditions. The N content had not changed during this time, confirming the long term stability of the formed tungsten nitride known from the laboratory experiments. In the future, this may allow to better discriminate between long term N retention by implantation and formation of tungsten nitride and transient retention by ammonia formation.

It is noteworthy, that the number of N atoms in the plasma is in the lower $10^{19}$ range. This number is negligible in the present considerations and demonstrates the importance of the wall inventory. Hence, the saturation of the N wall inventory has a strong effect on the N fluxes into the plasma. According to the WallDYN simulation, the increased reflection of N from the saturated walls increases the number of N atoms entering the plasma for a given puff source by almost a factor of ten.

## 5.5   Tungsten erosion

In this section I want to consider the erosion of tungsten (W) from the outer divertor. This topic has already been studied in some detail (see Refs. [151, 152, 153, 154]). Still, it is intimately connected to the N migration, as N ions dominate tungsten sputtering in N-seeded discharges and W sputtering is required to erode tungsten nitride (see section 5.1.4).

Two spectroscopic measurements of emission from $W^{0+}$ are shown in Fig. 5.24. Figure 5.24a presents measurement and simulation for the DOT 1 line of sight, looking into the outer divertor from the top of the main chamber. One can see that there is a notable difference in the absolute value. Here it has to be noted that there exist some uncertainties, like the quality of the PEC employed for W and the width of the experimental line of sight. Nevertheless the qualitative behavior is well reproduced by the simulation: First there is a small increase in the W erosion with the onset of the N puff. When the N radiation induces the transition to the low $T_e$ state the W erosion drops (see section 2.6). When the puff is switched off, the plasma switches back into the high $T_e$ state and the W erosion rises back to its original value.

Figure 5.24b presents $W^{0+}$ emission measurements from a horizontal line of sight (gray and red curves), RON 14, in the outer divertor. This line of sight views a po-
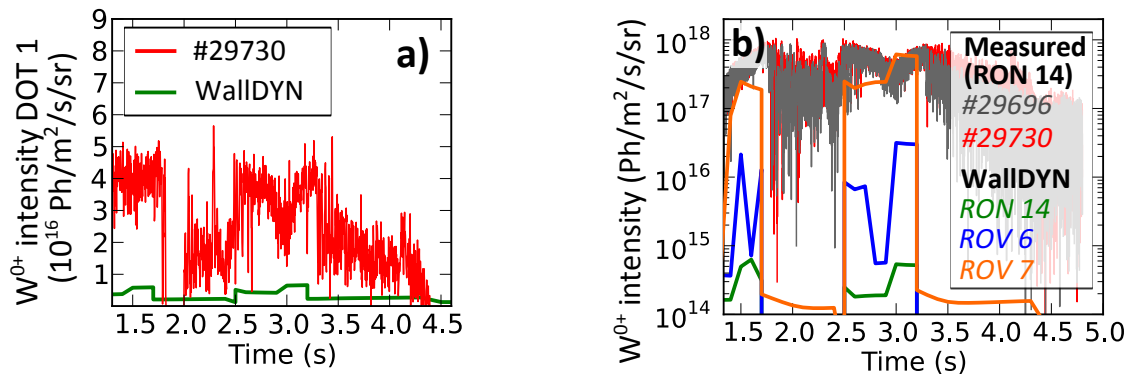
**Figure 5.24:** *Emission from $W^{0+}$ in the outer divertor measured with a vertical (DOT 1) and a horizontal (RON 14) line of sight. These measurements reflect the flux of eroded W atoms. Qualitatively the simulations match the observed behavior. The RON 14 line of sight probably picks up light emitted from atoms adjacent regions with stronger emission.*

sition slightly below the outer strike line as shown in Fig. 5.25b. The corresponding simulation (green curve in Fig. 5.24b) reproduces the measurement qualitatively, but the absolute magnitude is wrong by orders of magnitude. A discrepancy has already been observed for the N emission recorded with this line of sight in Fig. 5.12c. A possible reason is illustrated in Fig. 5.25a: The emission varies within a few centimeters by many orders of magnitude. So a finite width of the experimental line of sight or a small misalignment of the magnetic configuration, which has a typical uncertainty of 1 cm [155, Ch. 4.1.1], can cause such large variations. Actually simulations of nearby lines of sight (blue and orange curve in Fig. 5.24b, the lines of sight are shown in Fig. 5.25b) give a better or even good absolute agreement with the measured erosion during the high $T_e$ phases with strong W erosion. Unfortunately, experimental measurements from these lines of sight are not available.

During the low $T_e$ phases when the tungsten sputtering is small, e.g. around 2 s, the simulated intensity remains below the experimental measurements for all considered lines of sight. Probably this is due to an erroneous measurement, where the W emission is overestimated due to background noise. However, W sputtering for the low $T_e$ state may also be underestimated in the simulations. For example the divertor plasma oscillations (see section 3.2.2), responsible for the scatter in the measurements, could increase the erosion.

The observed W erosion rate is rather small ($\leq 10^{20}$ W/m$^2$) even in the high $T_e$ phases. The net erosion is again about a factor of ten smaller because most of the tungsten is re-deposited close to its origin.
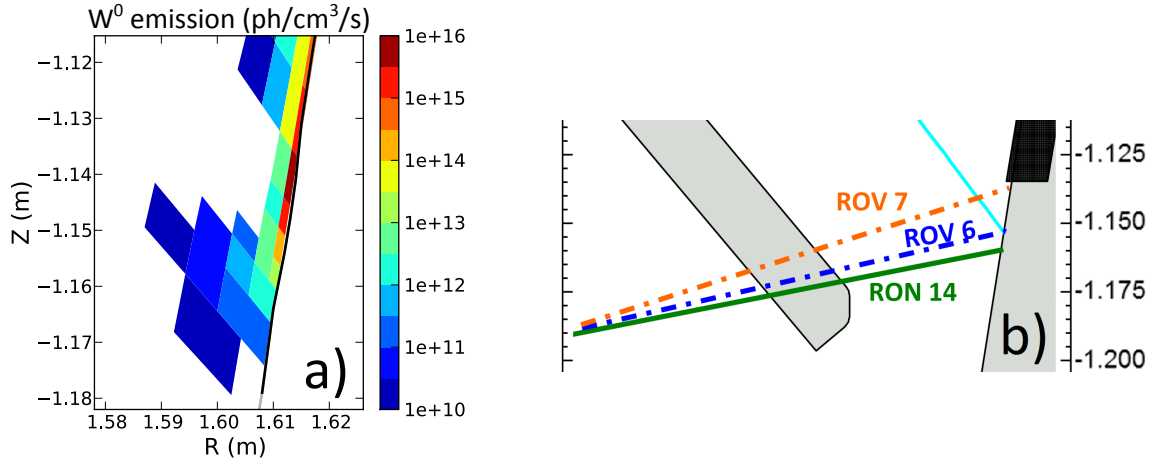
**Figure 5.25:** *The neutral tungsten emission (a) close to the separatrix (cyan curve in (b)) varies by orders of magnitude within one centimeter. Therefore small inaccuracies in the line of sight (b) can lead to very different results.*

## 5.6 Summary of AUG experiments and WallDYN simulations

In this section the nitrogen transport and retention under tokamak divertor plasma conditions was studied experimentally and with WallDYN-DIVIMP simulations. To this end tungsten samples were exposed to the divertor plasma of well-characterized L-mode discharges at ASDEX Upgrade and analyzed with nuclear reaction analysis. Nitrogen distribution and fluxes in the plasma were observed via spectroscopic measurements. The constituents of the residual gas and the number of pumped $N_2$ molecules were determined with mass spectrometry. WallDYN-DIVIMP simulations allow a self-consistent interpretation of these measurements and help to identify the physical processes governing the migration of nitrogen. The main findings are:

- The surface nitrogen content of the outer divertor target saturates within one discharge with (little) N-seeding. The N saturation areal density in the tungsten surfaces of AUG is about $1 \cdot 10^{20}$ N/m². This value is comparable to the saturation areal density observed in laboratory experiments on smooth samples. This indicates that the nitrogen retention does not depend on the surface roughness.

- The surface nitrogen content after nominally identical discharges varies notably. Considering the results from section 4.2, this indicates an intricate dependence of the nitrogen accumulation on parameters like implantation energy and plasma composition. These parameters cannot be fully controlled in a fusion plasma and complicate the interpretation of such experiments.

- WallDYN-DIVIMP simulations, applying the newly implemented saturation

model, can reasonably reproduce the observed nitrogen deposition and spectroscopic measurements.

- The simulations show a strong impact of the nitrogen ionization pattern on the deposition in the outer divertor and contamination of the core plasma. The ionization pattern is very sensitive to the plasma parameters, so a good reproduction of the plasma parameters by the plasma background is essential. The importance of the temperature gradient force and the ion background flows found in previous studies [12] is confirmed, though the present analyses show that especially the flow pattern at the source location (the X-point region in the present study) is of relevance. The transport of ions perpendicular to the magnetic field, either by anomalous diffusion or classical drifts, seems to be of minor importance in the current studies. Probably the closeness of the impurity source location to the considered deposition position emphasizes the neutral transport and leaves no time for the perpendicular transport to become active.

- Residual gas analysis indicates that part of the seeded $N_2$ is converted to ammonia and retained in the AUG vacuum vessel.

- WallDYN simulations of the long term nitrogen retention predict a saturation of the nitrogen content in the plasma facing components at $3$–$5 \cdot 10^{21}$ N atoms. This is in agreement with the results form Ref. [62]. The discrepancy to laboratory experiments reported in Ref. [62] probably originates from an underestimation of the available wall area in AUG.

The presented results have improved the understanding of the nitrogen inventory buildup and migration pathways in AUG. The results also give suggestions for future experimental and theoretical efforts:

- The good agreement between WallDYN-DIVIMP simulations and experimental measurements constitutes a successful benchmark for this novel tool. This promotes the further use of WallDYN and DIVIMP for interpretative and predictive analysis.

- The major source for discrepancies between WallDYN simulations and measurements seems to be the negligence of the depth distributions in the WallDYN surface model. This leads to an overestimation of N sputtering from tungsten nitride in WallDYN. Using a more sophisticated surface model, e.g. including the depth distribution as proposed in Ref. [127] or adapting the sputter model, is therefore a possible option to improve WallDYN. However, one has to keep in mind that WallDYN is mostly used to simulate the long term wall evolution. In such calculations zones of net-erosion and net-deposition develop and the accurate description of mixing effects may be of less importance.

114

- The presented measurements indicate that the nitrogen retention on rough surfaces is not increased. The newly installed version of the AUG divertor manipulator allows to expose several samples at the same poloidal position. This would allow a direct comparison of the nitrogen deposition on rough and smooth surfaces.

- According to WallDYN, the main wall significantly contributes to the nitrogen retention in AUG. The transport of impurities perpendicular to the magnetic field is subject to large uncertainties, so an experimental measurement of nitrogen deposition in the main chamber region would be desirable.

- The residual gas analysis indicates that part of the seeded nitrogen is converted to ammonia and retained in the AUG vacuum vessel. Therefore, further analysis of the formation and distribution of nitrogen containing molecules is required.

# Chapter 6

# Summary and conclusion

The impurity migration in a fusion reactor determines the lifetime of the plasma facing components, the impurity contamination of the core plasma, the tritium retention by co-deposition and induces the formation of mixed materials. An important impurity species is nitrogen, which has been established as an optimal choice to control the divertor heat load in the fusion experiment ASDEX Upgrade [9]. The migration of nitrogen, i.e. implantation in and subsequent release from the tungsten walls, introduces a history effect into the nitrogen particle balance [62]. Therefore, a model of the nitrogen migration is required to optimize the heat load control.

There are two common approaches in the study of plasma-wall interactions. The first one is to study the interaction directly in the devices of interest, in fusion experiments. Such experiments naturally include all relevant physics but may be difficult to interpret. Another widespread approach is to study the underlying processes in computer simulations or dedicated laboratory experiments under well defined conditions. This allows to understand the underlying physics and to extrapolate the results to a fusion plasma environment.

The present work combines both methods to improve the understanding of nitrogen migration in the fusion experiment ASDEX Upgrade: First, the interaction of nitrogen with tungsten surfaces was investigated in laboratory experiments under well-defined exposure conditions. The evolution of the surface was measured with XPS and NRA analysis. Via SDTrimSP simulations the results were interpreted and extrapolated to tokamak divertor conditions. This allowed to establish a thorough theoretical model for accumulation and loss of nitrogen in tungsten. Next, nitrogen retention and transport were studied in dedicated ASDEX Upgrade experiments. To interpret these experiments the WallDYN code was applied, which allows to extrapolate from laboratory studies to experiments in fusion devices. WallDYN simulates the time evolution of the surface composition and impurity fluxes and permits a self-consistent interpretation of various diagnostics.

The laboratory and computational studies presented in section 4.1 confirm that

117

SDTrimSP simulations can correctly describe the implantation of nitrogen into tungsten. In agreement with the known phase of WN, the nitrogen concentration has to be limited in the simulations to $c_N \leq 50\,\%$ to match the experimental measurements. The erosion of tungsten nitride by argon and deuterium is reasonably reproduced by SDTrimSP simulations, although the erosion by deuterium is somewhat overestimated in the simulation. At elevated temperatures the accumulation of nitrogen in tungsten exhibits a complex dependency on material temperature, which is not recovered by the SDTrimSP model: With increasing sample temperature, the nitrogen retention decreases steadily. In contrast, when heating a N-implanted tungsten sample, a diffusive loss of nitrogen is only observed above 800 K. According to these results, the sudden release of nitrogen from tungsten surfaces reaching a critical temperature (suspected in Ref. [10]) is unlikely.

The co-bombardment of tungsten by deuterium and nitrogen was studied in a set of SDTrimSP simulations in section 4.2. These simulations indicate that deuterium strongly modifies the nitrogen depth profile by recoil implantation into the depth and preferential erosion from the surface. The interplay between these two kinetic processes and the limitation of the nitrogen concentration to $c_N \leq 50\ \%$ results in a nitrogen saturation areal density of about $10^{20}$ N/m$^2$.

Chapter 5 presents ASDEX Upgrade experiments on the nitrogen transport in the plasma and its deposition on tungsten surfaces. To study the nitrogen deposition, tungsten coated samples were exposed to ASDEX Upgrade divertor plasmas and analyzed with nuclear reaction analysis. The measured nitrogen content of samples exposed to one and two N seeded discharges is comparable, so that a steady state of the local nitrogen content must have been reached within one discharge. The nitrogen distribution and fluxes in the plasma were measured by passive and active spectroscopy. The retention of nitrogen in the vacuum vessel and production of ammonia were examined via residual gas analysis.

This set of measurements was then compared to WallDYN simulations employing an extended model for the plasma-wall interaction. This model includes the saturation of the nitrogen content in tungsten surfaces and pumping of nitrogen by the vacuum system. The WallDYN simulation employing the SOLPS generated plasma backgrounds reproduces most of the experimental results. A large discrepancy arises only with regard to residual gas analysis. This points to the formation and storage of ammonia in the vacuum vessel of ASDEX Upgrade, a process not included in the WallDYN model. A simulation of the long term nitrogen retention predicts that about $3 \cdot 10^{21}$ nitrogen atoms can be stored in the form of tungsten nitride. This number agrees with the result from Ref. [62]. However, according to the WallDYN simulations the estimate for the plasma wetted area in Ref. [62] was too small. Consequently, the nitrogen saturation areal density given in Ref. [62] is too large.

The good agreement with the experimental measurements is a successful benchmark of WallDYN. For the physical interpretation of the experimental results further WallDYN simulations were set up and analyzed. These simulations employ

adapted transport parameters and customized OSM plasma backgrounds to provide information which is not accessible from experimental measurements. The variations in the outer divertor deposition between the SOLPS based simulation, the 'simple' OSM based simulation and the simulation based on the OSM solution with modified outer divertor plasma temperature, indicate that the nitrogen ionization pattern determines nitrogen fluxes and deposition in the outer divertor. On the other hand, SOL flows do not modify the predicted deposition pattern for the present discharge scenario.

The contamination of the core plasma by puffed impurities is critical for the applicability of impurity seeding to control the peak power load. Hence, the sensitivity of the core nitrogen concentration to input and plasma parameters was studied in dedicated simulations. According to these simulations the dominant source for nitrogen in the core plasma was the applied nitrogen puff. The predicted core contamination essentially varies with all considered parameters: Initial kinetic energy of the atoms (i.e. ionization location), background ion flows (especially the X-point region flow pattern) and temperature gradient force. The discrepancy between simulations based on the SOLPS and 'simple' OSM backgrounds is due to the X-point flow dependence. For a good agreement with the measurements the temperature gradient force must be included, the flows in the X-point region must point towards the divertor and the atoms have to be launched with thermal energies.

The presented results largely resolve the questions on the applicability of nitrogen in fusion devices and reported contradictions between earlier experimental findings. The results on the nitrogen migration are already applied in SOLPS simulations of the power exhaust with nitrogen seeding [136] and WallDYN simulations on the nitrogen migration in ITER are in progress. From a more fundamental point of view, the observed complex temperature dependence and the predicted strong recoil implantation appear as attractive phenomena for further studies. Finally, the good agreement of the WallDYN-DIVIMP simulations to the AUG measurements is encouraging. It gives confidence in the ability to predict processes in a fusion reactor by combining laboratory experiments and computer simulations. This ability is essential to promote understanding and control of the plasma-wall interaction in a future reactor.

# Bibliography

[1] Kreditanstalt für Wiederaufbau (KfW) Entwicklungsbank, *http://www. kfw-entwicklungsbank. de/DE_Home/Sektoren/Energie/Bedeutung_ fuer_Entwicklung_ und_Armutsminderung/Zugang_ zu_Energie. jsp* Stand 19. November 2010.

[2] A. Grundwald, R. Grünwald, D. Oertel and H. Paschen, *Arbeitsbericht Nr. 75 Kernfusion*, Büro für Technikfolgen-Abschätzung beim deutschen Bundestag (2002).

[3] U. Stroth, *Plasmaphysik*, Vieweg+Teubner, Wiesbaden (2011)

[4] European Fusion Development Agreement, *A roadmap to the realisation of fusion energy (2012)*, `http://www.efda.org/2013/01/ fusionsstrom-ins-netz-bringen/`

[5] J. Wesson et al., *Tokamaks*, Oxford University Press, Inc., 3rd edn. (2004).

[6] P.C. Stangeby and G.M. McCracken, Plasma boundary phenomena in tokamaks, *Nucl. Fusion 30, 1225 (1990)*, `http://dx.doi.org/10.1088/ 0029-5515/30/7/005`

[7] G. Federici, C.H. Skinner, J.N. Brooks, et al., Plasma-material interactions in current tokamaks and their implications for next step fusion reactors, *Nucl. Fusion 41, 1967 (2001)*, `http://dx.doi.org/10.1088/0029-5515/41/12/218`

[8] P.C. Stangeby, *The Plasma Boundary of Magnetic Fusion Devices*, Institute of Physics Publishing, Bristol and Philadelphia, 2000.

[9] A. Kallenbach, M. Balden, R. Dux, et al., Plasma surface interactions in impurity seeded plasmas, *J. Nucl. Mater 415, S19 (2011)*, `http://dx.doi.org/ 10.1016/j.jnucmat.2010.11.105`

[10] K. Schmid, A. Manhard, Ch. Linsmeier, et al., Interaction of nitrogen plasmas with tungsten, *Nucl. Fusion 50, 025006 (2010)*, `http://dx.doi.org/10.1088/ 0029-5515/50/2/025006`

[11] O.V. Ogorodnikova, K. Sugiyama, A. Markin, et al., Phys. Scr. T145, 014034 (2011), `http://dx.doi.org/10.1088/0031-8949/2011/T145/014034`

[12] G.F. Matthew, Material migration in divertor tokamaks, *J. Nucl. Mater. 337, 1 (2005)*, `http://dx.doi.org/10.1016/j.jnucmat.2004.10.075`

[13] R.A. Pitts, J.P. Coad, et al., Material erosion and migration in tokamaks, *Plasma Phys. Control. Fusion 47, B303 (2005)*, `http://dx.doi.org/10.1088/0741-3335/47/12B/S22`

[14] A. Hakola, M.I. Airila, et al., Global migration of impurities in tokamaks, *Plasma Phys. Control. Fusion 55, 124029 (2013)*, `http://dx.doi.org/10.1088/0741-3335/55/12/124029`

[15] K. Schmid, M. Reinelt, and K. Krieger, An integrated model of impurity migration and wall composition dynamics for tokamaks, *J. Nucl. Mater. 415, S284 (2011)*, `http://dx.doi.org/10.1016/j.jnucmat.2011.01.105`

[16] G. Meisl, K. Schmid, O. Encke, et al., Implantation and erosion of nitrogen in tungsten, *New J. Phys. 16, 093018 (2014)*, `http://dx.doi.org/10.1088/1367-2630/16/9/093018`

[17] G. Meisl, K. Schmid, M. Oberkofler, Nitrogen retention in ASDEX Upgrade, *J. Nucl. Mater. (2014), in Press*, `http://dx.doi.org/10.1016/j.jnucmat.2014.10.031`

[18] ITER Physics Basis Editors, et al., ITER Physics Basis, *Nucl. Fusion 39, 2137 (1999)*, `http://iopscience.iop.org/0029-5515/39/12`

[19] `http://en.wikipedia.org/wiki/File:Deuterium-tritium_fusion.svg`, version from 28.11.2009.

[20] R. Schneider, Plasma Edge Physics for Tokamaks, *IPP Report 12/1, Max-Planck-Institut für Plasmaphysik, Garching (2001)*, `http://edoc.mpg.de/display.epl?mode=doc&id=378633&col=33&grp=1311#cb`

[21] B. Lehnert, Half a century of fusion research towards ITER , *Phys. Scr. 87, 018201 (2013)*, `http://dx.doi.org/10.1088/0031-8949/87/01/018201`

[22] K. Schmid, et al., submitted to J. Nucl. Mater.

[23] C.S. Pitcher and P.C. Stangeby, Experimental divertor physics, *Plasma Phys. Control. Fusion 39, 779 (1997)*, `http://dx.doi.org/10.1088/0741-3335/39/6/001`

[24] A. Loarte, Effects of divertor geometry on tokamak plasmas, *Plasma Phys. Control. Fusion 43, R183 (2001)*, `http://dx.doi.org/10.1088/0741-3335/43/6/201`

[25] K. Schmid, M. Mayer, C. Adelhelm, et al., Impact of gyro-motion and sheath acceleration on the flux distribution on rough surfaces, *Nucl. Fusion 50, 105004 (2010)*, `http://dx.doi.org/10.1088/0029-5515/50/10/105004`

[26] D. Naujoks, *Plasma-Material Interaction in Controlled Fusion*, Springer Series on atomic, optical, and plasma physics 39, Berlin, Heidelberg 2006

[27] W. Eckstein, *Computer Simulation of Ion-Solid Interactions*, Springer Verlag (1991)

[28] W. Möller, W. Eckstein, and J.P. Biersack, Tridyn-binary collision simulation of atomic collisions and dynamic composition changes in solids, *Comp. Phys. Comm. 51, 355 (1988)*, `http://dx.doi.org/10.1016/0010-4655(88)90148-8`

[29] A. Mutzke, R. Schneider, W. Eckstein, and R. Dohmen, SDTrimSP Version 5.00, *IPP Report 12/08, Max-Planck-Institut für Plasmaphysik (Hrsg.) (2011)*, `http://edoc.mpg.de/display.epl?mode=doc&id=552734&col=33&grp=1311#cb`

[30] R.A. Langley, J. Bohdansky, W. Eckstein, et al., Data Compendium for Plasma-Surface Interactions, *Nucl. Fusion 24, S9 (1984)*, `http://dx.doi.org/10.1088/0029-5515/24/S1/001`

[31] W. Eckstein, Reflection (Backscattering), *IPP Report 17/12, Max-Planck-Institut für Plasmaphysik (Hrsg.) (2009)*, `http://edoc.mpg.de/display.epl?mode=doc&id=434557&col=33&grp=1311#cb`

[32] R. Behrisch (Ed.), Sputtering by Particle Bombardment I, *Topics in Applied Physics, Vol. 47*, Berlin-Heidelberg-New York: Springer-Verlag 1981

[33] J. Bohdansky, *Nucl. Instrum. Methods B 2, 587 (1984)*, `http://dx.doi.org/10.1016/0168-583X(84)90271-4`

[34] C. Garcia-Rosales, W. Eckstein, J. Roth, Revised formulae for sputtering data, *J. Nucl. Mater. 218, 8 (1994)*, `http://dx.doi.org/10.1016/0022-3115(94)00376-9`

[35] W. Eckstein, C. Garcia-Rosales, J. Roth, and W. Ottenberger, Sputtering Data, *IPP Report 9/82, Max-Planck-Institut für Plasmaphysik (Hrsg.) (1993)*, `http://edoc.mpg.de/display.epl?mode=doc&id=394284&col=33&grp=1311#cb`

[36] W.D. Wilson, L.G. Haggmark, and J.P. Biersack, Calculations of nuclear stopping, ranges, and straggling in the low-energy region, *Phys. Rev. B 15, 2458 (1977)*, `http://dx.doi.org/10.1103/PhysRevB.15.2458`

[37] T. Dittmar, M.J. Baldwin, R.P. Doerner, et al., *Phys. Scr. T145, 014009 (2011)*, `http://dx.doi.org/10.1088/0031-8949/2011/T145/014009`

[38] S. Günter, Q. Yu, J. Krüger, K. Lackner, Modelling of heat transport in magnetised plasmas using non-aligned coordinates, *J. Comp. Phys. 209, 354 (2005)*, `http://dx.doi.org/10.1016/j.jcp.2005.03.021`

[39] T. Eich, B. Sieglin, A. Scarabosio, et al., Inter-ELM Power Decay Length for JET and ASDEX Upgrade: Measurement and Comparison with Heuristic Drift-Based Model, *Phys. Rev. Lett. 107, 215001 (2011)*, `http://dx.doi.org/10.1103/PhysRevLett.107.215001`

[40] J. Marki, R.A. Pitts, T. Eich, et al., Sheath heat transmission factors on TCV. *J. Nucl. Mater. 363, 382 (2007)*, `http://dx.doi.org/10.1016/j.jnucmat.2007.01.197`

[41] R. Schneider, X. Bonnin, K. Borrass, et al., Plasma Edge Physics with B2-Eirene, *Contrib. Plasma Phys. 46, 3*, `http://dx.doi.org/10.1002/ctpp.200610001`

[42] L. Aho-Mantila, M. Wischmeier, H.W. Müller, et al., Outer divertor of ASDEX Upgrade in low-density L-mode discharges in forward and reversed magnetic field: I. Comparison between measured plasma conditions and SOLPS5.0 code calculations, *Nucl. Fusion 52, 103006 (2012)*, `http://dx.doi.org/10.1088/0029-5515/52/10/103006`

[43] A. Loarte, B. Lipschultz, A.S. Kukushkin, et al., Progress in ITER Physics Basis Chapter 4: Power and particle control, *Nucl. Fusion 47, S203 (2007)*, `http://dx.doi.org/10.1088/0029-5515/47/6/S04`

[44] S.W. Lisgo, A. Kukushkin, R.A. Pitts, et al., Design assessment of tungsten as an upper panel plasma facing material in ITER, *J. Nucl. Mater. 438, S580 (2013)*, `http://dx.doi.org/10.1016/j.jnucmat.2013.01.121`

[45] A.V. Chankin, D.P. Coster, N. Asakura, et al., A possible role of radial electric field in driving parallel ion flow in scrape-off layer of divertor tokamaks, *Nucl. Fusion 47, 762 (2007)*, `dx.doi.org/10.1088/0029-5515/47/8/006`

[46] ASDEX Upgrade Team, et al., Special Issue on ASDEX Upgrade, *Fusion Sci. Technol. 44, 569 (2003)*, `http://www.ans.org/pubs/journals/fst/v_44:3`

[47] F.J. Casson, R.M. McDermott, C. Angioni, et al., Validation of gyrokinetic modelling of light impurity transport including rotation in ASDEX Upgrade, *Nucl. Fusion 53, 063026 (2013)*, `http://dx.doi.org/10.1088/0029-5515/53/6/063026`

[48] T. Pütterich, R. Dux, R. Neu, Observations on the W-transport in the core plasma of JET and ASDEX Upgrade, *Nucl. Fusion 55, 124036 (2013)*, `http://dx.doi.org/10.1088/0741-3335/55/12/124036`

[49] T. Pütterich, R. Dux, M.A. Janzer, et al., ELM flushing and impurity transport in the H-mode edge barrier in ASDEX Upgrade, , *J. Nucl. Mater. 415, S334 (2011)*, `http://dx.doi.org/10.1016/j.jnucmat.2010.09.052`

[50] H.P. Summers, *ADAS User Manual 2.6*, `http://www.adas.ac.uk./manual.php(2004)`.

[51] R. Balescu, *Transport processes in plasmas Vol. 1*, North-Holland, Amsterdam (1988).

[52] S.I. Braginskii, , Transport processes in a plasma, *Review of Plasma Physics Vol. 1*, M.A. Leontovish (ed.) Consultants Bureau, New York (1965).

[53] D. Reiser, D. Reiter, M.Z. Tokar, Improved kinetic test particle model for impurity transport in tokamaks , *Nucl. Fusion 38, 165 (1998)*, `http://dx.doi.org/10.1088/0029-5515/38/2/302`

[54] P.C. Stangeby and J.D. Elder, Impurity retention by divertors. I. One dimensional models, *Nucl. Fusion 35, 1391, (1995)*, `http://dx.doi.org/10.1088/0029-5515/35/11/I06`

[55] B. Lipschultz, X. Bonnin, G. Counsell, et al., Plasma-surface interaction, scrape-off layer and divertor physics: implications for ITER, *Nucl. Fusion 47, 1189 (2007)*, `http://dx.doi.org/10.1088/0029-5515/47/9/016`

[56] J.D. Elder, A.G. McLean, P.C. Stangeby, OEDGE modeling of the DIII-D H-mode 13CH4 puffing experiment, *J. Nucl. Mater. 363, 140 (2007)*, `http://dx.doi.org/10.1016/j.jnucmat.2007.01.004`

[57] J. Miettunen, M.I. Airila, T. Makkonen, et al., Dissociation of methane and nitrogen molecules and global transport of tracer impurities in an ASDEX Upgrade L-mode plasma , *Plasma Phys. Control. Fusion 56, 095029 (2014)*, `http://dx.doi.org/10.1088/0029-5515/52/3/032001`

[58] D. Told, F. Jenko, T. Görler, et al., Characterizing turbulent transport in ASDEX Upgrade L-mode plasmas via nonlinear gyrokinetic simulations, *Phys. Plasmas 20, 122312 (2013)*, `http://dx.doi.org/10.1063/1.4858899`

[59] L. Aho-Mantila, M. Wischmeier, K. Krieger, et al., Effect of E x B driven transport on the deposition of carbon in the outer divertor of ASDEX Upgrade, *J. Nucl. Mater 415, S231 (2011)*, `http://dx.doi.org/10.1016/j.jnucmat.2010.10.080`

[60] U. Samm, G. Bertschinger, P. Bogen, et al., Radiative edges under control by impurity fluxes, *Plasma Phys. Control. Fusion 35, B167 (1993)*, `http://dx.doi.org/10.1088/0741-3335/35/SB/013`

[61] R. Neu, et al., Overview on plasma operation with a full tungsten wall in ASDEX Upgrade, *J. Nucl. Mater 438, S34 (2013)*, `http://dx.doi.org/10.1016/j.jnucmat.2013.01.006`

[62] A. Kallenbach, R. Dux, J. Fuchs, et al., Divertor power load feedback with nitrogen seeding in ASDEX Upgrade, *Plasma Phys. Control. Fusion 52 055002 (2010)*, `dx.doi.org/10.1088/0741-3335/52/5/055002`

[63] M. Oberkofler, D. Douai, S. Brezinsek, et al., First nitrogen-seeding experiments in JET with the ITER-like Wall, *J. Nucl. Mater 438, S258* (2013), `http://dx.doi.org/10.1016/j.jnucmat.2013.01.041`

[64] G.J. van Rooij, J.W. Coenen, L. Aho-Mantila, et al., Tungsten divertor erosion in all metal devices: Lessons from the ITER like wall of JET, *J. Nucl. Mater. 438, S42 (2013)*, `http://dx.doi.org/10.1016/j.jnucmat.2013.01.007`

[65] P. Petersson, A. Hakola, J. Likonen, et al., Injection of nitrogen-15 tracer into ASDEX-Upgrade: New technique in material migration studies, *J. Nucl. Mater. 438, S616 (2013)*, `http://dx.doi.org/10.1016/j.jnucmat.2013.01.129`

[66] K. Dobes, P. Naderer, N. Lachaud, C. Eisenmenger-Sittner, and F. Aumayr, Phys. Scr. T145, 014017 (2011), `http://dx.doi.org/10.1088/0031-8949/2011/T145/014017`

[67] W. Ensinger, M. Kiuchi, Cubic nitrides of the sixth group of transition metals formed by nitrogen ion irradiation during metal condensation, *Surf. Coat. Technol. 84, 425 (1996)*, `http://dx.doi.org/10.1016/S0257-8972(95)02808-0`

[68] J. Keinonen, J. Risnen, and A. Anttila, Diffusion of nitrogen in ion-implanted chromium and tungsten, *Appl. Phys. A 35, 227 (1984)*, `http://dx.doi.org/10.1007/BF00617172`

[69] S.H. Kim, J.K. Kim, N. Kwak, et al., Atomic Layer Deposition of Low-Resistivity and High-Density Tungsten Nitride Thin Films Using B2H6, WF6, and NH3, *Electrochem. Solid-State Lett. 9, C54 (2006)*, `http://dx.doi.org/10.1149/1.2161451`

[70] G. Soto, W. de la Cruz, F.F. Castillon, et al., Tungsten nitride films grown via pulsed laser deposition studied in situ by electron spectroscopies, *Appl. Surf. Sci. 214, 58 (2003)*, `http://dx.doi.org/10.1016/S0169-4332(03)00343-X`

[71] P.-C. Jiang, Y.-S. Lai, and J. S. Chen, Dependence of crystal structure and work function of W N x films on the nitrogen content, *Appl. Phys. Lett. 89, 122107 (2006)*, `http://dx.doi.org/10.1063/1.2349313`

[72] D. Neuwirth, V. Rohde, T. Schwarz-Selinger, and ASDEX Upgrade Team, Formation of ammonia during nitrogen-seeded discharges at ASDEX Upgrade, *Plasma Phys. Control. Fusion 54 085008 (2012)*, `http://dx.doi.org/10.1088/0741-3335/54/8/085008`

[73] L. Gao, W. Jacob, P. Wang, U. von Toussaint, and A. Manhard, Phys. Scr. T159, 014023 (2014), `http://dx.doi.org/10.1088/0031-8949/2014/T159/014023`

[74] H.T. Lee, M. Ishida, Y. Ohtsuka, and Y. Ueda, The influence of nitrogen on deuterium permeation through tungsten, Phys. Scr. T159, 014021 (2014), `http://dx.doi.org/10.1088/0031-8949/2014/T159/014021`

[75] H. Hertz, Ueber einen Einfluss des ultravioletten Lichtes auf die electrische Entladung, *Ann. Phys. 267, 983 (1887)*, `http://dx.doi.org/10.1002/andp.18872670827`

[76] A. Einstein, Ueber einen die Erzeugung und Verwandlung des Lichtes betreffenden heuristischen Gesichtspunkt, *Ann. Phys. 322, 132 (1905)*, `http://dx.doi.org/10.1002/andp.19053220607`

[77] L.C. Feldman, J.W. Mayer, Fundamentals of surface and thin film analysis, Feldman LC, Mayer JW , editors. New York: Elsevier Scientific Publishing Company, Inc., New York 1986

[78] R. Schlaf, Calibration of Photoemission Spectra and Work Function Determination, `http://rsl.eng.usf.edu/Documents/Tutorials/TutorialsWorkFunction.pdf`, 23.05.2014

[79] `http://de.wikipedia.org/wiki/Photoelektronenspektroskopie#mediaviewer/Datei:XPS_-_Energy_levels_(schematic)_DE.svg`, version from 11.10.2009

[80] S. Hüfner, *Photoelectron Spectroscopy*, Springer, Berlin, Heidelberg (1995)

[81] F. Reinert, and S. Hüfner, Photoemission spectroscopyfrom early days to recent applications, *New J. Phys. 7, 97 (2005)*, `http://dx.doi.org/10.1088/1367-2630/7/1/097`

[82] D. Briggs and J. Grant (Editors), *SURFACE ANALYSIS by Auger and X-Ray Photoelectron Spectroscopy*, IM Publications, Charlton, Chichester (2003)

[83] S. Suga, A. Sekiyama, *Photoelectron Spectroscopy*, Springer Series in Optical Sciences 176, Berlin, Heidelberg (2014)

[84] W.S.M Werner, Electron transport in solids for quantitative surface analysis, *Surf. Interface Anal. 31, 141 (2001)*, `http://dx.doi.org/10.1002/sia.973`

[85] S. Tougaard, and C. Jansson, Comparison of Validity and Consistency of Methods for Quantitative XPS Peak Analysis *Surf. Interface Anal. 20, 1013 (1993)*, `http://dx.doi.org/10.1002/sia.740201302`

[86] S. Tougaard, Low energy inelastic electron scattering properties of noble and transition metals, *Solid State Commun. 61, 547 (1987)*, `http://dx.doi.org/10.1016/0038-1098(87)90166-9`

[87] S. Tougaard, and P. Sigmund, Influence of elastic and inelastic scattering on energy spectra of electrons emitted from solids, *Phys. Rev. B 25, 4452 (1982)*, `http://dx.doi.org/10.1103/PhysRevB.25.4452`

[88] D.A. Shirley, High-Resolution X-Ray Photoemission Spectrum of the Valence Bands of Gold, *Phys. Rev. B 5, 4709 (1972)*, `http://dx.doi.org/10.1103/PhysRevB.5.4709`

[89] J. Vegh, The Shirley background revised, *J. Electron Spectrosc. Relat. Phenom. 151, 159 (2006)*, `http://dx.doi.org/10.1016/j.elspec.2005.12.002`

[90] M.P. Seah, Background subtraction: I. General behaviour of Tougaard-style backgrounds in AES and XPS, *Surf. Sci. 420, 285 (1999)*, `http://dx.doi.org/10.1016/S0039-6028(98)00852-8`

[91] C.D. Wagner, L.E. Davis, M.V. Zeller, et al., Empirical atomic sensitivity factors for quantitative analysis by electron spectroscopy for chemical analysis, *Surf. Interface Anal. 3, 211 (1981)*, `http://dx.doi.org/10.1002/sia.740030506`

[92] S.V. Merzlikin, N.N. Tolkachev, T. Strunskus, et al., Resolving the depth coordinate in photoelectron spectroscopy  Comparison of excitation energy variation vs. angular-resolved XPS for the analysis of a self-assembled monolayer model system, *Surf. Sci. 602, 755 (2008)*, `http://dx.doi.org/10.1016/j.susc.2007.12.005`

[93] C.O. Encke, Wechselwirkung von Stickstoff- & Deuterium-Ionen mit Wolfram, Diploma thesis, Ulm university, 2014

[94] J.C. Vickerman (Ed.), *Surface Analysis*, John Wiley & Sons Ltd, Chichester (1997)

[95] E. Rutherford, Collision of $\alpha$ Particles with Light Atoms. IV. An Anomalous Effect in Nitrogen. *Philosophical Magazine 37, 581 (1919)*. `http://dx.doi.org/10.1080/14786440608635919`

[96] G. Giorginis, P. Misaelides, A. Crametz, and M. Conti, Nucl. Instr. Meth. B133, 396 (1996), `http://dx.doi.org/10.1016/0168-583X(95)01393-8`

[97] L. Gao 2013, private communication

[98] F. Wagner, A quarter-century of H-mode studies, *Plasma Phys. Control. Fusion 49, B1 (2007)*, `http://dx.doi.org/10.1088/0741-3335/49/12B/S01`

[99] H. Zohm, Edge localized modes (ELMs), *Plasma Phys. Control. Fusion 38, 105 (1996)*, `http://dx.doi.org/10.1088/0741-3335/38/2/001`

[100] P.C. Stangeby, J.D. Elder, J.A. Boedo, et al., Interpretive modeling of simple-as-possible-plasma discharges on DIII-D using the OEDGE code, *J. Nucl. Mater. 313, 883 (2003)*, `http://dx.doi.org/10.1016/S0022-3115(02)01470-8`

[101] S. Potzel, Experimental classification of divertor detachment, *IPP Report 10/44, Max-Planck-Institut für Plasmaphysik (Hrsg.) (2012)*, `http://edoc.mpg.de/display.epl?mode=doc&id=628955&col=33&grp=1311#cb`

[102] S. Potzel, M. Wischmeier, et al., A new experimental classification of divertor detachment in ASDEX Upgrade, *Nucl. Fusion 54, 013001 (2014)* , `http://dx.doi.org/10.1088/0029-5515/54/1/013001`

[103] L. Aho-Mantila, X. Bonnin, D.P. Coster, et al., Model-Based Radiation Scalings for the ITER-like Divertors of JET and ASDEX Upgrade, *submitted to J. Nucl. Mater.*

[104] L. Aho-Mantila, D. Coster, M. Wischmeier, In *41st EPS Conference on Plasma Physics*

[105] C. Ruset, E. Grigore, et al., *Phys. Scr. T128, 171 (2007)*, `http://dx.doi.org/10.1088/0031-8949/2007/T128/033`

[106] U. Fantz, Basics of plasma spectroscopy , *Plasma Sources Sci. Technol. 15, S137 (2006)*, `http://dx.doi.org/10.1088/0963-0252/15/4/S01`

[107] K. Behringer, H.P. Summers, B. Denne, et al., Spectroscopic determination of impurity influx from localized surfaces, *Plasma Phys. Control. Fusion 31, 2059 (1989)* , http://dx.doi.org/10.1088/0741-3335/31/14/001

[108] A. Könies, K. Krieger, et al., *Script: IPP Summer University for Plasma Physics* (2004).

[109] E. Viezzer, T. Pütterich, R. Dux and R.M. McDermott, High-resolution charge exchange measurements at ASDEX Upgrade, *Rev. Sci. Instrum. 83, 103501 (2012)*, `http://dx.doi.org/10.1063/1.4755810`

[110] V. Rohde, A. Kallenbach, V. Mertens et al., Wall retention of deuterium and gaseous impurities in all tungsten ASDEX Upgrade, *Plasma Phys. Control. Fusion 51, 124033 (2009)*, `http://dx.doi.org/10.1088/0741-3335/51/12/124033`

[111] D. Neuwirth, Formation of ammonia during nitrogen-seeded discharges at the Tokamak ASDEX Upgrade, *IPP Report 17/33, Max-Planck-Institut für Plasmaphysik (Hrsg.) (2012)*, `http://edoc.mpg.de/display.epl?mode=doc&id=610302&col=33&grp=1311#cb`

[112] V. Rohde, M. Mayer, V. Mertens, R. Neu, K. Sugiyama and the ASDEX Upgrade Team, Dynamic and static deuterium inventory in ASDEX Upgrade with tungsten first wall, *Nucl. Fusion 49, 085031 (2009)*, `http://dx.doi.org/10.1088/0029-5515/49/8/085031`

[113] J.H. Scofield, Hartree-Slater subshell photoionization cross-sections at 1254 and 1487 eV, *J. Electron Spectrosc. 8, 129 (1976)*, `http://dx.doi.org/10.1016/0368-2048(76)80015-1`

[114] W.H. Gries, A Universal Predictive Equation for the Inelastic Mean Free Path-lengths of X-ray Photoelectrons and Auger Electrons, *Surf. Interface Anal. 24, 38 (1996)*, `http://dx.doi.org/10.1002/(SICI)1096-9918(199601)24:1<38::AID-SIA84>3.0.CO;2-H`

[115] M.P. Seah, and I.S. Gilmore, Simplified equations for correction parameters for elastic scattering effects in AES and XPS for Q, b and attenuation lengths, *Surf. Interface Anal. 31, 835 (2001)*, `http://dx.doi.org/10.1002/sia.1113`

[116] J.J. Yeh, and I. Lindau, Atomic subshell photoionization cross sections and asymmetry parameters, *Atomic Data and Nuclear Data Tables 32, 1-155 (1985)*, `http://dx.doi.org/10.1016/0092-640X(85)90016-6`

[117] M.P. Seah, I.S. Gilmore, and S.J. Spencer, Quantitative XPS: I. Analysis of X-ray photoelectron intensities from elemental data in a digital photoelectron database, *J. Electron Spectrosc. Relat. Phenom. 120, 93 (2001)*, `http://dx.doi.org/10.1016/S0368-2048(01)00311-5`

[118] M.P. Seah, and I.S. Gilmore, Quantitative x-ray photoelectron spectroscopy: Quadrupole effects, shake-up, Shirley background, and relative sensitivity factors from a database of true x-ray photoelectron spectra, *Phys. Rev. B 79, 174113 (2006)*, `http://dx.doi.org/10.1103/PhysRevB.73.174113`

[119] L. Schiesko, G. Cartry, C. Hopf, et al., First experiments for Cs doped Mo as surface converter for negative hydrogen ion sources for fusion: determination of the H$^-$ surface generation mechanisms and long term stability, *to be submitted*

[120] K.E. Brenan, S.L. Campbell, L.R. Petzold, *Numerical Solution of Initial-Value Problems in Differential-Algebraic Equations*, Society for Industrial and Applied Mathematics (SIAM), Philadelphia (1996)

[121] Hindmarsh, A. and Taylor, A. "User Documentation for IDA: A Differential-Algebraic Equation Solver for Sequential and Parallel Computers." Lawrence Livermore National Laboratory report, UCRL-MA-136910, December 1999.

[122] P. N. Brown and A. C. Hindmarsh, Reduced Storage Matrix Methods in Stiff ODE Systems, *J. Appl. Math. & Comp. 31, 49 (1989)*.

[123] Wolfram Research, Inc., Mathematica 9 (2013)

[124] V. Rohde, R. Dux, A. Kallenbach, et al., Wall conditioning in ASDEX Upgrade, *J. Nucl. Mater. 363, 1369 (2007)*, `http://dx.doi.org/10.1016/j.jnucmat.2007.01.200`

[125] A. Kallenbach, R. Dux, M. Mayer, et al., Non-boronized compared with boronized operation of ASDEX Upgrade with full-tungsten plasma facing components, *Nucl. Fusion 49, 045007 (2009)*, `http://dx.doi.org/10.1088/0029-5515/49/4/045007`

[126] W. Möller, D. Bouchier, O. Burat, and V. Stambouli, Computer simulation of boron nitride deposition by ion-beam-assisted evaporation, *Surf. Coat. Technol. 45, 73 (1991)*, `http://dx.doi.org/10.1016/0257-8972(91)90208-E`

[127] K. Schmid, Implementation of a diffusion convection surface evolution model in WallDYN, *J. Nucl. Mater. 438, S484 (2013)*, `http://dx.doi.org/10.1016/j.jnucmat.2013.01.099`

[128] M. Mayer, V. Rohde, J. Likonen, et al., Carbon erosion and deposition on the ASDEX Upgrade divertor tiles, *J. Nucl. Mater. 337, 119 (2005)*, `http://dx.doi.org/10.1016/j.jnucmat.2004.10.046`

[129] M. Mayer, V. Rohde, K. Sugiyama, et al., Carbon balance and deuterium inventory from a carbon dominated to a full tungsten ASDEX Upgrade, *J. Nucl. Mater. 390, 538 (2009)*, `http://dx.doi.org/10.1016/j.jnucmat.2009.01.087`

[130] `http://en.wikipedia.org/wiki/Delay_differential_equation`, version from 17.07.2014.

[131] A. Kirschner, V. Philipps, J. Winter, and U. Kögler, Simulation of the plasma-wall interaction in a tokamak with the Monte Carlo code ERO-TEXTOR, *Nucl. Fusion 40, 989 (2000)*, `http://dx.doi.org/10.1088/0029-5515/40/5/311`

[132] P.C. Stangeby, J.D. Elder, Calculation of observable quantities using a divertor impurity interpretive code, DIVIMP, *J. Nucl. Mater 196, 258 (1992)*, `http://dx.doi.org/10.1016/S0022-3115(06)80042-5`

[133] P.C. Stangeby, C. Farrell, S. Hoskins and L. Wood, Monte Carlo modelling of impurity ion transport for a limiter source/sink, *Nucl. Fusion 28, 1945 (1988)*, `http://dx.doi.org/10.1088/0029-5515/28/11/003`

[134] J.D. Elder, P.C. Stangeby, D.G. Whyte, et al., OEDGE modeling of 13C deposition in the inner divertor of DIII-D, *J. Nucl. Mater. 337, 79 (2005)*, `http://dx.doi.org/10.1016/j.jnucmat.2004.10.138`

[135] A. Xuereb, M. Groth, K. Krieger, et al., DIVIMP-B2-EIRENE modelling of 13C migration and deposition in ASDEX Upgrade L-mode plasmas, *J. Nucl. Mater. 396, 228 (2010)*, `http://dx.doi.org/10.1016/j.jnucmat.2009.11.014`

[136] F. Reimold, M. Wischmeier, M. Bernert, et al., Experimental Studies and Modeling of Complete H-Mode Divertor Detachment in ASDEX Upgrade, *Submitted to J. Nucl. Mater.*

[137] P.C. Stangeby, J.D. Elder, W. Fundamenski, A. Loarte, et al., Code-code comparisons of DIVIMP's onion-skin model and the EDGE2D fluid code, *J. Nucl. Mater 241, 358 (1997)*, `http://dx.doi.org/10.1016/S0022-3115(97)80064-5`

[138] J.R. Harrison, *Characterisation of Detached Plasmas on the MAST Tokamak*, Ph.D. Thesis University of York (2010)

[139] D. Elder, 21.01.2014, private communication

[140] D. Reiter, M. Baelmans, P. Börner, The eirene and B2-eirene codes, *Fusion. Sci.Technol. 47, 172 (2005)*, `http://www.ans.org/pubs/journals/fst/a_698`

[141] A.V. Chankin, Classical drifts in the tokamak SOL and divertor: models and experiment, *J. Nucl. Mater 241, 199 (1997)*, `http://dx.doi.org/10.1016/S0022-3115(97)80040-2`

[142] S. Lisgo, *DIVIMP SOL28 User Guide* (2010)

[143] S. Lisgo, P.C. Stangeby, J.D. Elder, et al., Re-construction of detached divertor plasma conditions in DIII-D using spectroscopic and probe data, *J. Nucl. Mater. 337, 256 (2005)*, `http://dx.doi.org/10.1016/j.jnucmat.2004.09.055`

[144] O.B. Bodnar, I.M. Aristova, A.A. Mazilkin, et al., Nitrogen Diffusion Parameters in Ion-Implanted Tungsten Single Crystals, *Physics of the Solid State 48, 10 (2006)*, `http://dx.doi.org/10.1134/S1063783406010033`

[145] S.M. Myers, and R.A. Langley, Study of the diffusion of Au and Ag in Be using ion beams, *J. Appl. Phys. 46, 1034 (1975)*, `http://dx.doi.org/10.1063/1.322207`

[146] K. Schmid, and J. Roth, Concentration dependent diffusion of carbon in tungsten, *J. Nucl. Mater. 302, 96 (2002)*, `http://dx.doi.org/10.1016/S0022-3115(02)00807-3`

[147] N.Q. Lam, Ion Bombardment Effects on the Near-surface Composition During Sputter Profiling, *Surf. Interface Anal. 12, 65 (1988)*, `http://dx.doi.org/10.1002/sia.740120202`

[148] G. Tardini, R. Fischer, F. Jenko, et al., Core transport analysis of nitrogen seeded H-mode discharges in the ASDEX Upgrade, *Plasma Phys. Control. Fusion 55, 015010 (2013)*, `http://dx.doi.org/10.1088/0741-3335/55/1/015010`

[149] R.M. McDermott, C. Angioni, R. Dux, et al., Effect of electron cyclotron resonance heating (ECRH) on toroidal rotation in ASDEX Upgrade H-mode discharges, *Plasma Phys. Control. Fusion 53, 035007 (2011)*, `http://dx.doi.org/10.1088/0741-3335/53/3/035007`

[150] R.M. Churchill, B. Lipschultz, C. Theiler and the Alcator C-Mod Team, Inout impurity density asymmetry in the pedestal region of Alcator C-Mod, *Nucl. Fusion 53, 122002 (2013)*, `http://dx.doi.org/10.1088/0029-5515/53/12/122002`

[151] A. Thoma, K. Asmussen, R. Dux, Spectroscopic measurements of tungsten erosion in the ASDEX Upgrade divertor, *Plasma Phys. Control. Fusion 39, 1487 (1997)*, `http://dx.doi.org/10.1088/0741-3335/39/9/014`

[152] R. Dux, V. Bobkov, A. Herrmann, Plasma-wall interaction and plasma behaviour in the non-boronised all tungsten ASDEX Upgrade, *J. Nucl. Mater. 390, 858 (2009)*, `http://dx.doi.org/10.1016/j.jnucmat.2009.01.225`

[153] M. Mayer, M. Andrzejczuk, R. Dux, et al., Tungsten erosion and redeposition in the all-tungsten divertor of ASDEX Upgrade, *Phys. Scr. T138, 014039 (2009)*, `http://dx.doi.org/10.1088/0031-8949/2009/T138/014039`

[154] R. Neu, A. Kallenbach, M. Sertoli, et al., Tungsten behaviour in radiatively cooled plasma discharges in ASDEX Upgrade, *J. Nucl. Mater. 415, S322 (2011)*, `http://dx.doi.org/10.1016/j.jnucmat.2010.09.036`

[155] F. Reimold, *Complete Detachment in Nitrogen Seeded H-Modes in ASDEX Upgrade*, PhD thesis, Technische Universität München, 2014

# Acknowledgments

# Appendix A

# SDTrimSP input file

&TRI_INP
idrel=0
nh=3000000
nr_pproj=1
idout=-1
flc=20
ncp=3
symbol="N", "W"
case_e0=0
e0=500, 0
case_alpha= 0
alpha0=40, 0
qu=0, 1
qubeam=1, 0
qumax=0.5, 1
inel0=3, 3
ltableread=.true.
irand=31415
e_cutoff=2, 4
e_surfb=0.1, 8.82000
dns0=0.15750, 0.06306
iintegral=2
ipivot=8
isbv=3
dsf =5
iq0=0
ttarget=800
nqx=400

For the D-N cobombardment simulations presented in section 4.2 also two further parameters were set:

qu_int=.true.
case_layer_thick=2

# Appendix B

# Calibration of AUG residual gas analysis

An introduction to the residual gas analysis and vacuum pumping system of AUG is given in section 3.2.5. This section reports some further details, concerning for example the calibration and uncertainties.

The residual gas analysis employs mass spectrometers to analyze the composition of the residual gas. During the actual discharges the spectrometers are operated in the peak jump mode, where only the intensities at a few given masses is recorded. The resulting temporal resolution is somewhat below one second. This temporal resolution is not sufficient to resolve the dynamics of the discharges performed in this work and may cause errors in the determination of the number of pumped atoms. Between two discharges the mass spectrometer is operated in the analog mode, where complete spectra are recorded at the expense of temporal resolution.

The calibration factor relating the measured intensity at m/q=28 to the $N_2$ partial pressure is based on the relative detection efficiencies reported in Ref. [111]. To get the absolute calibration factor for $N_2$, the calibration factor for $D_2$ was determined. The partial pressure of $D_2$ is much larger than the partial pressure from impurity species, so that it is equal to the total pressure. The calibration factor of $D_2$ was determined from a comparison of the intensity measured with the mass spectrometer to capacity gauges installed close to the mass spectrometers. The $D_2$ calibration of HPQI is associated with some error because the capacity gauge installed next to HPQI was only reliable when the intensity at m/q=4 just reached saturation. The calibration factors applied for HPQO were 360 for $D_2$ and 144 for $N_2$ and for HPQI 100 for $D_2$ and 40 for $N_2$. One should note that the mass spectrometers were operated with different settings.

The AUG vacuum vessel is pumped permanently by turbo molecular pumps. During plasma operation a liquid helium cryo pump is switched on and then dominates the pumping speed. The pumping speed of the turbo molecular and cryo pumps

has been measured [112], however only for deuterium. As deuterium is the most abundant species it is usually assumed that all other components of the residual gas are pumped with the same speed. As the discharges presented in this work had rather low pressures, 0.01 Pa in the pumping duct, the pumping speed for nitrogen has a notable uncertainty. An indication for this is that the N concentration is different at HPQI and HPQO. HPQO can only be reached by gas which has passed the cryo pump, so preferential pumping of $N_2$ would cause a reduced $N_2$ concentration for HPQO. cryo pump, so preferential pumping of $N_2$ would cause a reduced $N_2$ concentration for HPQO. Furthermore the pumping speed was only measured in dependence of the pressure at the position of HPQO. The pumping speed at HPQI was then calculated from the conductivity between HPQI and HPQO.

# Appendix C

# SDTrimSP D-N simulation with 60 degree impact
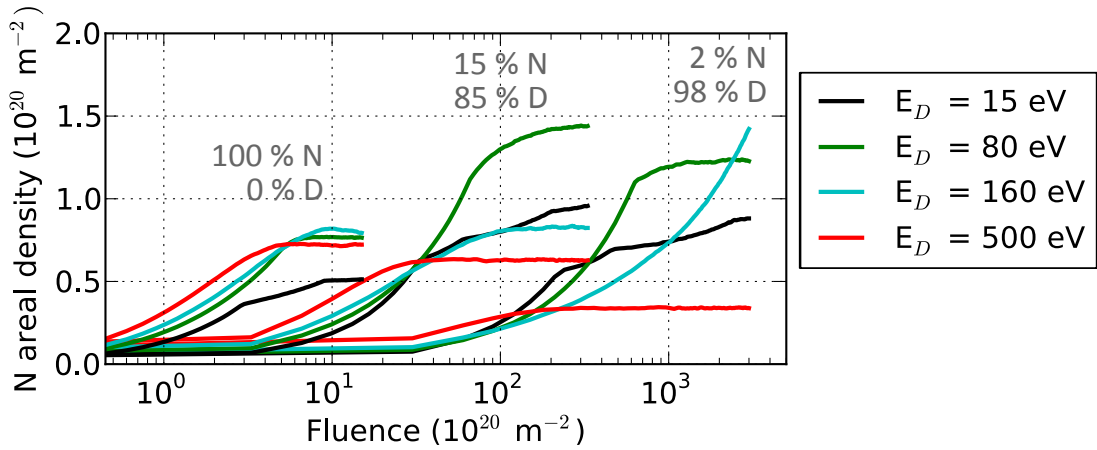


**Figure C.1:** *SDTrimSP simulations of the N accumulation in a W surface under D-N co-bombardment for an impact angle of 60°, different energies and beam compositions. The N energy was twice the D energy, $E_N = 2\,E_D$. The gray numbers indicate the beam composition for the nearby curves. The saturation N areal density varies between $0.5 \cdot 10^{20}$ N/m$^2$ and approximately $1.5 \cdot 10^{20}$ N/m$^2$. On average the N areal density is lower than for 40° implantation, which is shown in Fig. 4.9*

# Appendix D

# Plasma backgrounds

In the plots of the Mach number a positive Mach number (red color) indicates a flow to the outer target and a negative Mach number (blue regions) a flow to the inner target.
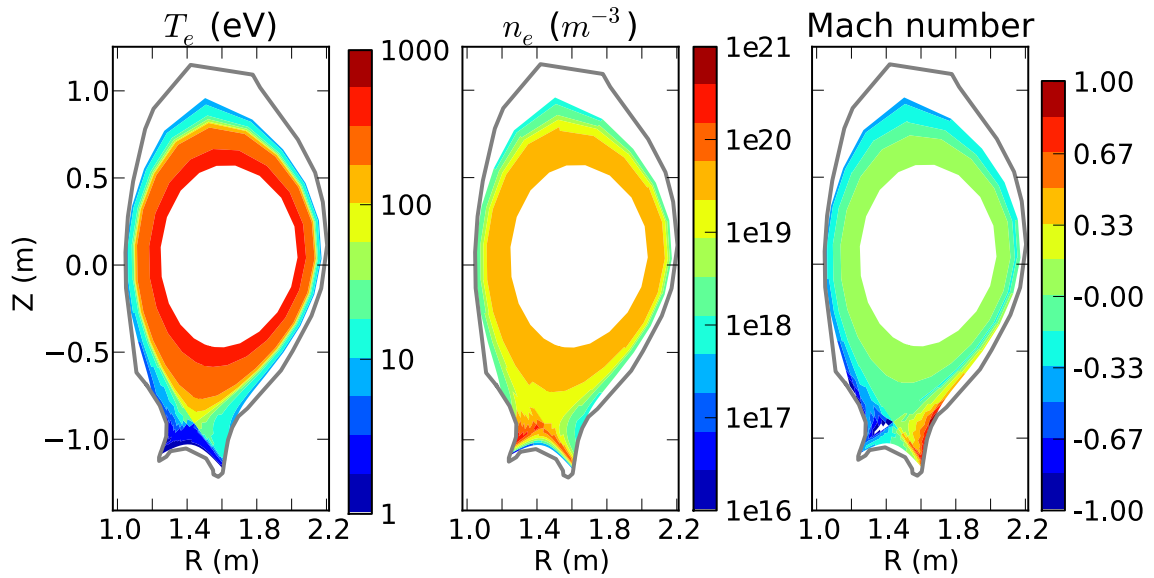


**Figure D.1:** *Electron temperature, density and ion mach number according to the SOLPS simulation corresponding to the N-seeded, low $T_e$ state.*
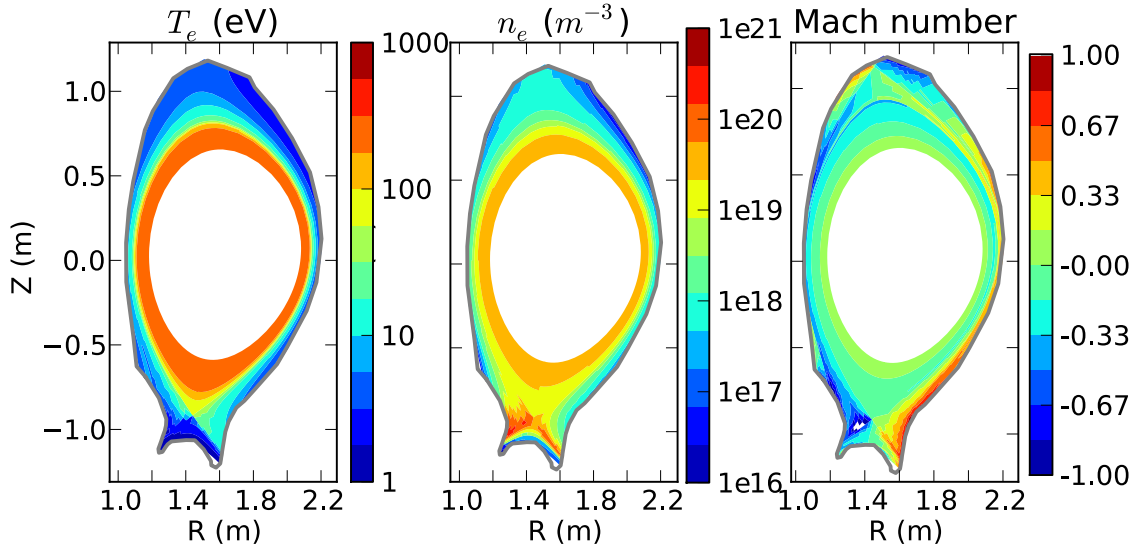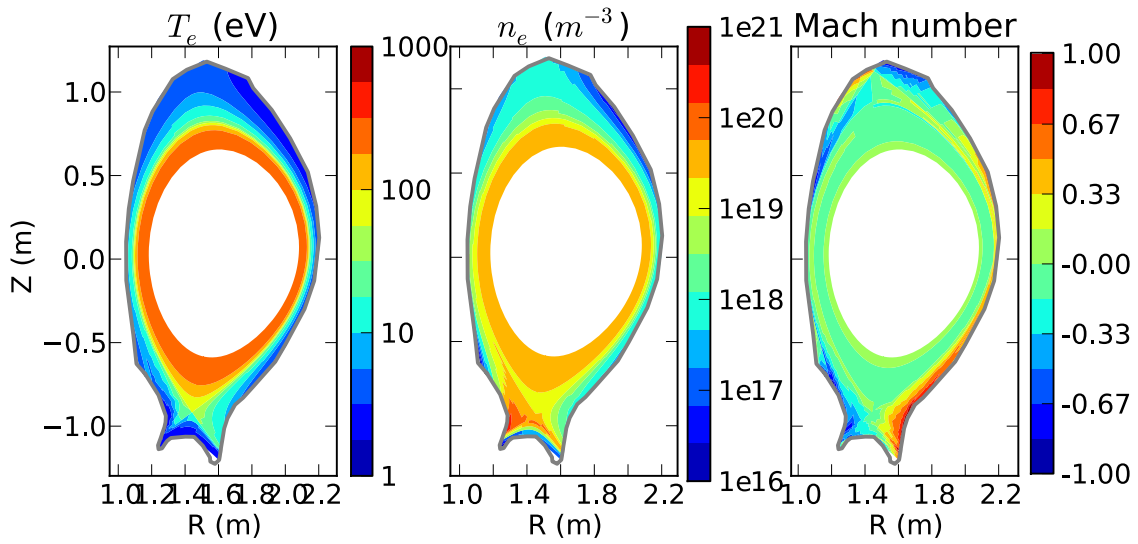
**Figure D.2:** *Electron temperature, density and ion mach number according to the SOLPS simulation corresponding to the N-seeded (low $T_e$ divertor) plasma with an OSM based extension to the main wall.*
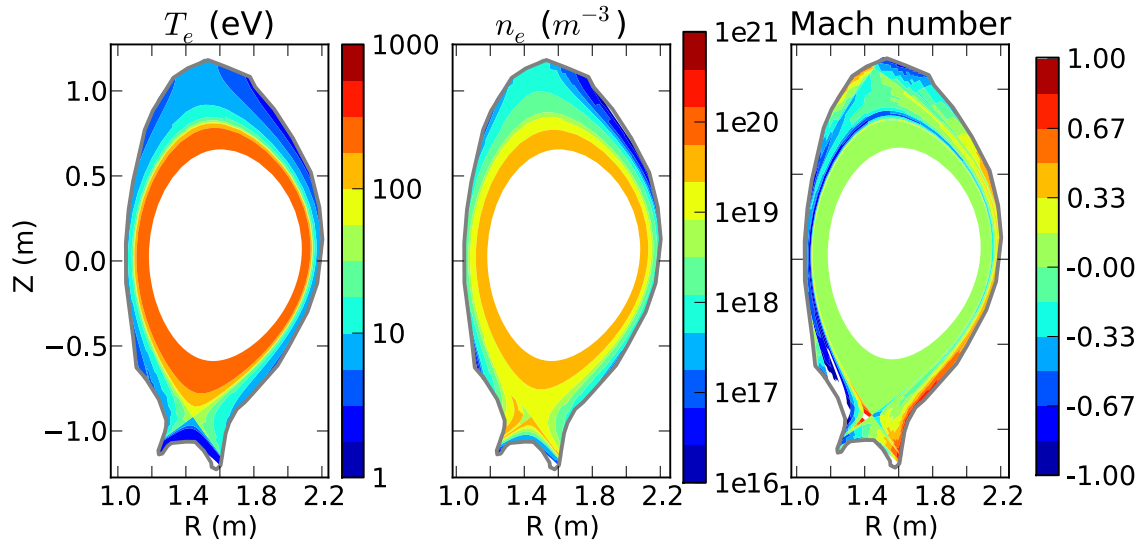


**Figure D.3:** *Electron temperature, density and ion mach number according to the SOLPS simulation corresponding to the non-seeded (high $T_e$ divertor ) plasma with an OSM based extension to the main wall.*

**Figure D.4:** *Electron temperature, density and ion mach number from the simple OSM plasma. To both sides of the X-point there is a upwards directed ion flow. The boundary conditions for this plasma are taken from the simulation shown in Fig. D.1*
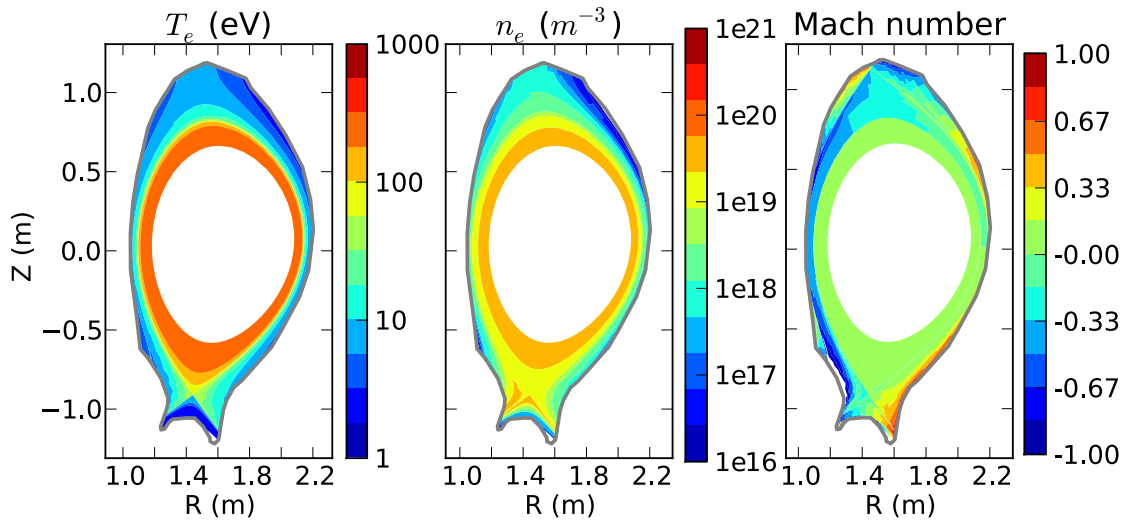


**Figure D.5:** *Electron temperature, density and ion mach number from the OSM plasma with adapted flows.*
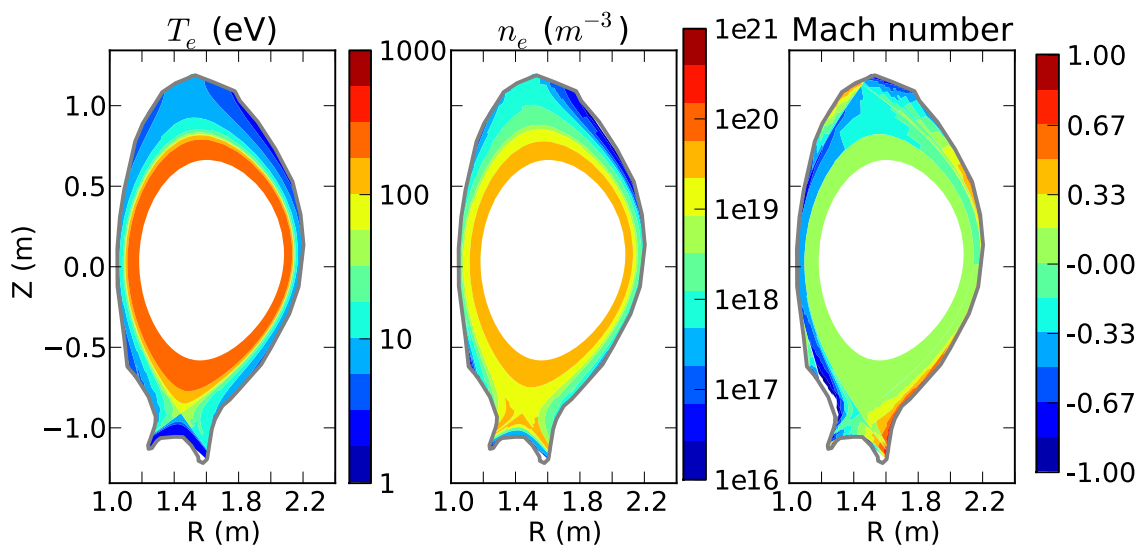
**Figure D.6:** *Electron temperature, density and ion mach number from the OSM plasma with adapted flows and outer divertor plasma.*

# Appendix E

# Nitrogen re-distribution matrix

Fig. E.1 shows the charge state integrated nitrogen redeposition matrix calculated with the low $T_e$ plasma background with extended grid (Fig. D.2). The wall tile indexing is shown in Fig. 3.18. The transport of the impurities through the plasma is parameterized for WallDYN by such re-distribution matrices calculated with DIVIMP. a re-distribution matrix states which percentage of the material eroded from a given tile impinges on another tile. Diagonal contributions indicate local re-deposition. Material from the main wall is deposited in the inner divertor but not in the outer divertor (source tile index 0-25 have no contribution to deposition tiles 30-40). The sum of each line is one, reflecting the particle conservation.
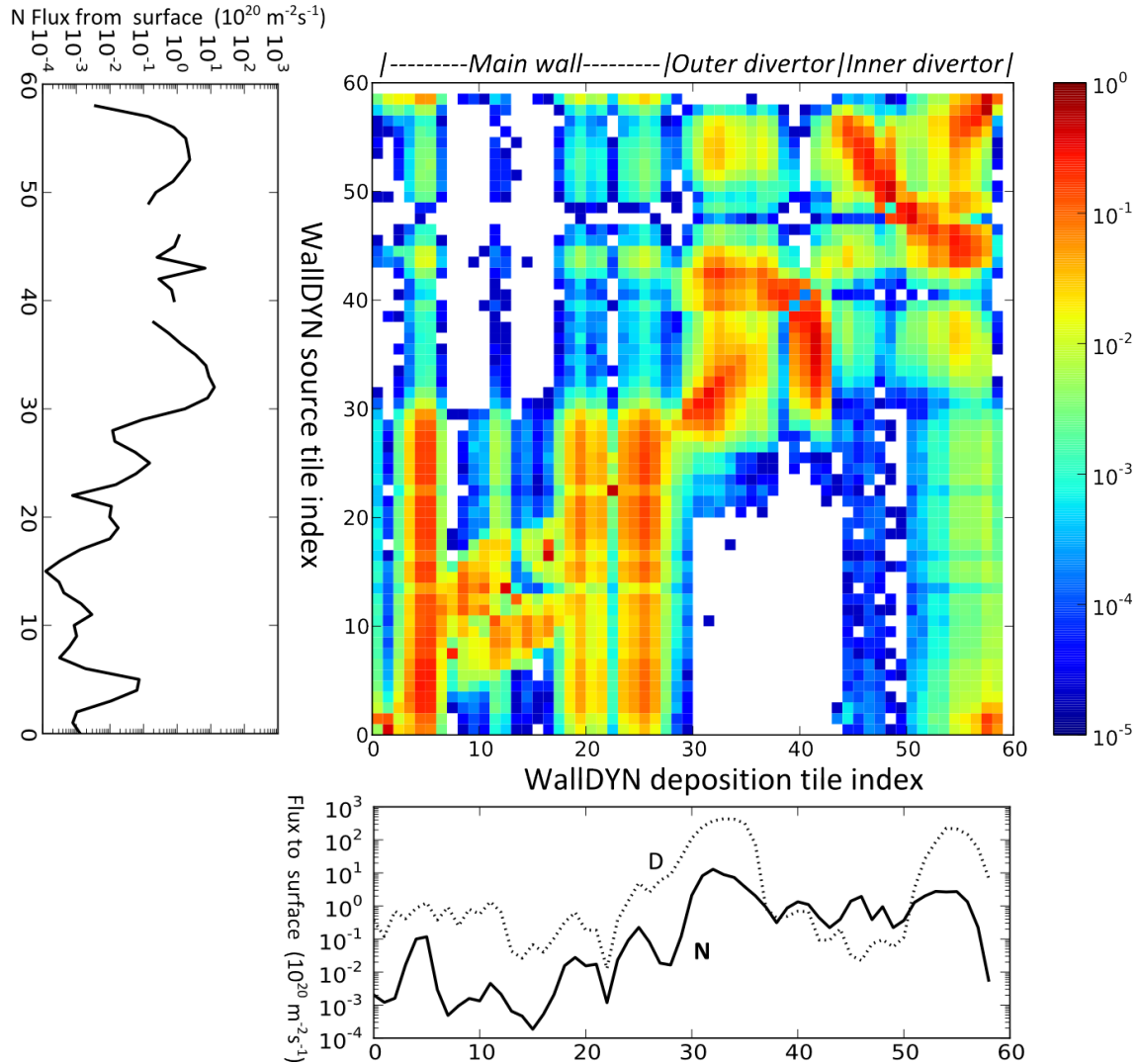
**Figure E.1:** *Charge state integrated nitrogen re-distribution matrix calculated with the low $T_e$ SOLPS plasma background (Fig. D.2). The figures to the left and at the bottom show the N fluxes from the WallDYN simulation at $t = 2.3$ s (corresponding to the end of the first N-seeded phase). The N fluxes are calculated by solving the self-consistent equation for the impurity fluxes, which includes the information from the re-distribution matrix. The figure at the bottom also contains the D flux taken from SOLPS (and the OSM solution in the extended grid region) for reference.*